STUDY OF THE RESPONSE OF THE ATLAS TILE CALORIMETER TO MUONS PRODUCED IN $\sqrt{s} = 7$ TeV PROTON-PROTON COLLISIONS AT THE LHC

by

PIERCE BEN WEATHERLY

Presented to the Faculty of the Graduate School of
The University of Texas at Arlington in Partial Fulfillment
of the Requirements
for the Degree of

MASTER OF SCIENCE IN PHYSICS

THE UNIVERSITY OF TEXAS AT ARLINGTON

August 2011

To my family and friends. Especially my parents,

Michael and Monell, for all their love and support.

ACKNOWLEDGEMENTS

I would like to thank my supervising professor Dr. Kaushik De for allowing me to be a part of this experiment during such an exciting time in High Energy Physics and for his guidance through my undergraduate and master's studies. I wish to thank my academic advisors Dr. Giulio Usai, and Dr. Alex Weiss for their support and for taking time to serve in my dissertation committee. I would like to further thank Dr. Usai for his mentoring and guidance through the course of learning ROOT and understanding the Tile Calorimeter.

I would also like to extend my appreciation to Heather Brown and Carlos Medina-Hernandez for taking care of me while I was without a home during my stay at CERN in the summer of 2010; and to Mark Sosebee and Patrick McGuigan for their help in learning the Tier 3 system and for all their help over the years. I would like to thank those who read this manuscript and helped me correct glaring errors and the simple formatting mistakes: Mark Sosebee, etc

I am grateful to all the great professors here in the physics department and in the math department here at UTA that allowed me to learn so much and taught me that there is so much else that I can and must learn on my own. I would like to especially thank the teachers in my graduate studies for motivating me to higher standards of learning and supporting me through and their personal attentiveness to my graduate studies.

I thank all the wonderful colleagues and fellow students I've had the pleasure of taking classes with here at UTA and working with at CERN. To my fellow students, our problem sessions and helping each other with the details really let the material be that much more interesting and fun to learn.

I appreciate what my family and close friends have done for me. To my parents, Michael and Monell Weatherly for their love and devotion (not to mention their financial support) throughout my life so that I could learn that which I love, and be taught by them the wisdom and love that many in this world are not fortunate to have. I would like to thank my brother Choyce and sister Cymbre for their love and support, and their willingness to discuss science with me. I would also like to thank my uncle Phil Houston for his interesting conversations with my father that got me interested in science at a young age. To my grandparents, both alive and passed, who have believed in me my whole life. To my friends Cory Bourland, Jeremy Pope, and Matt Scarborough for putting up with me through the tough times (finals) and sharing an apartment with me so that I could afford to live closer to the university and get more work done.

I would also like to thank my Lord and Savior Jesus Christ for all the trials and tribulations he has given me and the ability to learn that which I have been allowed too.

July 14, 2011

ABSTRACT

STUDY OF THE RESPONSE OF THE ATLAS TILE CALORIMETER TO MUONS PRODUCED IN $\sqrt{s} = 7$ TeV PROTON-PROTON COLLISIONS AT THE LHC

PIERCE BEN WEATHERLY, MS

The University of Texas at Arlington, 2011

Supervising Professor: Kaushik De

The purpose of this study is to verify the inter-calibration of the cells and uniformity of the Tile Calorimeter (TileCal) detector in the ATLAS experiment at CERN. The response using muons produced in proton-proton collisions at $\sqrt{s} = 7$ TeV is identified. Muons are efficient calibration tools because they are minimum ionizing particles that deposit nearly constant energy in the calorimeter for a wide range of particle energies.

In this study, the tracks of the muons are extrapolated through the calorimeter, and their path lengths through TileCal cells are calculated. The energy, path length, and dE/dx response of the cells are determined. The dE/dx response of each layer and tower is then analyzed for uniformity and compared to Monte Carlo data. Once this has been done, the yield of individual cells is determined by analyzing the number of photo-electrons produced by the muons traversing the scintillating material of the cell.

TABLE OF CONTENTS

LIST OF FIGURES

LIST OF TABLES

CHAPTER 1

INTRODUCTION

1.1 Introduction

Experimental high energy particle physics is at the frontier of science and allows scientists to test the limits of mankind's understanding of the physical world and how it operates at the most fundamental level. This frontier is expanded by accelerating tiny particles up to speeds close to the speed of light in particle accelerators. These highly energetic particles are then collided together in large detectors designed to track and sample the different particles produced in the collisions. In order to be able to make accurate measurements in high energy particle physics, all systems in a detector must be precise, and their response to the particles that will interact with it must be well understood. A complication with a system in the detector not having a well-understood behavior could jeopardize the understanding of rare processes and opportunities for new discoveries that could further our collective understanding of the universe.

1.2 The Large Hadron Collider

The Large Hadron Collider (LHC) is the world's largest particle accelerator, straddling the border between Switzerland and France, just outside of Geneva, Switzerland. It is based at the European Organization for Nuclear Research (CERN), and uses the same tunnel that housed the Large Electron-Positron Collider (LEP), as well as recycling and chaining together the old accelerators on site as storage rings and pre-accelerators. The LHC is a hadron-hadron collider, where hadrons are subatomic

particles consisting of gluons and quarks. The LHC allows for proton-proton (pp) beams to be accelerated up to a center-of-mass energy of $\sqrt{s} = 14$ TeV. At these high energies, physicists will have the opportunity to detect the last piece of the Standard Model (SM), the Higgs particle, a scalar gauge boson thought to give mass to all the particles in the SM. The LHC was also commissioned to test various theories beyond SM like Supersymmetry (SUSY), Extra Dimensions, and Dark Matter (DM) [1].

1.2.1 LHC Specifications

The LHC ring has a circumference of 27 kilometers and is located (on average) 100 meters underground. Currently, the proton-proton collisions in the LHC have a center-of-mass energy of $\sqrt{s} = 7.0$ TeV, with each proton beam having an energy of 3.5 TeV. Eventually, the LHC will reach $\sqrt{s} = 14$TeV, after going through an upgrade currently scheduled for 2013 [2]. The LHC also collides lead ions at $\sqrt{s} = 5.5$ TeV per colliding nuclei for quark-gluon plasma experiments [1]. For a detailed description of the LHC, refer to LHC the guide, source [3].

The first stage in accelerating protons is performed by accelerating them through the Linac2, one of the linear accelerators at CERN, up to 50 MeV and sending them to the Proton Synchrotron Booster (PSB), which brings the protons up to 1.4 GeV. The next step injects the protons into the PS to bring them up to 25 GeV. To accelerate the protons further, they are then fed to the Super Proton Synchrotron (SPS) where they obtain an energy of 450 GeV. The last step to accelerate them up to 3.5 TeV (per beam) is done in the LHC itself, with the two proton beams circulating in opposite directions. For lead ion collisions, the lead ions are accelerated in the Low Energy Ion Ring before being injected into the PS (see Fig. 1.1) [1].

The LHC's beam pipe has a hard vacuum of 10^{-13} atmospheres, so that the protons do not interact with gas molecules. It also contains over 9600 magnets, the ma-

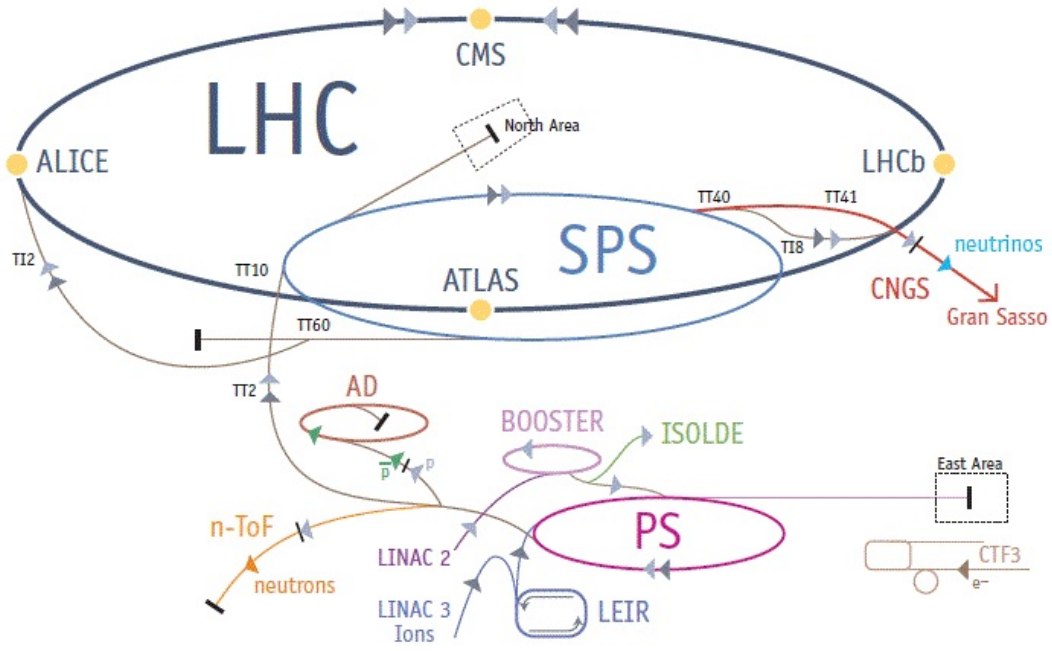

Figure 1.1. Layout of the accelerators and detectors at the LHC.

jority of which are dipole and quadrapole magnets, to accelerate and constrain/focus the beams. Most, if not all of the magnets used in the LHC are superconducting magnets made of superconducting niobium-titanium alloy. To get the superconducting material cold enough, the LHC is cooled down to 1.9 degrees K via superfluid helium, which is colder than the vacuum of space. With these superconducting dipole magnets, the beams can be accelerated to high energies, and steered effectively around the ring. Special Insertion Quadrapole Magnets near the collision points focus the beams so that the likelihood of collisions is higher [3][1].

To find the peak magnetic dipole field needed to accelerate the particles up to 3.5 TeV and steer them, one needs to look at the relationship between the magnetic

field and the forces accelerating the particles. The hadrons are accelerated through the beam pipe by the dipole magnets via the Lorentz force (per particle):

$$\vec{F_L} = q(\vec{E} + \vec{v} \times \vec{B}) = m\vec{a} \tag{1.1}$$

where q is the charge of the particle, $\vec{E}$ is the electric field, v the particle's velocity, $\vec{B}$ is the magnetic field, and m is the mass of the hadron. Since the magnetic field is much stronger than any residual electric field, and since the particles are moving transverse to the magnetic field, the force on the particles is effectively $F_L = qvB$. The acceleration of a particle moving on a circular path is v^2/r, where r is the radius of the LHC ring (r = 4242.9 m). Because the average momentum p of a particle moving in the LHC would be 3.5 TeV/c, we find that the peak magnetic field of the dipole magnets needs to be:

$$B = p/qr \tag{1.2}$$

where B = 2.75 T. The particles are accelerated in sets called bunches. Bunches are collided at the interaction points along the LHC ring and the LHC normally runs with 2808 bunches when the proton beam is at full intensity. Within each bunch, there are nominally 1.15×10^{11} protons at the beginning of each fill; at the collision points, the focusing magnets squeeze the bunch cross-sectional area down to approximately 16 μm.

At $\sqrt{s}$ = 14 TeV the collisions of the bunches will occur at a rate of 40 MHz, or once every 25 ns. At this rate and with 2808 proton bunches, the LHC delivers around 40 million bunch crossings per second at each primary interaction point. With each bunch crossing, around 20 to 25 inelastic pp interactions occur, which gives roughly one billion collisions per second [4].

The rate at which a collider operates, or its performance, is measured in terms of luminosity. The luminosity of a colliding accelerator like the LHC is useful in

determining the rate of event production in particle physics. The rate of production, or the reaction rate R, is linearly proportional to the luminosity L by:

$$R = L\sigma \tag{1.3}$$

where σ is the cross section for a given process [5]. The total luminosity at the LHC can be determined by the proton beam parameters:

$$L = F\xi\frac{fNn_b\gamma}{r_p\beta^*} \tag{1.4}$$

Since the LHC collides beams at small crossing angles, one must factor in this affect into the luminosity calculation by setting $F = 0.9$ and the beam-beam tune-shift parameter $\xi = 0.0034$. The number of protons per bunch is assumed to be equal, while n_b is the number of bunches in the LHC ring and f is the frequency at which the bunches travel around the ring. The proton's classical radius is r_p, γ is the Lorentz factor associated with the proton beam, and β^*= 0.5 m is derived from the amplitude function β for the proton beam at the interaction point [6]. At the design goal of $\sqrt{s}$ = 14 TeV, the LHC will have a maximum luminosity of 10^{34} cm^{-2} s^{-1} [4].

1.2.2 Hadrons

The motivation for accelerating hadrons, specifically protons and lead nuclei, as opposed to leptonic particles like electrons, is that the proton is easily obtainable via ionizing hydrogen gas, and hadrons do not suffer as badly from energy loss due to synchrotron radiation compared to the much lighter electron. This is because synchrotron radiation arise from the acceleration of charged particles. As can be seen in Eq. 1.2, the charge of the particle and the particle's mass remain constant, as well as the radius of the ring. So, to increase the particle's momentum (or velocity), the magnetic field must be increased, up to the limit of the magnetic system. While

bringing the particles up to the desired energy of 7.0 TeV, the particles are constantly undergoing acceleration through the RF cavities. Once the particles have reached the desired energy, the particles are still constantly undergoing a centripetal acceleration, and so energy is lost to syncronotron radiation. Because of this, more energy must be expended to keep the particles at the target energy of 7.0 TeV, and so the great mass difference between protons and electrons is very significant. The amount of energy that must be put into maintaining the desired energy level for the lighter electron is not nearly as economical as it is for the heavier proton [3].

1.2.3 The Different Experiments at the LHC

Because the goals of the LHC are so broad, and since it is the most powerful accelerator on Earth, many scientists from around the world gather there to test their hypotheses at one of the six detector experiments built to take full advantage of the powerful particle beams. There are four collision points arround the LHC ring. At each point, one of four large and medium size experiments surround the beam pipe, hoping to catch a glimpse of something new and exciting. There are also two small scale experiments that are associated with the two largest experiments. The size of an experiment is a reference to both the number of people in the collaboration and the physical size of the detector. The TOTal Elastic and diffractive cross section Measurement experiment (TOTEM) and the Large Hadron Collider forward (LHCf) are the two small LHC experiments. The two medium scale experiments at the LHC are A Large Ion Collider Experiment, or ALICE, and Large Hadron Collider beauty (LHCb). The largest are the Compact Muon Solenoid (CMS) and A Toroidal LHC ApparatuS (ATLAS). The positions on the LHC ring of the four larger experiments (and collision points) can be seen in Fig. 1.1.

ALICE was designed to explore the quark-gluon plasma that is produced by lead ion collisions. This quark-gluon plasma is a state of matter that is believed to have existed shortly after the Big Bang. LHCb is designed to study asymmetries between matter and antimatter produced by B-particle interactions. B-particles are hadrons containig b quarks. Both of these detectors have their own interaction point on the LHC ring and are asymmetric detectors.

CMS and ATLAS, both of which have thousands of collaborators, were designed to be general purpose detectors, thereby enabling searches for the Higgs boson, confirming Standard Model predictions, and looking for evidence of SUSY, DM, and Extra Dimensions. Crucially, they provide a cross-check for one another, such that if one of them finds a signal of new physics, the other can confirm (or not) that they see it, too. The structural and technical design of the two detectors are different. CMS is a densely packed detector wrapped around a large superconducting solenoid, whereas ATLAS is more open with a toroidal magnetic system. Both ATLAS and CMS sit on the primary interaction points of the LHC [3].

CHAPTER 2

ATLAS DETECTOR

The ATLAS detector is shown in Fig. 2.1 [1]. It is a general purpose detector, and is also the largest detector at the LHC. Being a general purpose detector, ATLAS records data from both pp and lead ion collisions with highly precise tracking, momentum and energy (mass) resolution, so that precision searches for the Higgs, SUSY particles, and Dark Matter explorations may be undertaken at the high $\sqrt{s}$ range the LHC provides. In addition to searching for new physics, ATLAS also improves upon SM measurements and parameters, as well as studying the quark-gluon plasma produced in lead ion collisions. In addition to recording events from the proton-proton collisions, ATLAS also records data from cosmic rays that occur naturally in the Earth's atmosphere while the beam is not present. Currently, there are over 3000 physicists involved within ATLAS and over 1000 students, from 174 laboratories and universities in 38 countries. The cavern that houses the ATLAS detector is at Point 1 on the LHC ring, as can be seen in Fig. 1.1. A general guide for the ATLAS experiment as well as many of the images used in this chapter can be found in the ATLAS Fact Sheet [1], and a detailed description of the detector design is given in the ATLAS Technical Design Report [6].

2.1 Overview and Specifications

The ATLAS detector is roughly 46 meters long, 25 meters in diameter, and weighs some seven thousand metric tons. The detector is divided into four large parts: the Long Barrel (or LB), two End Barrels (EB), and the Muon Spectrometer.

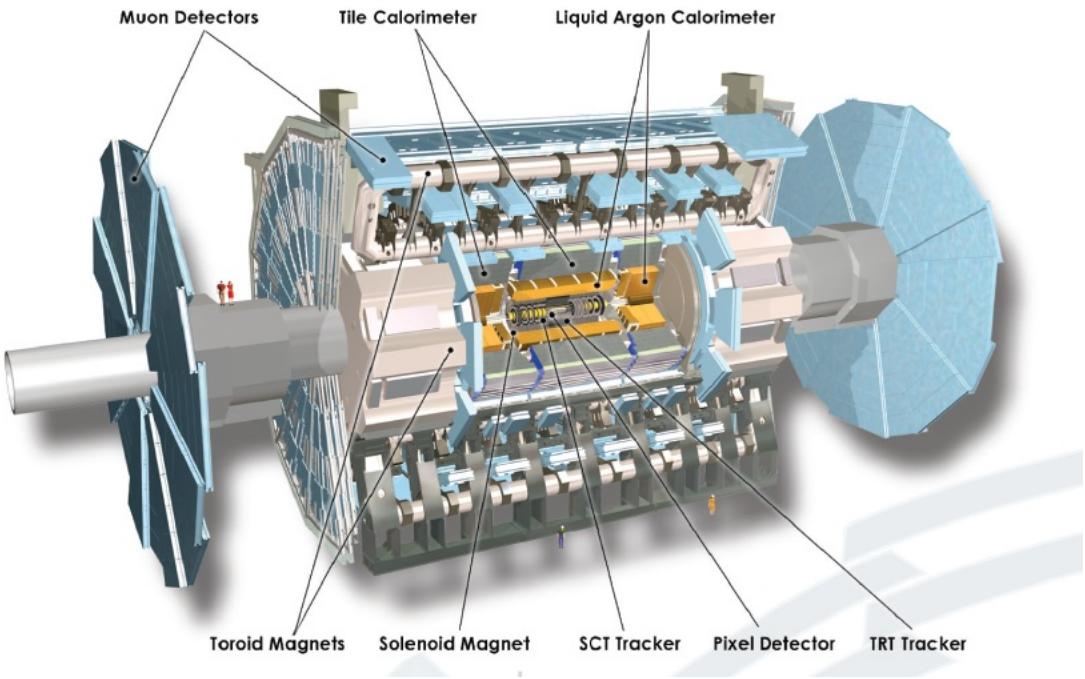

Figure 2.1. Exploded view of the ATLAS Detector.

The Muon Spectrometer consists of the Muon Wheels that cap off the ends of the detector and the Muon Detector that acts as an outer shell for ATLAS. Between the LB and the EB is a gap region which allows for cabling to be fed into the inner detector and thus provide pathways for their electronics and data flow, and also houses cryostats to keep the end caps and long barrel cold. ATLAS is further comprised of many subdetector systems designed to accurately measure the energy and position of the particles passing through the detector [1][6].

2.1.1 Coordinates in ATLAS

ATLAS must employ a coordinate system in which to quantitatively define the location of the particle tracks. Since the beam pipe runs the length of the detector through its center, the z axis is set to coincide with the center of the beam pipe. Because the Interaction Point (IP) of ATLAS is in the middle of the detector, it is

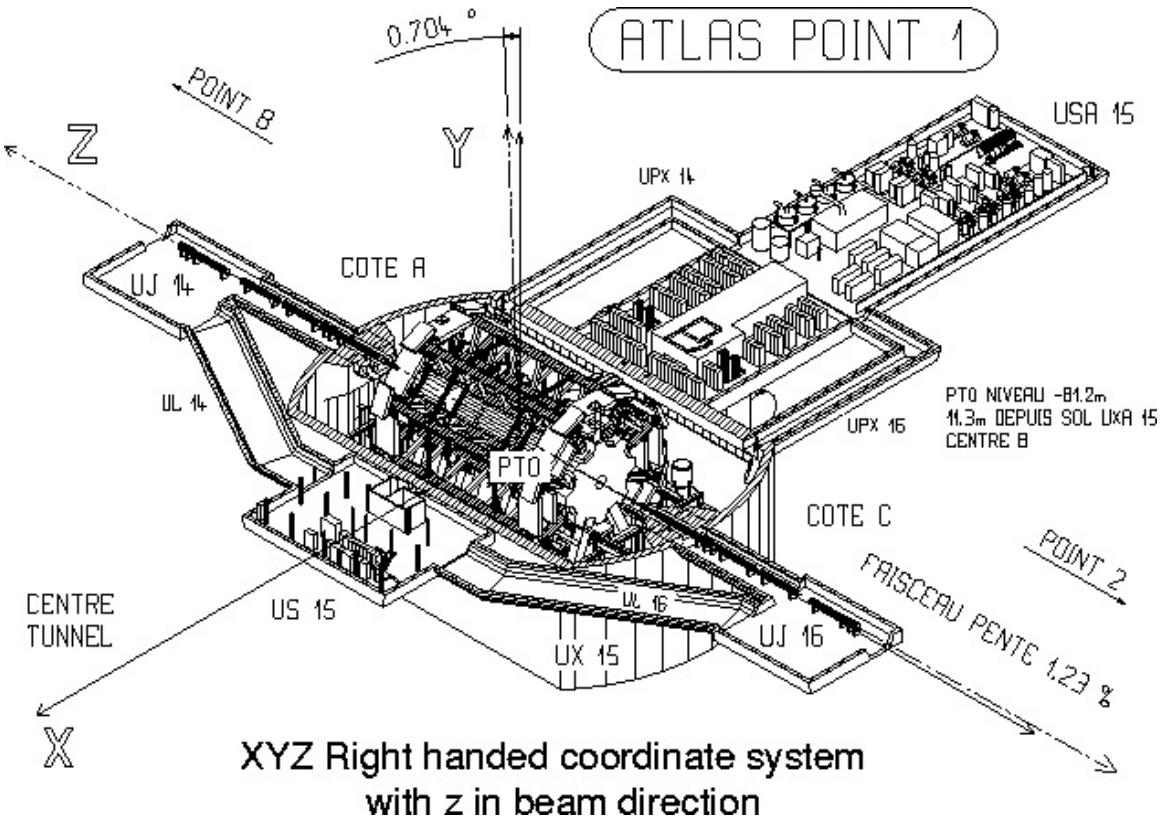

Figure 2.2. ATLAS with Cartesian coordinates.

assigned to be the zero point of the z axis. The positive z axis is termed the "A" side, as this side is nearest to Geneva, and the negative z axis is termed the "C" side, as it is the side nearest to the Jura mountians in France.

For constant values of z, planes normal to the axis are called transverse planes. The $z = 0$ transverse plane is the most important one in the set, and many parameters, such as the transverse momentum p_t are described by this specific plane. Points in this plane can be parameterized in either a Cartesian basis or a cylindrical basis, but since the transformation between the two bases is straightforward, both bases are used. The x axis corresponds to the plane inscribed by the LHC ring, with the positive axis pointing towards the center of the ring. The y axis is normal to the x

and z axes, with the positive axis pointing upward. Figure 2.2 shows the rectangular coordinate system overlaid onto the ATLAS detector [7].

Since ATLAS is cylindrically symmetric, the most economical coordinate system to use is the cylindrical coordinate system. The azimuthal angle is ϕ, and has a range of $(-\pi, \pi]$. The negative portion of the ϕ range is the bottom of the barrel, while the positive ϕ range is the top of the barrel. The ray extending along $\phi = 0$ points towards the center of the LHC ring. The third orthogonal vector is the radial coordinate. Traveling outward from the beam pipe, the interface for each layer of the detector corresponds to a constant value of ρ. As will be seen later, it is also useful to define the detector in terms of a spherical coordinate system (the best way to describe the path information for the particles from the collisions), with θ being the polar angle with respect to the beam pipe, or z axis, and r being the radial vector.

An important quantity that is required to describe a particle is its 4-momentum; the 4-momentum vector must be Lorentz invariant. In rectangular coordinates, the 4-momentum p_ν can be written as:

$$p_\nu = (p_x, p_y, p_z, -E) \tag{2.1}$$

We can reduce the information needed about a particle's momentum to two parameters, the momentum along the beam axis p_z and the transverse momentum p_T. The transverse momentum is defined as:

$$\begin{aligned} \vec{p_t} &= p_x\hat{i} + p_y\hat{j} \\ p_t &= \sqrt{{p_x}^2 + {p_y}^2} \end{aligned} \tag{2.2}$$

Because most of the energy away from the $z = 0$ region is contained within the p_z component, we can normally describe the momentum with $p_z = \beta cos\theta$ and p_t,

where $\beta = E/p$. However, since the polar angle θ is not Lorentz invariant, we define the psudorapidity η in Eq. 2.3 [6] as

$$\eta = -ln\left(tan\frac{\theta}{2}\right) \tag{2.3}$$

With the momentum expressed in terms of $p_z = p_z(\eta)$ and p_T, the 4-momentum is now Lorentz invariant in our desired coordinate system.

2.1.2 Recording and Data

To obtain and process all the information from collisions, ATLAS has over a hundred million electronic channels, along with three thousand kilometers of cabling that connects the detector subsystems to the electronics that filter and sort the data. The data is recorded, after filtering to ignore non-interesting and well understood events, in online processing. Online processing happens at the time the data is recorded using electronic filters, or reconstruction and selection algorithms [4], whereas offline processing occurs once data has already been recorded, and is done on a software level in the ATHENA framework. The offline process reconstructs events and pares the data down to more manageable levels. Since the LHC runs at a very high luminosity, the amount of data available to record is enormous, and would arrive at a rate of roughly 70 TB per second (equivalent to filling 100 thousand CD's every second). To handle all of this information and select the events that are important, a Trigger and Data Acquisition (TDAQ) system was designed for online processing of the collision data. TDAQ sifts through the information and reduces it in three steps called trigger levels.

The Level 1 Trigger must deal with the 40MHz timing of event information flooding into the recording system and pare it down by about a factor of 400. This level of the trigger is purely hardware; it consists of processors designed specifically to

omit non-interesting events without the use of software processing before the information is sent to the Level 2 trigger. This trigger system depends on the identification of physical objects such as muons, jets, photons, leptons, and hadrons identified by the Level 1 trigger in the calorimeters and the muon spectrometer which are known as Region-of-Interests (RoI's). The Level 1 RoI contains the η and ϕ coordinate information, as well as the E_T information and threshold clearance. Events that pass this trigger (about 10^5/sec) are then sent to the Level 2 trigger.

The Level 2 trigger is implemented in software on about 500 dual-core processors. At this trigger level, the feature extraction and hypothesis algorithms process the RoI's from the Level 1 trigger. At this stage, the full granularity of the various regions of the detector are used to group the RoI's together. The data is reduced by a factor of about 30 in the 2nd Level trigger to around 3000 events/second, which is then passed to the Level 3 trigger.

The Level 3 trigger, like the Level 2 Trigger, is executed on computing farms at CERN via software, utilizing about 1700 dual-core processors to mold the information into the raw data format. This raw format is constructed by an event builder that assembles full events from the data fragments taken from ATLAS' readout system. Of the 3000 events passed into the Level 3 trigger every second, only some 200 are kept and converted into raw data for fast offline processing [4].

After the data has passed through the three levels of the Trigger system, the raw data is recorded. This raw data is further reconstructed into physical events due to the collisions like tracks, particles, jets, etc, and is then passed through specialized programs that filter the reconstructed information into physics data (see Table 2.1). This physics data is stored in two formats called ESD's and AOD's. There is little difference between the two, but ESD's retain much more information, whereas AOD's are a more reduced data format.

Table 2.1. Amount of data recorded after passing the Level 3 trigger

Recorded	Per Event (Mb)	Per Year (Tb)
Raw Data	1.6	3200
Reconstructed Data	1.0	2000
Physics Data	0.1	200

These data are distributed amongst a "Tier" system on the GRID network. Tier 0 is located at CERN and houses the raw data and the ESD's and AOD's. The AOD's and ESD's are then replicated to the Tier 1 centers around the world, with each major region having one Tier 1. The Tier 1 for the U.S. is at Brookhaven National Laboratory. At this point in the analysis stage, the data is ready for user analysis. To facilitate these analyses, users often reduce the data down further to formats such as flat Ntuples or D3PD's, which are copied into Tier 2 and Tier 3 systems. Each region in the Tier 1 zones has a Tier 2 from which users within that zone can access data relevant to their analyses via the GRID. However, users can also use the GRID to send their analysis jobs to another Tier 2 if the one in their region does not have the data they wish to use. UTA hosts the Tier 2 for the Southwest region of the United States. The Tier 3 system is designed for users to run local jobs and house large amounts of information for their analyses over short periods of time, as well as use the GRID to send jobs off to the Tier 2 sites.

For an accurate analysis, the collision data must be compared against theoretical predictions. To do this, the ATLAS experiment continuously generates simulated data using Monte Carlo techniques of the events and reconstructions. The simulated data chain begins with a physics event generator (such as PYTHIA), followed by a GEANT detector simulation and finally event reconstruction in the same manner as the real data [8].

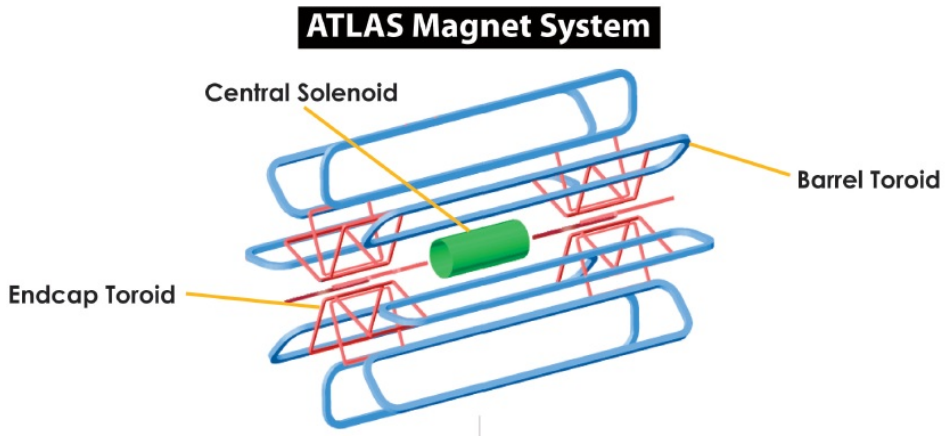

Figure 2.3. The magnetic systems for the ATLAS detector.

2.2 Magnetic systems in ATLAS

There are three magnet systems wrapped around the detector, shown in Fig. 2.3, that bend the paths of charged particles as they propagate through the detector. The bending of a particle's path is important so that its mass and electrical charge can be determined. Each of the parts of the magnetic system are kept cold using liquid helium, so that the magnetic material stays within its superconducting region.

The Central Solenoid magnet has a strength of two Tesla and weighs some five metric tons. It is 5.3 m long and has a radius of 1.2 m with a shell thickness of 4.5 cm. The central solenoid has around 9 km of superconducting wire wrapped around it; the current in the coil is 7730 A. The Barrel Toroid is comprised of 8 isolated coils, each 25.3 meters in length with a diameter of 20.1 m. Together they produce a magnetic field of 4.0 T at a current of 20500 A. The mass of the magnets (including the liquid helium used to cool the coils to 4.7 K) is around 1200 metric tons. The End-cap Toroid magnets are located on the ends of the detector and are five meters in length with an outer diameter of 10.7 m and also consist of eight coils in each

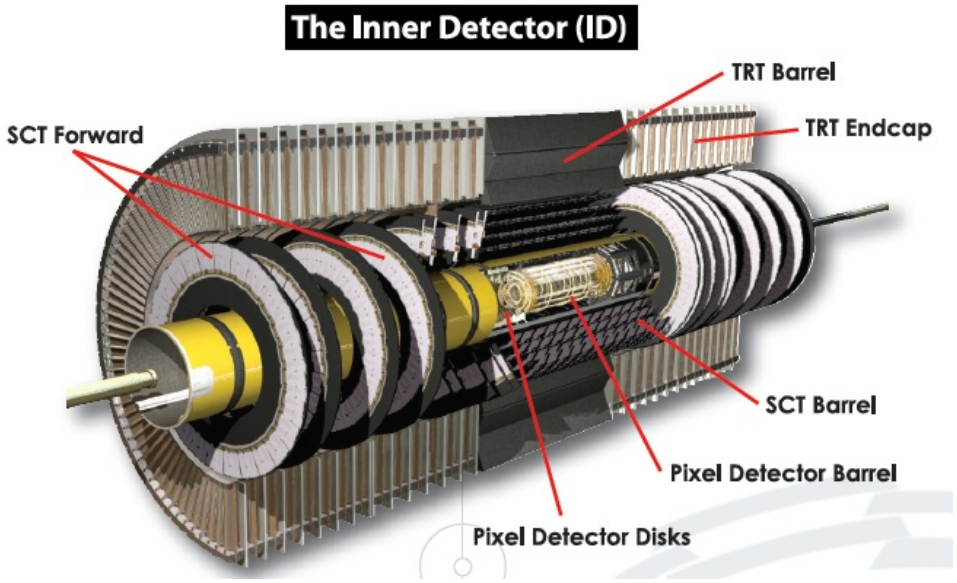

Figure 2.4. The ATLAS Inner Detector.

end. The total mass of each end-cap toroid is 400 metric tons, and they produce a magnetic field of 4.0 T using 20500 A at 4.7 K [1][6].

2.3 The Inner Detector

To accurately determine the identity of the various subatomic particles and determine their energy and trajectory, ATLAS has many sub-detectors. These sub-detectors are designed to deal with specific particle categories, absorbing the particles so that the energy of the particle can be accurately measured, and also ensure specific particle types do not penetrate to the next layer of sub-detectors.

The Inner Detector (ID), Fig. 2.4, is the innermost part of ATLAS detector and surrounds the beam pipe. There are three subsystems that make up the ID: the Pixel Detector, the Semiconductor Tracker (SCT), and the Transition Radiation Tracker (TRT). The three subsystems in the ID are each comprised of a barrel and two end cap disks which cover the range $|\eta| \leq 2.5$.

At the IP, the ATLAS Pixel Detector tracks the particles produced in the collision and helps to trace out their trajectory. The Pixel Detector contains 80 million pixels, with each pixel having an associated electronics channel. The Barrel component has 1744 modules, with each spanning an area of 10 cm^2 and containing 46 thousand pixels. The barrel is split into three layers, out of which the central layer is critical for determining the vertex of a particle (or jet). The end caps of the Pixel Detector house three pixel disks each, and between the three disks, 6.6 million channels are used to read out data.

The second part of the ID is the SCT; it consists of 4088 double-sided modules, and has over 6 million channels which allow the SCT to track charged particles originating from the collisions. The modules themselves are 12 cm long silicon microstrips aligned azimuthally, covering a total are of 60 m^2 between the four barrel layers and 18 end-cap disks. In every silicon module there is a readout strip every 80 μm, which translates to an accuracy in the transverse direction of the strips of 17 μm.

The last part of the ID is the TRT, which together with the SCT, is referred to as the Precision Tracker. The TRT boasts 400 thousand channels and allows a precise measurement of the track of the particles down to 0.17 mm. The TRT is made of straw tubes which contain tungsten wire that has been gold plated and has a radius of 15 μm. The tubes themselves have radii of 2.0 mm, and the overall TRT volume is 16 m^3. There are 100 thousand straws in the barrel, all of which are 150 cm long, and 400 thousand in the end cap disks combined [1][6]. A schematic of the ID layers with inter-layer dimensional specifications can be seen in Fig. 2.5 [9].

2.4 ATLAS Calorimeters

The ATLAS detector has two calorimeters, The Liquid Argon Calorimeter (LAr) and the Tile Calorimeter (TileCal), whose layout can be seen in Fig. 2.6 [9]. This

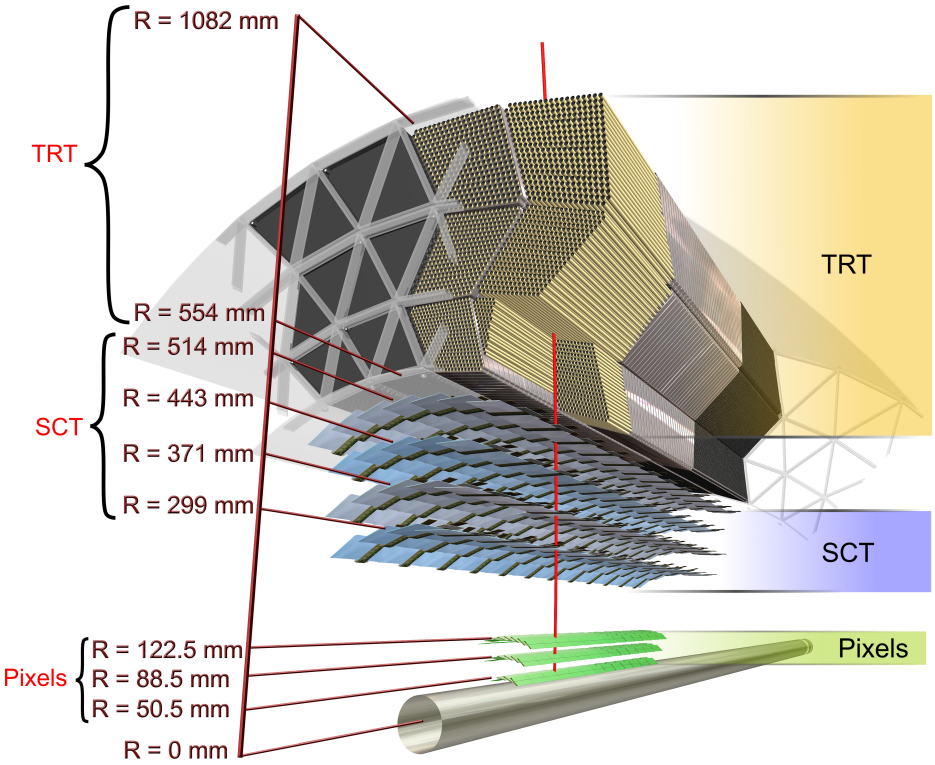

Figure 2.5. Cross-section of the ATLAS Inner Detector.

multipart calorimeter design allows ATLAS to have good jet and missing transverse energy ($E_T{}^{miss}$) tracking and reconstruction, both of critical importance for Higgs and SUSY analyses as well as other BSM studies. The Liquid Argon Calorimeter is the electromagnetic (EM) calorimeter for the ATLAS detector and, as such, it is used to track the position of photons, electrons, and positrons, in addition to accurately measuring their energy. In most cases, the LAr fully absorbs the photons and light leptons, but occasionally very high energy photons punch through to the TileCal. The TileCal is the hadronic calorimeter for ATLAS, which absorbs and measures

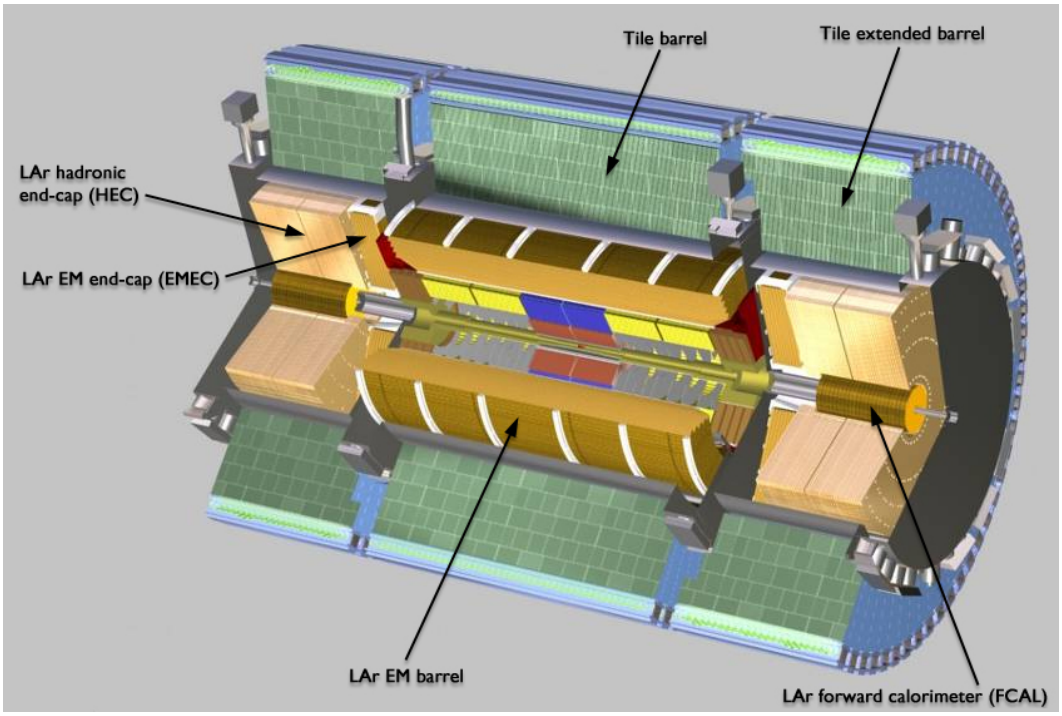

Figure 2.6. The ATLAS calorimeter.

the energy and position of hadrons and their associated showers of particles and jets produced by hadronic decays. Since the hadrons decay in the TileCal, the volume of the calorimeter needs to be large enough to encompass their daughter particles in order to accurately measure the energy of the parent hadrons [6].

2.4.1 The Liquid Argon Calorimeter

The LAr detector (see Fig. 2.7 [9]) is comprised of lead absorber plates and cold liquid argon cooled to 90 K. The high granularity needed for precise position measurements is achieved by using accordion shaped layers (Kapton electrodes and Pb plates), but due to the odd shape, calibration is used to correct for this in the transition to η and ϕ coordinates. It surrounds the ID, and has a barrel section and two end-cap sections with approximately 190 thousand channels combined. The

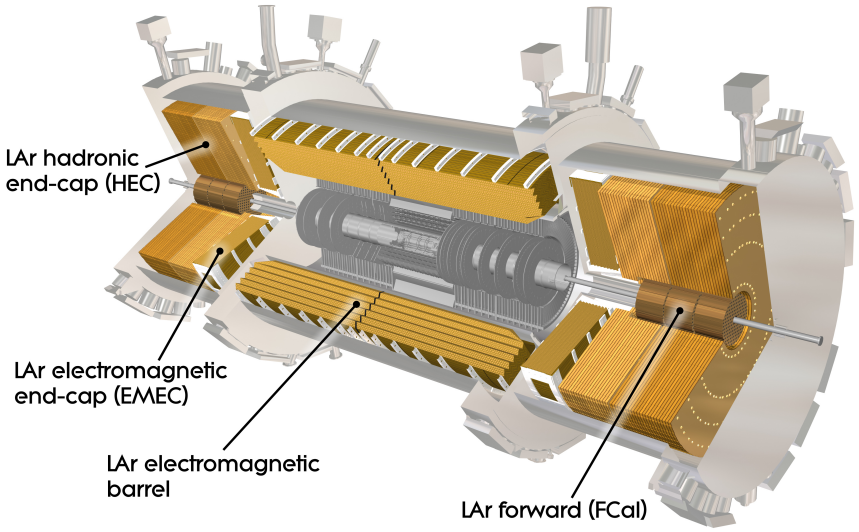

Figure 2.7. The ATLAS liquid argon calorimeter.

barrel of the LAr calorimeter is 6.4 m long and is a little over half a meter thick. The barrel covers a psudorapidity range of $|\eta| \leq 1.475$, but contains a 6.0 mm gap at $z = 0$. The end-caps are 63.2 cm thick and are 4.15 m in diameter, and are mechanically separated into two wheels. The outer wheel covers the psudorapidity range $1.375 < |\eta| < 2.5$. The LAr's inner end-cap wheel is called the Forward Calorimeter (FCal), and is a hadronic calorimeter. It extends the psudorapidity range of ATLAS' hadronic calorimetry up to $|\eta| < 3.2$. The EM calorimeter is large enough such that its thickness is greater than 24 and 26 radiation lengths in the barrel and end-caps, respectively.

Both the barrel and the outer end-cap wheel have three longitudinal sections that act as pre-shower detectors, allowing for the enhancement of particle identification and precise psudorapidity measurements. To achieve this high granularity, the middle barrel layer (located at shower-max) is segmented into regions of size $\Delta\phi \times \Delta\eta = 0.025 \times 0.025$ [1][6].

2.4.2 The Tile Calorimeter

The TileCal is the primary hadronic calorimeter of ATLAS and surrounds the LAr system. It is divided into three parts, two end-caps and a long barrel section. The TileCal is mechanically subdivided into 64 wedges in ϕ. Each wedge, or module, is 560 cm long (260 cm in the end caps), and the barrel weighs 20 metric tons. The whole of the TileCal is comprised of 500 thousand tiles of varying sizes and grouped into units called cells. The cells are made of plastic scintillator material used to sample the hadrons and jets and steel plates used as absorber material [1].

Since the response and inter-calibration of the TileCal due to muons from collisions and cosmics is the central focus of this thesis, the Tile Calorimeter will be discussed in greater detail in the next chapter.

2.5 The Muon Spectrometer

To be able to more accurately determine the energies in the events coming from collisions, and to reduce the background due to cosmic radiation, the Muon Spectrometer is designed to determine muon momentum and masses with high resolution. This muon system, as seen in Fig. 2.8 [9], is comprised of several different sections, a barrel, two end-caps, and two Muon Wheels (the Monitored Drift Tube chambers located furthest away from the IP, after the gap past the end-caps). The spectrometer has a total surface area of around 5000 m^2, and covers the whole of ATLAS in ϕ and a range of $|\eta| < 3$ with good hermiticity for muon track reconstruction. Most of the spectrometer is attached to the torridal magnet girder structure for support, or on girders designed specifically for supporting the muon chambers and connected to service structures or ATLAS's main rails. The service racks and readout electronics are accessible on the outer hull of the spectrometer. A complete description of the

Muon Spectrometer and images used in this section can be found in the ATLAS Muon Spectrometer Techical Design Report [10].

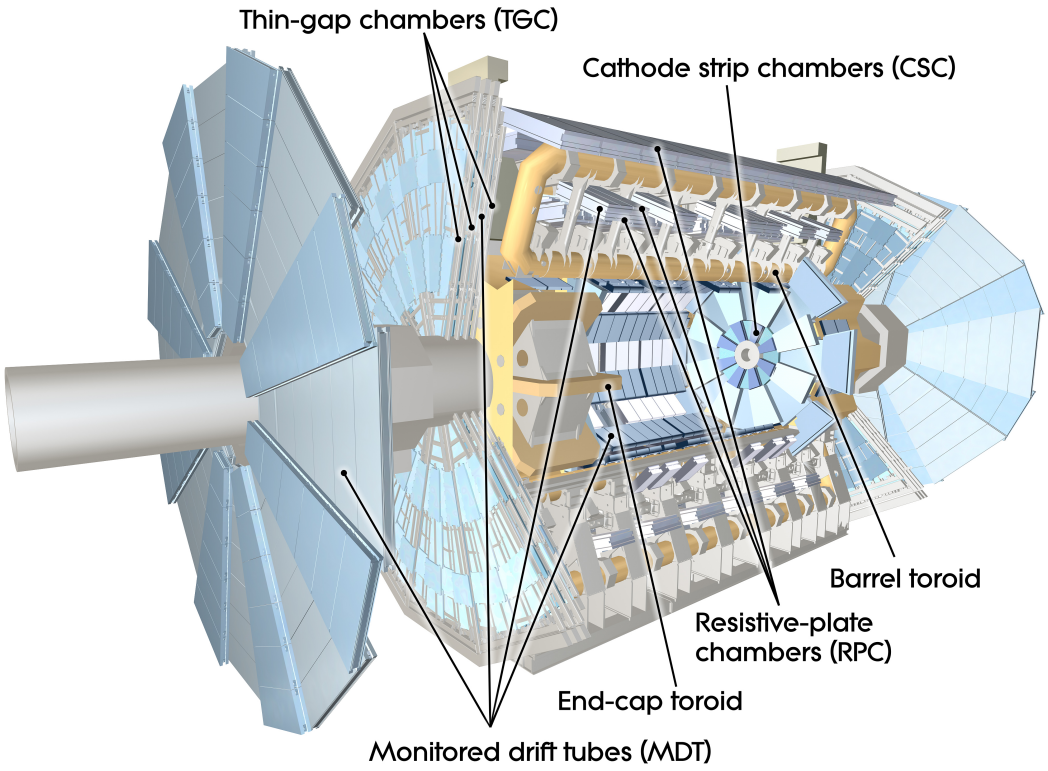

Figure 2.8. The ATLAS Combined Muon System.

The detector is configured to optimize the momentum resolution by ensuring that each particle will cross at least three layers, known as stations, in the chambers. The barrel section has three layers coaxial with the beam pipe located at 5.0, 7.5, and 10 m away from the beam axis, while covering the range $|\eta| < 1.0$. The end caps also consist of three layers of chambers located 7, 10, and 14 meters from the IP, while the Muon Wheels are located 21 to 23 meters away from the IP. Both the end caps and the Muon Wheels lie parallel to the transverse plane, and cover the range $1.0 < |\eta| < 2.7$. However, to ensure that the cabling and services can reach the inner systems,

the central solenoid, and the Tile and LAr calorimeters, an opening was left at $\eta = 0$.

For trigger selections, the muon system was designed to be sensitive for a range of transverse momenta from 5.0 to 20 GeV/c, while for trigger coverage, the muon system delivers high efficiency in the region $|\eta| < 2.4$ needed for CP violation, Higgs, and B physics studies. Since this analysis uses muons from pp collision processes, the Muon Spectrometer plays an integral part in sifting through the background events to look specifically for muons to study their effects on the TileCal.

The Muon Spectrometer has an accuracy in muon track measurements of better than 50 μm by taking measurements of the track in r and z, the direction that is parallel to the direction that the magnetic fields bend the muons. The z coordinate is measured by the barrel, while the r coordinate is measured by the end caps and in the transition region. To achieve these measurements, the Muon Spectrometer has Monitored Drift Tube (MDT) chambers along the barrel, end-caps, and Muon Wheel that provide a resolution of approximately 30 μm, while Cathode Strip Chambers (CSC's) are used to provide measurements in the region $2.0 < |\eta| < 2.7$ in the first layer of the end caps. Resistive Plate Chambers (RPC's) provide trigger functionality for the barrel, while Thin Gap Chambers (TGC's) provide it for the end caps [10].

2.5.1 Monitored Drift Tubes

The MDT chambers are made of tubes containing gas and a central wire. The tubes have a radius of 15 mm, with 0.4 mm thick aluminum walls, while the non-flammable gas mixture of Ar-CH_4-N_2 in the tubes is under a pressure of three bars and has a volume of 800 m^3. The tungsten-rhenium alloy central wire has a radius of 15 μm and is kept under an electric potential of 3270 V. The resolution of the individual tubes is 80 μm, with a maximum drift time of 480 ns. To give the chambers a

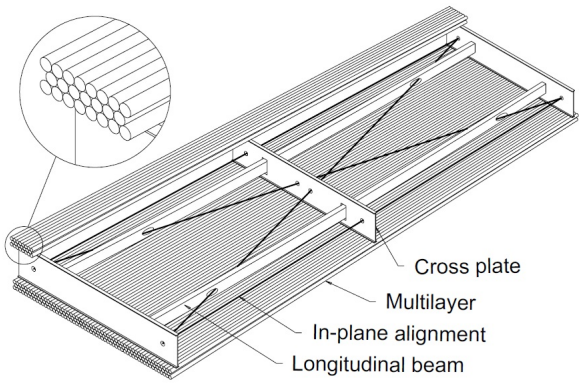

Figure 2.9. Schematic for the Monitored Drift Tube Chamber.

higher resolution with good pattern recognition, the chambers are constructed from mono-layers of the drift tubes, which are then stacked three or four high into multi-layers on either side of the support structure, or spacer frames, shown in Fig. 2.9. The spacer frames allow for the drift tubes to be positioned accurately, while also housing alignment system components, in plane optical devices that monitor the drift tubes. Each of the drift tubes is read out by a preamplifier at one end followed by a differential and shaping amplifier, and a discriminator. The time offsets between different channels are corrected by a phase calibration system. Information is fed into circuit boards mounted on the outside of the chambers, which feed the data to readout drivers in the experimental area [10].

2.5.2 Cathode Strip Chambers

Each multi-wire chamber of the CSC houses segmented cathode strips used to read out the information from the anode wires through ribbon cable jumpers out to the outer panels where electronic read out boards are located. The charge induced on the cathode strips by the anode cascade is used to determine the coordinates, with the transverse coordinate given by strips parallel to the anode wires, and the precision

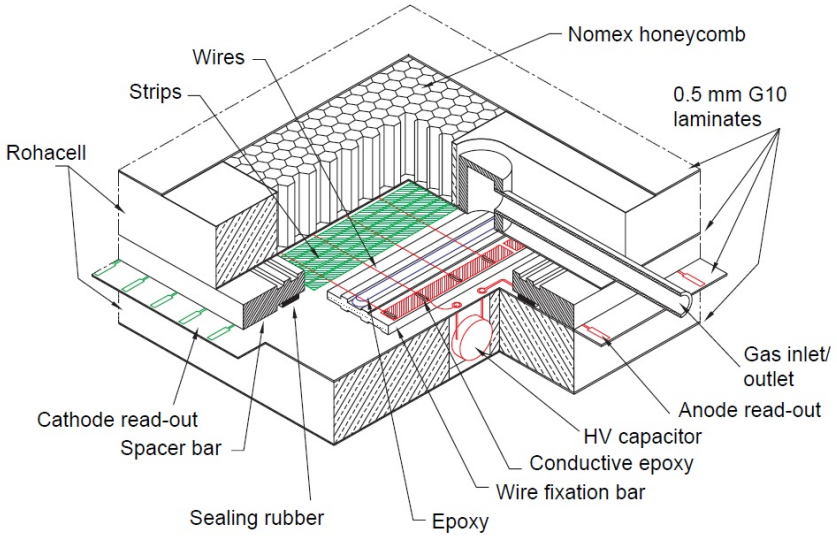

Figure 2.10. Schematic for a Cathode Strip Chamber Layer.

measurement by strips orthogonal to the anode wires. With the segmentation of the cathode strips and by interpolating the charge from neighboring strips, the CSC yield a high spatial resolution (better than 60 μm), and good two-track resolution. The CSCs have a time resolution of 7.0 ns and electron drift times less than 30 ns, while also having low neutron sensitivity due to the baseline gas (Ar-CO_2-CF_4) not containing any hydrogen. The wires of the CSC are made of the same alloy as the wires in the MDT's, but are thinner, having a diameter of 30 μm and are put under a 2600 V electric potential. Each layer of the CSC, as seen in Fig. 2.10, is housed in rohacell panel frames, and each multilayer of four layers is composed of five Nomex honeycombed panels and two thin cathodes formed from copper clad FR4 laminates. The electronic readout boards have sixteen channel CMOS IC chips consisting of pulse shaping amplifiers, driven by a charge-sensitive preamplifier [10].

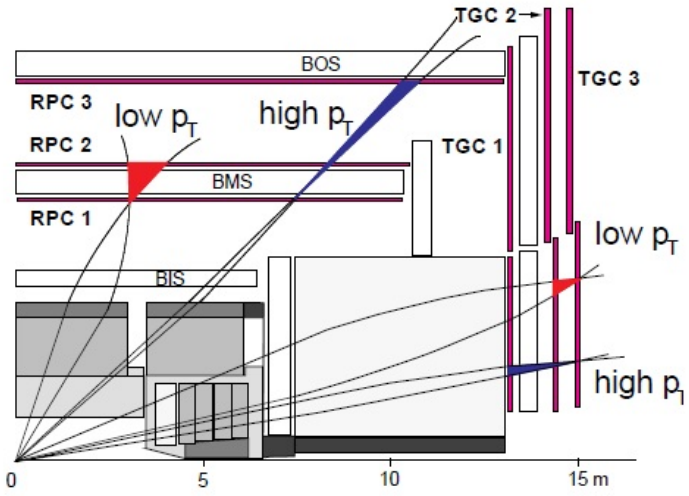

Figure 2.11. Level 1 trigger scheme for the Muon Spectrometer.

2.5.3 Muon Spectrometer Trigger System

To determine if events passing through the spectrometer have good quality data associated with them, the spectrometer's trigger chambers are designed to meet several requirements. In order to associate events in the spectrometer to the respective bunch crossing, the time resolution needs to be better than 25 ns while having a granularity of about one cm. Also, the measurement of the coordinate orthogonal to the one the precision chambers obtain should have a resolution better than 5.0-10 mm, and measurements of the p_T cutoffs while operating in the magnetic field permeating the Muon Spectrometer must be well-defined. To meet these requirements, the barrel region uses Resistive Plate Chambers (RPC's), while the end-caps contain Thin Gap Chambers (TGC's), where the each chamber has two or more layers. The total area covered by the trigger chambers is approximately 9450 m^2, and the trigger chambers have 790 thousand channels combined.

The RPC's are gaseous detectors filled with $C_2H_2F_4$ and have a space time resolution of 1.0 cm $\times$ 1.0 ns. The RPC's have a narrow gas-filled region sandwiched

between resistive parallel plates formed from Bakelite separated with insulating polycarbonate spacers, both of which are two mm thick. A uniform electric field of 4.5 kV/mm allows for the ionization of electrons from the gas mixture to cascade, and the cascade is amplified to produce a 0.5 pC pulse. Each of the chambers is formed from two detector layers along with four readout strip panels and is attached to two support panels. Both ends of the RPC readout strips are terminated to avoid reflections of the signal, thus preserving the RPC's good time resolution.

The TGC's are also multi-wire gas chambers (carbon dioxide and n-pentane) whose wires are set parallel to the MDT wires to provide trigger information, and contain readout strips arranged perpendicular to the wires to provide the second coordinate measurement. The gas region is 2.8 mm thick, and the wires have a radius of 25 μm under an electric potential of approximately 3.0 kV. This allows for the short drift time and good time resolution of the TGC's. Groups of several anode wires, between four and twenty depending on the desired granularity of the η measurement, are sent to a common readout channel and form the trigger signal.

The actual trigger system for the Muon Spectrometer has three levels, similar to many other systems in ATLAS. The Level 1 trigger accepts information at the same rate as the collisions, and has a 2.0 μs latency. It sends data to the Level 2 trigger at a rate between 75-100 kHz. The LVL1 trigger for the barrel uses three RPC stations, two on either side of the middle MDT chambers, and the third next to the outer layer of MDT chambers, and covers the range $|\eta| < 1.05$. The end-cap LVL 1 trigger covers the psudorapidity range $1.05 < |\eta| < 2.4$. The layout of the RPC's and TGC's is shown in Fig. 2.11. The first and second RPC layers in the barrel trigger on low transverse momentum events using predefined coincidence patterns, while high p_T event triggering uses all three RPC stations. Both low and high p_T triggers require coincidence in the stations involved in both coordinate projections

η and ϕ. Due to energy loss in the central parts of ATLAS, the resolution of the momentum measurement is approximately 20% for low p_T events, and 30% with a p_T threshold of 20 GeV. At this threshold, the barrel's coincidence window is 40 cm, and the coincidence window for the end-cap is between five and ten cm. The Level 2 trigger reduces the data stream to a rate of 1.0 kHz by processing and combining the data coming from the triggering detectors and their respective subsystems. The Level 2 trigger improves the Level 1 trigger's p_T resolution by estimating the momentum and invariant mass from data supplied by the RPC's and TGC's [10].

CHAPTER 3

THE TILE CALORIMETER

The ATLAS experiment uses a laminated scintillating tile calorimeter to provide high granularity sampling, energy reconstruction, and good ${p_T}^{miss}$ measurements. The high granularity sampling and energy reconstruction is necessary due to the large number of daughter particles produced by processes from the pp collisions, specifically hadronic jets that penetrate the detector significantly far away from the beam pipe. The scintillating tiles act as the sampling material, while steel plates act as the absorber. Because the EM calorimeter has very good η and ϕ resolution, the granularity of the TileCal is also important, and a segmentation of $\Delta\eta \times \Delta\phi = 0.1 \times 0.1$ was chosen. Since the TileCal is made up of steel plates and scintillating that are cyndrically symmetric, the design is made such that the TileCal could be put together as 64 separate azimuthally wedges, thus enabling assembly of the detector in a safe and cost effective manner. A complete description of the ATLAS Tile Calorimeter can be found in the ATLAS Tile Calorimeter Technical Design Report [11].

Like most of the sub-detectors in ATLAS, the TileCal is separated into three physical sections, two end caps and a long barrel section. The central barrel of the TileCal is referred to as the Long Barrel (LB), and is divided in half so that each side is labeled A side and C side corresponding to the coordinate system described in chapter 2, section 1.1. Though the TileCal LB has two sides, there is not a physical division between the two sides. The end caps, known as the End Barrels (EB's), also house the Intermediate Tile Calorimeter (ITC), with respective A and C sides. Between the LB and the EB, the TileCal has a gap region of approximately 60 cm to

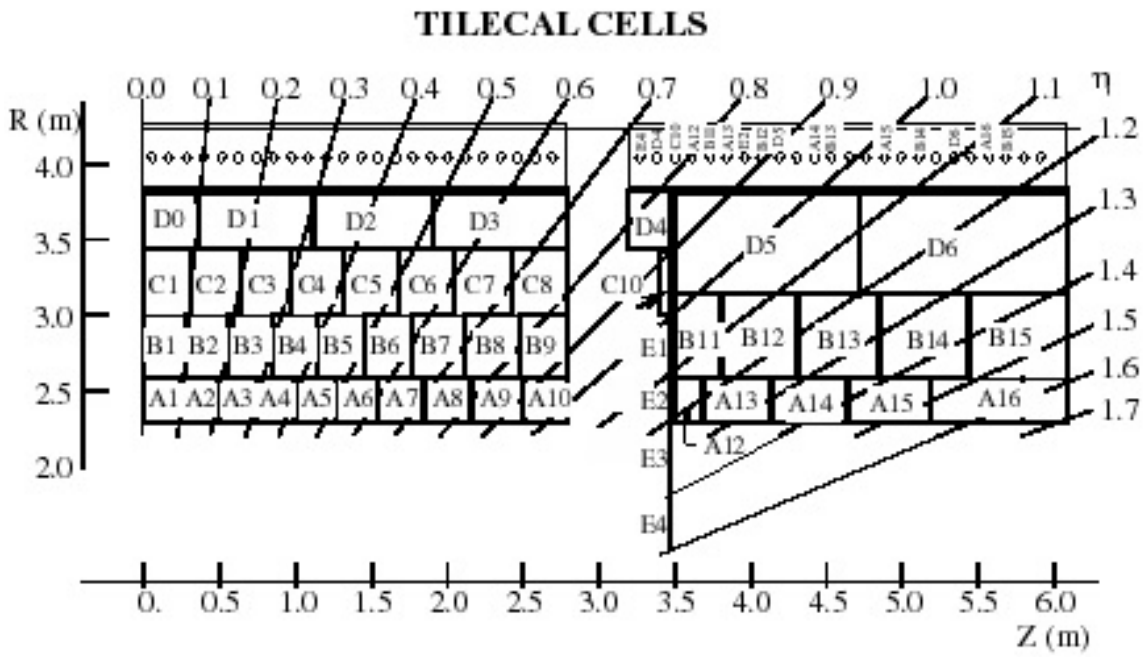

Figure 3.1. The geometry of TileCal modules on A-side.

allow for access to the inner parts of the detector during maintenance periods, and also to allow cabling to reach the LAr and ID systems. The calorimeter has an inner radius of 2.28 m and an outer radius of 4.23 m, with the LB's length along the beam axis equal to 5.64 m and the EB's having a length of 2.91 m. The barrel covers the eta region -1.0 $< |\eta| <$ 1.0, while the end barrels each cover the region 0.8 $< |\eta| <$ 1.7. The ITC's gap scintillators cover the region 1.0 $< |\eta| <$ 1.2, and the crack scintillators cover the 1.2 $< |\eta| <$ 1.6 region.

3.1 Module Design

Each of the three sections of the TileCal are subdivided into 64 physically separate azimutal wedges, called modules, that mechanically divide the barrel and end-caps into segments of $\Delta\phi = 0.1$. Each module is comprised of sub-modules that are the laminated scintillator-steel wedges, layered along z, with a girder on the outer

surface to hold the layers together. Within the gaps of the iron layers of the modules, scintillating plastic, whose radial length is between 97 mm and 187 mm, is placed parallel to the azimuthal plane. These modules are divided into three radial sample layers in the data, and also in towers of $\Delta\eta = 0.1$ for the two inner sample layers, and $\Delta\eta = 0.2$ for the outer sample layer, based on the plastic tiles' geometry. The divisions of the layers and towers for a wedge in the LB, EB, and ITC of the A-side of the TileCal can be seen in Fig. 3.1, and a schematic of a single module is shown in Fig. 3.2.

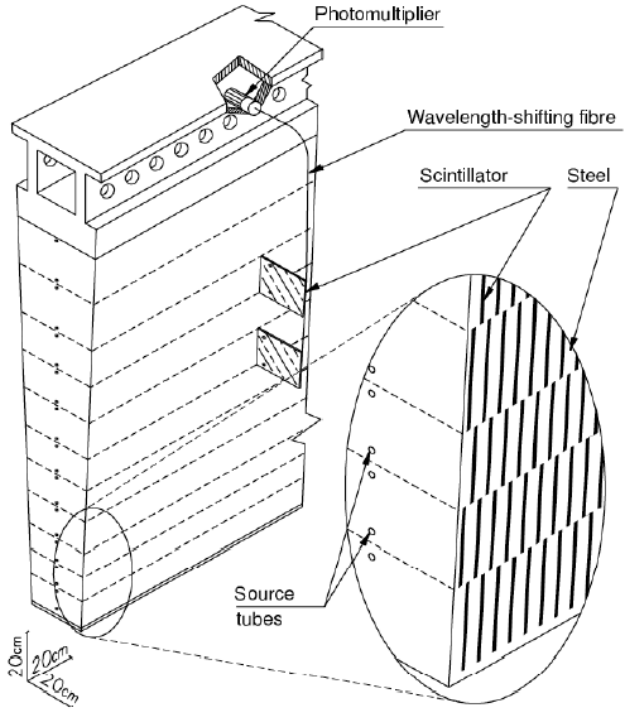

Figure 3.2. TileCal module schematic.

On the azimuthal exterior of the modules, pairs of wavelength shifting fibers run radially to collect light from the plastic tile's azimuthal edges. All of the tiles along a

z plane in a module are read by the same pairs of fibers. Readout cells are groups of tiles whose fibers are grouped together and fed into the same PMT. This segmentation gives the TileCal its ability to determine the three-dimensional locations of a particle or jet. Most of the plastic tiles, the steel material, the fiber optic cables, the wrapping for the tiles, and the PMT's are commercially available (or the materials to create them are commercially available), such that the many institutions that participated in the construction of the modules were able to conform to the same standard, which in turns allows the modules to have the necessary uniform response, since a non-uniform tile response degrades detector performance.

3.1.1 The ITC

To enable active coverage in the region between the LB and EB's, the ITC was inserted into the gap. It extends down into the narrow crack region behind the LAr system, where the cryostats for the barrel and end-caps are located. Due to the tight spatial constraints of the crack region, only the outer half (radially) of the ITC's active material, called the gap scintillators, is similar to the makeup of the rest of the TileCal. The innermost half is made of only scintillating material, and those tiles are referred to as crack scintillators. As such, the crack scintillators do not have any absorber material in front of them like the steel plates in the rest of the TileCal, save for a thin aluminum sheet to prevent light leaks into the scintillators and the aluminum boxes that hold the tiles in place. A schematic of the ITC sub-modules can be seen in Fig. 3.3

The crack tiles themselves, known as the E Sample Layer, are wrapped in Tyvek paper and black electrical tape to minimize light leakage. The two sets of tiles furthest away from the beam pipe, layers E1 and E2, have grooves etched into their surface to facilitate the placement of the fiber optic cables that connect the tiles to the PMTs

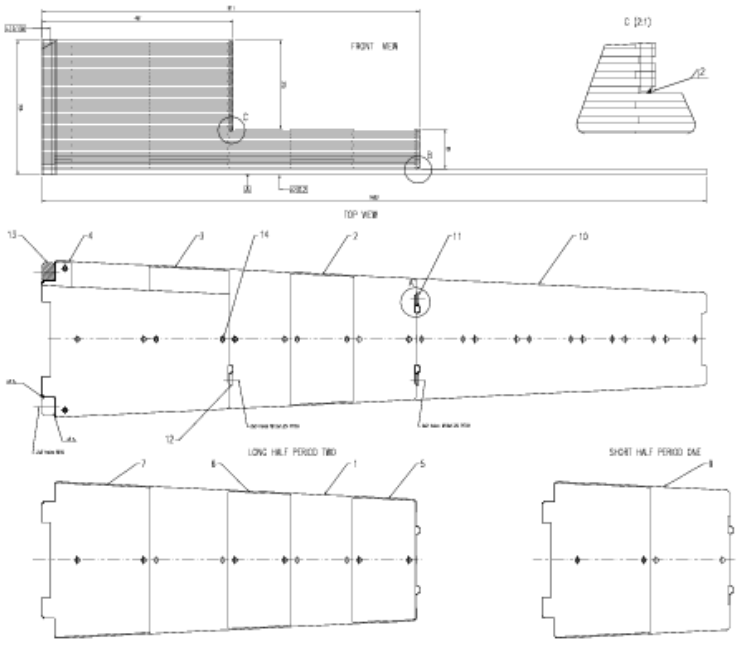

Figure 3.3. ITC sub-module schematic.

housed in the fingers of the EB. The tiles closer to the beam pipe in layers E3 and E4 have fibers along the azimutal edges, similar to the tiles in the other parts of TileCal; however, these tiles have multiple fibers per tile to collect photons, as opposed to a single fiber on each side. The boxes housing the tiles are made of aluminum and are attached to the lead structure that backs the gap cells and connects the ITC to the EB's.

3.1.2 Scintillation

As charged particles pass through the TileCal scintillating plastic tiles, they the atoms in the plastic and the resulting de-excitation produces scintillated light. The plastic lattice is polystyrene and has a binary scintillator, the combination of dopants being a primary fluor paraterphenyl (PTP) and a secondary fluor 1,4-bis(5-phenyloxazol-2-yl) benzene (POPOP). Each tile is wrapped in reflective Tyvek 1055B

paper, which has a reflectivity range of 95%, so that the photons are contained within the cells until they can enter the light guides, which are wavelength shifting fiber optic tubes, on the edge of the tile (or in the ITC crack tile's grooves).

The initial radiation produced by the particles passing through the polystyrene is in the 240-300 nm wavelength range, which is then absorbed by the primary fluor molecule PTP. The PTP re-emits the light in the 320-400 nm spectrum, which is then absorbed by the POPOP dye that converts the light to a longer blue wavelength. The emitted light has wavelengths in the range between 240-400 nm, so for the PMT's to be optimally used, the light is shifted along the light guide fibers to the wavelength the PMT photocathodes are most sensitive to (between 480-495 nm), reaches the PMT's quickly, and has low attenuation over the length of the fibers. Like everything else in the ATLAS detector, the fiber optic cables are manufactured to be radiation resistant so that their degradation over the operating life of the detector is minimal and does not affect the quality of the signal too much. A small fraction of the re-emitted photons in the light guides are re-captured and continue to propagate to the PMT's thanks to the total internal reflection of the fibers. The photons travel along the light guides until they reach the photomultiplier tubes, where they are converted into a detectable electronic signal. The truncated end of the fibers have been aluminized so that the photons are reflected back toward the PTM's, and between the photocathode and the fibers, a light mixer is inserted to optimize the detection uniformity.

3.2 Electronics and PMT's

In the girder structure that holds the TileCal modules in place, each module of the TileCal contains drawers for the front-end electronics and PMT's, located on the outer radius of the TileCal system. Facing into the gap regions, each drawer has a finger, and a steel box extending into the gap region that contains a low voltage power

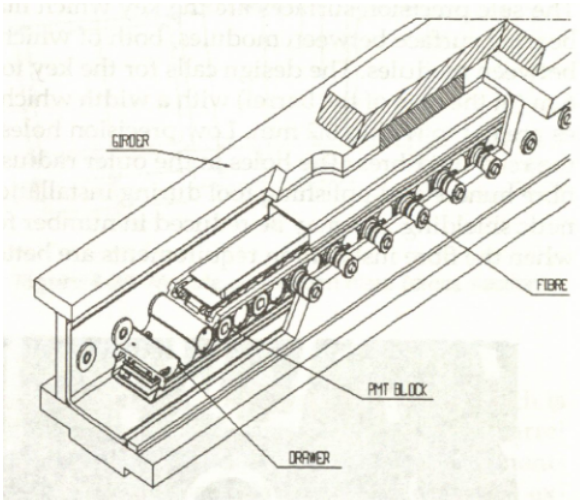

Figure 3.4. Module electronics schematic.

supply to power the electronics in the drawers. The drawers run the length of the sides of the LB and EB, with steel plates in the gap region that can be removed, so that the electronics may be pulled out and/or extracted when refurbishing is needed and access is available. Fig. 3.4 shows the general layout of the electronics in the girder structure.

The PMT's convert photons received from the light guides into an electronic signal via the photoelectric effect. The electron signal produced from the photocathode of the PMT is increased by having the electrons go through several dynode stages of increasing electric potential. The dynodes are made from material that has a low work function for an easier gain in signal, and as the electrons accelerate through the stages, the likelihood for electrons to be released by the dynode increases. This cascade of electrons through the PMT allow the original photon signal to be amplified by a factor of 10^4 to 10^7, enough for electronics to read the signal [12]. The amplification factor for a PMT is determined by using standard sources of photons and determining the output signal of the PMT, over the range of the PMT's operating voltage. In this manner, the number of photons produced in the scintillating plastic

tiles of the calorimeter can be counted, and the energy the TileCal system absorbs from the particles that traverse it can be determined for analysis.

The analog signal from the PMT is sent to digitizer boards located at the end of the drawers. For the TileCal, a Level 1 trigger requires two signals from the first and second sample layers, and one from the last layer. After a Level 1 trigger accept, the digitized information is sent to the Read Out Drivers (ROD's). The ROD's include bunch crossing information and apply calibration corrections for each PMT signal; they then preprocess and format the data. Finally, the data is passed to the read-out buffers for Level 2 trigger processing.

3.3 Detector Environment

The *pp* interaction rate is the dominant radiation source for the ATLAS detector, and most of the particles produced from the central proton collisions are absorbed in the calorimeters, especially the TileCal. These highly energetic particles shower (decay through various production channels) as they enter the detector material until the energy and the daughter particles are absorbed, while neutrinos and muons escape the detector. The neutral particles and electrons produced from the photons scatter many times before finally being captured, creating a low energy background of a uniform isotropic gas. The dose rate for most of the TileCal volume per year is below 20 Gy, although the region around $|\eta| < 1.2$ receives a maximum annual dose of 38 Gy. Because of these radiation levels, the TileCal was designed to have low degradation in the scintillating material and fiber optic guides over the first ten years of LHC operations, as well as having radiation hard front-end electronics to keep malfunctions and failures at a minimum during operations.

Since roughly 25% of the magnetic flux from the solenoid passes through the active parts of the calorimeter along with a small contribution from the toroidal sys-

tem, the material and electronics are designed to tolerate these fields. The maximum magnetic field strength in the scintillators is roughly six mT, which increases light output by about 1.0%, and in the gap regions, the field due to the torroid system is approximately 120 mT. To block the majority of the field in the gap region from the electronics, the drawers are capped by ten cm thick iron plates. Owing to this design, and the fact that the majority of the residual magnetic flux is confined to the girder structure, the field strength in the vicinity of the PMT's located near the gap region is reduced to about 20 Gauss, which in turn brings the total field level here up by 50%, but limits the degradation of the signal to approximately 1.0%. However, the PMT's are designed with shielding of iron and μ-metal cylinders rated for shielding against 500 Gauss fields.

In addition to the magnetic fields and high levels of radiation, the TileCal has to cope with determining how much energy has been lost to the dead material in front of the detector. The dead material is primarily the LAr cryostat, and offline processing reconstructs the energy loss through the known thickness of the dead material. The thickness of the calorimeter is also important for overall performance. As such, the TileCal barrel has to be sufficiently thick to reduce the punch through of hadronic jets into the Muon Spectrometer by containing the jets through absorption. In addition to absorbing the hadronic showers, the measurement of the missing transverse energy ${E_T}^{miss}$ is also greatly affected by the TileCal's thickness and acceptance. Muon energy absorbed by the TileCal greatly affects the momentum resolution of the Muon Spectrometer for low energy muons, but since the calorimeter can identify the muons, corrections can be applied to account for and identify the absorbed muons.

3.4 Muons in the TileCal

Since this analysis focuses on how the individual cells of the TileCal respond to muons, understanding the whole of the calorimeter's response to muons is very important. For low p_T muons (under 2.0 GeV/c), the TileCal absorbs the muons, and as such, must be able to identify them, since it is the only system able to do so if the muons cannot make it to the tracker in the Muon Spectrometer. Above this threshold, the muons do make it to the Muon Spectrometer, and they are measured there. However, muons whose p_T is between 2.0 GeV/c and 5.0 GeV/c have a large fraction of their energy absorbed by the LAr and Tile calorimeters, so the calorimetric measurements of the muons are very important to correct the muon spectrometer's momentum measurement. The muons in this p_T range are not truly minimally ionizing, as they deposit additional energy into the calorimeter, but, above this range, the muons deposit a uniform amount of energy regardless of their momentum and are known as Minimum Ionizing Particles (MIP's). Because of this, muons are an efficient tool to analyze the TileCal.

Compared to hadronic showers, the light emitted (and thus the signal) due to muons traversing the scintillating material is small, so the TileCal must have a large dynamical range over which it reads out information. The spectrum of the muon's energy loss is approximately a Landau distribution, or more accurately a Landau convoluted with a Gaussian. Because the shape of the distribution is known, the number of photo-electrons can be determined based on a fit to the energy distribution. The light yield, or number of photo-electrons emitted per GeV, has been determined to be efficient above 48 photo-electrons per GeV for a layer, but the light yield per for an individual cell will be much lower, approximately 10 to 20 photo-electrons per GeV. The calorimeter should also have a uniform response to muons in z, η, and ϕ for the signal/<signal>, and normally this signal response has an root mean square of

less than a couple percent. This analysis will determine the quality of the individual cells of the TileCal by verifying the light yield and the uniformity of the response to muons from collisions in η and in ϕ.

CHAPTER 4

ANALYSIS

Since high energy muons are MIP's, the amount of energy muons deposit as they pass through (thin) material is independent of the actual energy of the muons. This makes them useful tools for checking the response of the TileCal cells. To ensure that the study is accurate, the tracks of the muons are reconstructed through the calorimeter, and their path lengths through TileCal modules are calculated. The energy, path length, and dE/dx response of the cells in the modules are determined by excluding noise in the cells via the selection of tracks above the pedestal with a good path length calculation. The response of each layer is analyzed and compared to Monte Carlo simulations to determine if there is an irregularity in the physical data or in this analysis.

Once this has been done, the quality of an individual cell's response to the muons can be determined by analyzing the number of photo-electrons produced as the muons traverse the scintillating material in the cell. This value is determined by fitting the cell's energy distribution to a Landau curve and squaring the ratio of the energy distribution's most probable value (MPV) to the width of the Landau peak σ. For this study, only cells in the E and C10 layers will be considered.

4.1 Muon Data

In collision events, isolated low p_T muons originate from pion and kaon decays; with increasing transverse momentum, c and b mesons are the largest contributors, and at high transverse momentum, W and Z boson processes dominate. The corre-

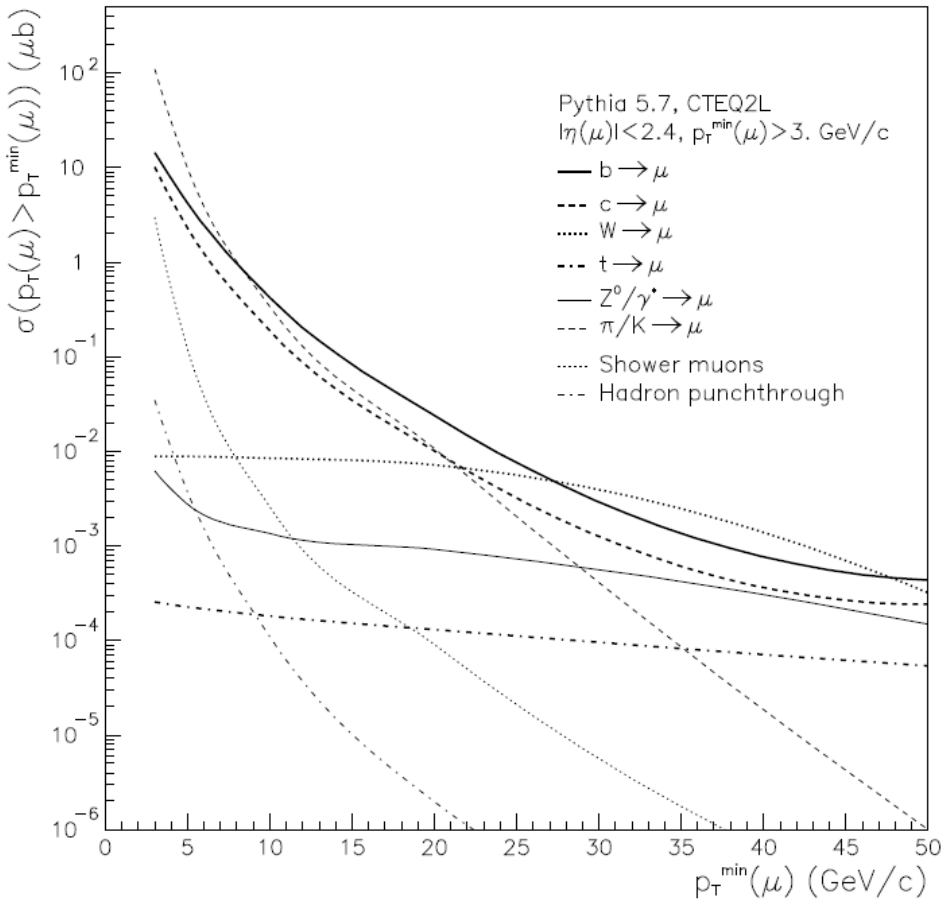

Figure 4.1. p_T vs. integrated cross-section for inclusive μ production.

lation between the p_T threshold and the integrated cross-section for inclusive muon production at the LHC is shown in Fig. 4.1. The data for this study are from the E and H run periods at the LHC. The MC data are simulated $b\bar{b} \rightarrow \mu$+X events where X are particles light enough to be produced by the b meson and still conserve lepton and other quantum numbers. The p_T distribution for the MC data (magenta line) is compared to the p_T distribution of the collision data (black line) in Fig. 4.2. Based on the p_T of the muons and their associated cross-sections, most of the muons are from pion, kaon and b meson decays. Although the MC data have a maximum higher than the first local maximum in the collision data, this does not necessairly signify that

the contribution from b/c meson decays is more than the pion/kaon contribution, since the MC data is exclusively due to b meson production. As such, the MC p_T distribution should be scaled via the branching ratio for b meson production, which has not been done here.

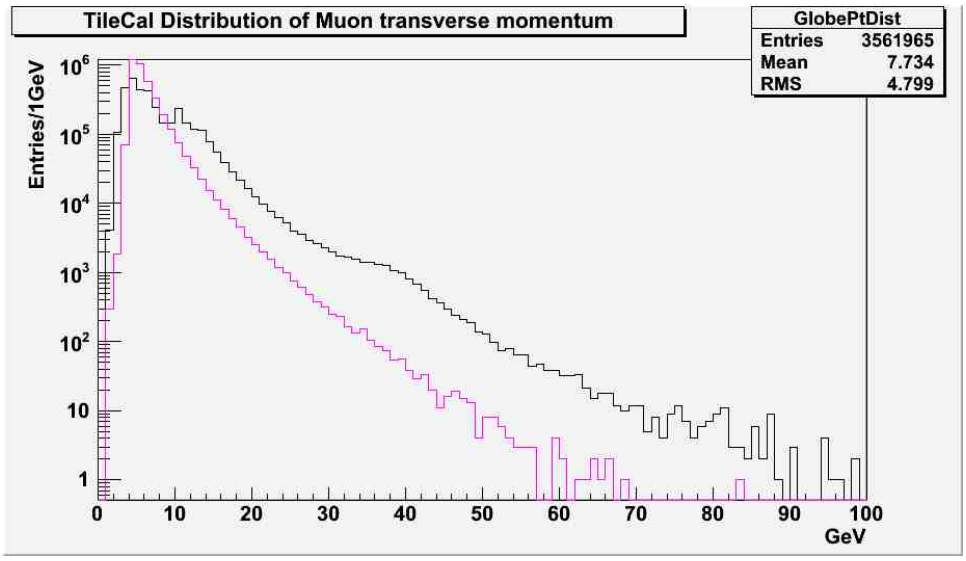

Figure 4.2. p_T for Collisions (black) and MC data (magenta).

In order to select muon candidates from the collision and MC data that reach the Muon Spectrometer, the muons are required to have a track momentum between 4.0 GeV/c and 100 GeV/c, as the Muon Spectrometer is efficient for triggering in this momentum range. The candidates are further required to be muons that have a single reconstructed track that passes through the Muon Spectrometer, so that only isolated muons are analyzed. The transverse momentum is not restricted; thus all processes that produce single muon events are considered, and the full geometric range of the detector can be analyzed [8].

4.1.1 Muon Trigger Efficiency

The trigger used to filter the data from the collisions into muon candidate events is the CombMuonID trigger. This trigger enforces the muons to have adequate reconstruction in the ID, with a minimum number of hits between the TRT and SCT systems. Additionally, the muons must pass through and have good resolution in the muon spectrometer. Near $\eta = 0$, specifically $|\eta| < 0.2$, the efficiency of the reconstruction is lower due to the reduced amount of sampling material. This also affects the path length calculation, since muons with very low p_T pass through fewer tiles in the cells, which causes them to have fewer extrapolation points needed for the calculation. In addition, the trigger is less efficient in the range $0.8 < |\eta| < 1.2$, affecting the statistics for ITC cells and cells close to the gap region [13]. This also affects the path length calculation in the form of edge effect errors.

4.2 Track Matching

Table 4.1. Track Matching Values used for $|\eta_{track} - \eta_{cell}|$ in the TileCal

Layer (Cell Type)	12 (LB A)	13 (LB BC)	14 (LB D)	15 (C10)
$\lvert\eta_{track} - \eta_{cell}\rvert$	0.05	0.05	0.10	0.12
Layer (Cell Type)	16 (D4)	17 (E1)	17 (E2)	17 (E3)
$\lvert\eta_{track} - \eta_{cell}\rvert$	0.12	0.05	0.05	0.01
Layer (Cell Type)	17 (E4)	18 (EB A)	19 (EB B)	20 (EB D)
$\lvert\eta_{track} - \eta_{cell}\rvert$	0.01	0.05	0.06	0.10

Because the cells that give the detector its granularity are to be analyzed, muons are restricted to be within the volumes of the cells. To ensure that the event is within the cell currently under consideration, the track matching parameters

$r_\phi < |\phi_{track} - \phi_{cell}|$ and $r_\theta < |\eta_{track} - \eta_{cell}|$ are determined, where $\phi_{track}(\eta_{track})$ is the azimuthal position of the track (psudorapidity of the track) and $\phi_{cell}(\eta_{cell})$ is the is the azimuthal position of the cell (psudorapidity of the cell). Because all of the modules and their cells have an azimuthal coverage of $\Delta\phi \leq 0.1$, the track matching parameter $r_\phi < 0.05$ is used for all of the TileCal cells.

Due to the differing geometries of the cells, as seen in Fig. 3.1, their η coverage varies between different layers. As such, the track matching parameter r_η is determined on a layer-by-layer basis. The cells in the long barrel and end-cap layers can be grouped into three sets with specific r_η values. Since the coverage of the A and BC layers of the LB and the A layer of the EB is the same, $\Delta\eta \leq 0.1$, the acceptance of the track matching parameter is $r_\eta < 0.05$. For the D layers in both the LB and EB, $r_\eta < 0.1$, since their $\Delta\eta = 0.2$. The B layer in the EB has an $\Delta\eta$ coverage slightly larger than 0.1, so its track matching parameter is taken to be $r_\eta < 0.06$. The same procedure is applied to the ITC. Table 4.1 gives the $|\eta_{track} - \eta_{cell}|$ restrictions for the different cell types in the LB, the ITC, and the EB.

4.3 Signal Isolation

In order to remove extraneous noise that the track matching selection missed, the energy distribution for each layer is plotted to acquire an understanding of the pedestal, and, from this, a noise cut is determined. The pedestal of a cell is information (electronic noise) received from the PMT's through the front end electronics in the absence of a signal (an event passing through the cell). When trying to study the average response of a cell, the pedestal skews the cell's energy distribution and therefore must be removed. The raw energy distribution for LB Layer A is shown in Fig. 4.3, indicating the signal, the pedestal, and the noise cut. The procedure is

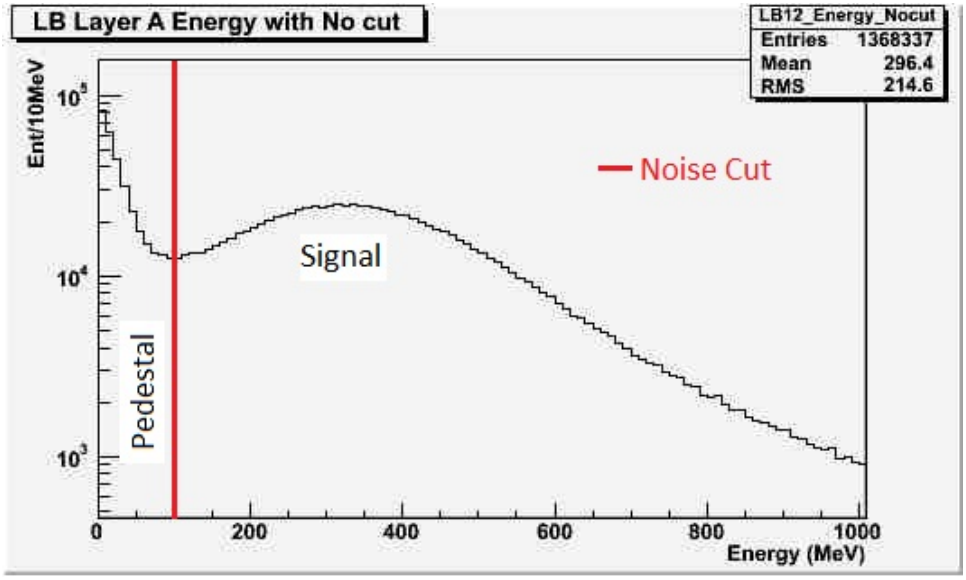

Figure 4.3. Unaltered Energy Distribution in LB Layer A.

replicated for each layer in the TileCal, and the resulting noise cut for each layer is given in Table 4.2.

In addition to removing the pedestals, to ensure the muon tracks under study are actually due to muon events, the LAr calorimeter is used to remove fakes from highly energetic electrons that are mis-identified as low energy muons. To remove these electrons, the correlation of the energy deposited in the LAr layers with respect to the energy deposited in the TileCal barrel for a given track is analyzed by plotting the energy of cells within a cone-size of $\sqrt{(\phi_{track} - \phi_{cell})^2 + (\eta_{track} - \eta_{cell})^2} \leq 0.05$ in the LAr against the energy deposited within the TileCal layers. It has been determined that if the energy deposition in the second layer of the EM calorimeter is $\leq$ 700 MeV, there is a strong correlation to muons in the TileCal barrel, and this restriction removes most muon fakes. The correlation between the second layer in the LAr and the first layer of the TileCal is shown in Fig. 4.4, where the x-axis is the energy

Table 4.2. Pedestal Removal Value for each Layer in the TileCal

Layer	LB A	LB BC	LB D	C10	D4	E	EB A	EB B	EB D
Noise Cut (MeV)	100	100	100	50	100	20	100	100	150

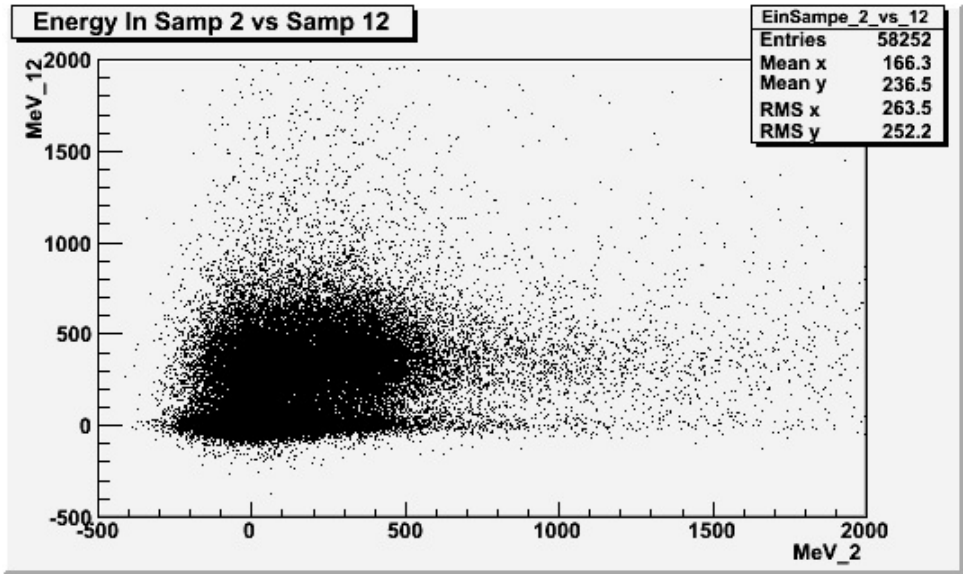

Figure 4.4. Correlation between LAr Energy and LB Layer A Energy.

deposited in the second layer of the LAr calorimeter and the y-axis is the energy deposited in LB Layer A.

Since the ITC does not have corresponding coverage in the LAr system, only analyzing the energy distribution is used to remove the pedestal. Because the EM Calorimeter in the EB's is very noisy and not as sensitive to the $|\eta|$ region of the EB TileCal, again only the energy distribution is analyzed to remove the pedestal.

4.3.1 Path Length Calculation

To understand the uniformity of the response of different sampling layers, knowing the energy distribution is not sufficient. This is due to the fact that the cells in different layers have various sizes, muons can pass through more than one cell in a

layer, and within some of the layers (primarily layer A in the EB's) there are "special" asymmetric cells (see Table 4.3) that need to be more closely analyzed. In order to account for the variation in cell sizes, the energy deposition per unit length (dE/dx) where x is the path length (not the coordinate) is determined by extrapolating the path length of the track in each cell. Using dE/dx also has the added benefit of reducing any of the noise left over from the pedestal that was not successfully removed via the energy cuts. In general, the path length should be positive. If it is not, then the track is considered to have a bad extrapolation and is omitted. The algorithm to calculate the path length was developed by Dr. Giulio Usai et al, and is used for many other analyses involving the ATLAS TileCal system.

Table 4.3. Asymmetric Cell Locations in Sample Layer 18 (EB A)

Module Number	36	37	60	61
ϕ_{cell} value	-2.79798	-2.69981	-0.53996	-0.44179

To check whether the path length calculation is accurate, the path length is plotted against the η_{track} and E_{sum} for each sample layer. In the first case, the geometry of the cells in η should be correct along with the value of the path length being within the range of the cell geometry. Figure 4.5 (LB Layer A η vs. path length) is given as an example: the width of each cell can be seen to have a width of $\Delta\eta = 0.1$. In the second case, the response of the layers should be linear over the central range of the cells. Figure 4.6 (LB Layer A path length vs. energy deposition) is given here as an example. For the other layers, the graphs are available in Appendix A.

The current extrapolation program works well for both the LB and EB TileCal, but there are issues with the ITC path length calculation currently that are being

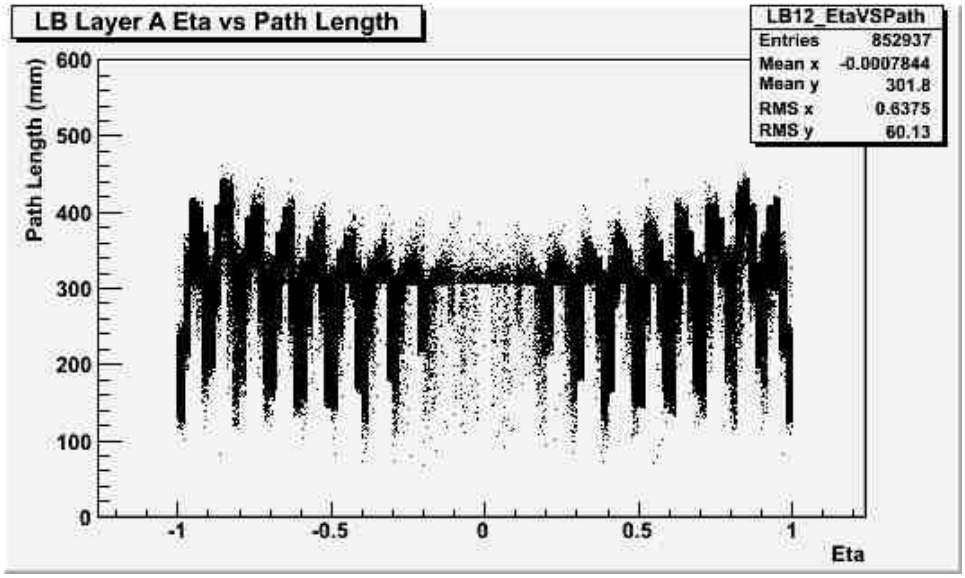

Figure 4.5. Long Barrel Layer A Eta vs. Path Length.

analyzed, along with errors in calculations for cells near the gap region (edge effects). The edge effect errors affect the ITC and the A and B layers of the barrel layers. Once the isolated muon tracks have been appropriately selected, and the path length calculation verified, the response of the layers in the TileCal can be analyzed in η and ϕ.

4.4 Light Yield of ITC C10 Cells

Since the ITC C10 layers are thin cells, they can be analyzed for their light yield. The C10 layer cells are designed like standard cells, but they only have three scintillator tiles. Because the composition of these cells is thin material, the energy deposition per charged particle (muons for this study) should be described by a Landau curve, given sufficient statistics, as shown for the C10 C-side module number 7 cell in Fig. 4.7. The light yield of a cell can then be determined by taking the square of the ratio of the Most Probable Value (MPV) of the normalized Landau curve to

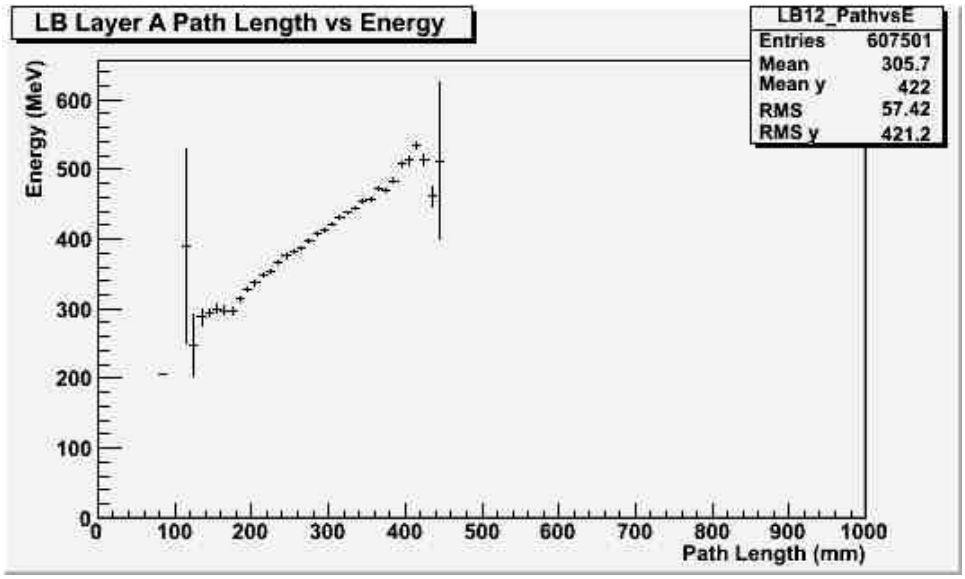

Figure 4.6. Long Barrel Layer A path length vs. energy deposition.

the width σ of the curve. This value, called the yield, is proportional to the actual light yield, and, once determined, the yield for each cell is plotted with the other cells with respect to the layer and tower. Any cells determined to have a low light yield (yield < 10) can then be singled out and analyzed in detail in a future analysis.

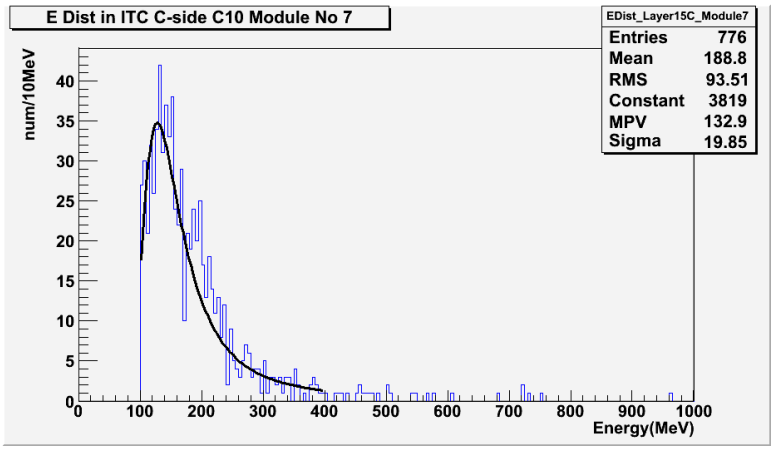

Figure 4.7. Normalized Landau curve fitted to the energy deposited in a cell.

The results of the analysis are discussed in the next chapter.

CHAPTER 5

RESULTS

5.1 Energy and dE/dx Distributions

With the selection criteria described in Chapter 4, the pedestal is removed and the energy per unit length (dE/dx) deposited in the cells can be analyzed. The signal for the layers can be seen clearly in the energy distribution as a convolution of Landau and Gaussian curves, and the dE/dx distribution for each layer is given. The plots for LB Layer A are shown in Fig. 5.1. Plots for the other layers are provided in the appendices.

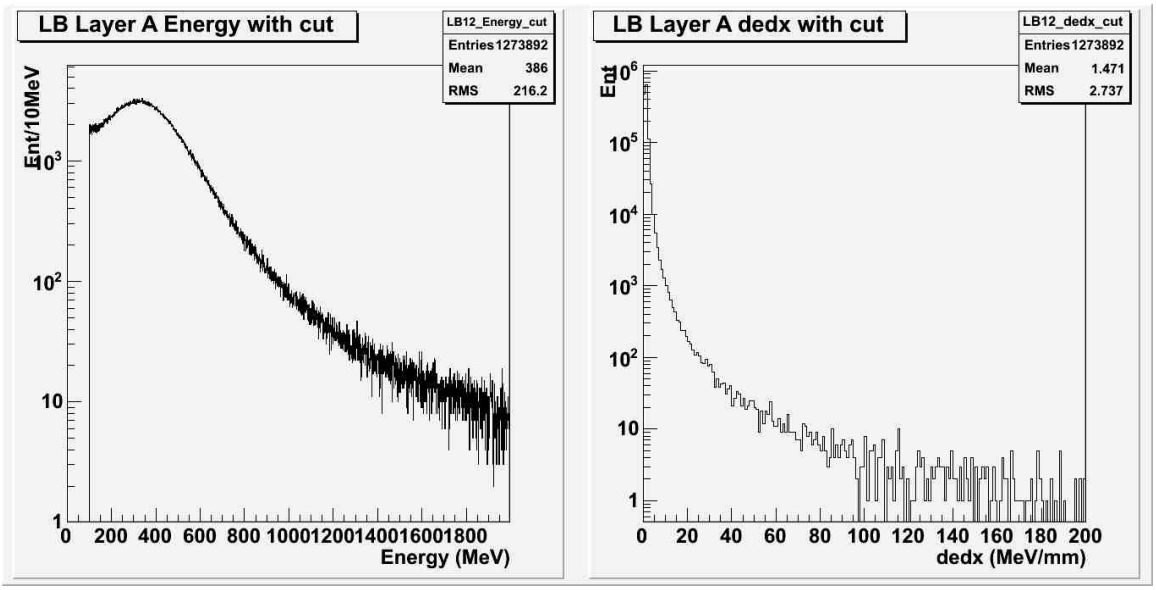

Figure 5.1. Energy and dE/dx for LB Layer A.

5.2 Layer Response in ϕ and η

Using the same selection criteria, the response of the layers can be determined: in η, integrated over ϕ (right side), and in ϕ, integrated over η (left side) as shown in Fig. 5.2. The MC result is shown in magenta, while the result from the collision data is shown in black. The binning of the ϕ response plots is with respect to the modular divisions (64 bins), and the binning for the η response plots is established such that the bins correspond to towers. For the D Layers, the binning is enlarged from towers to cover the range of the D cells. Muons close to $\eta = 0$ have a lower trigger efficiency as discussed in the Analysis chapter (section 4.3). However, this does not affect phi response uniformity.

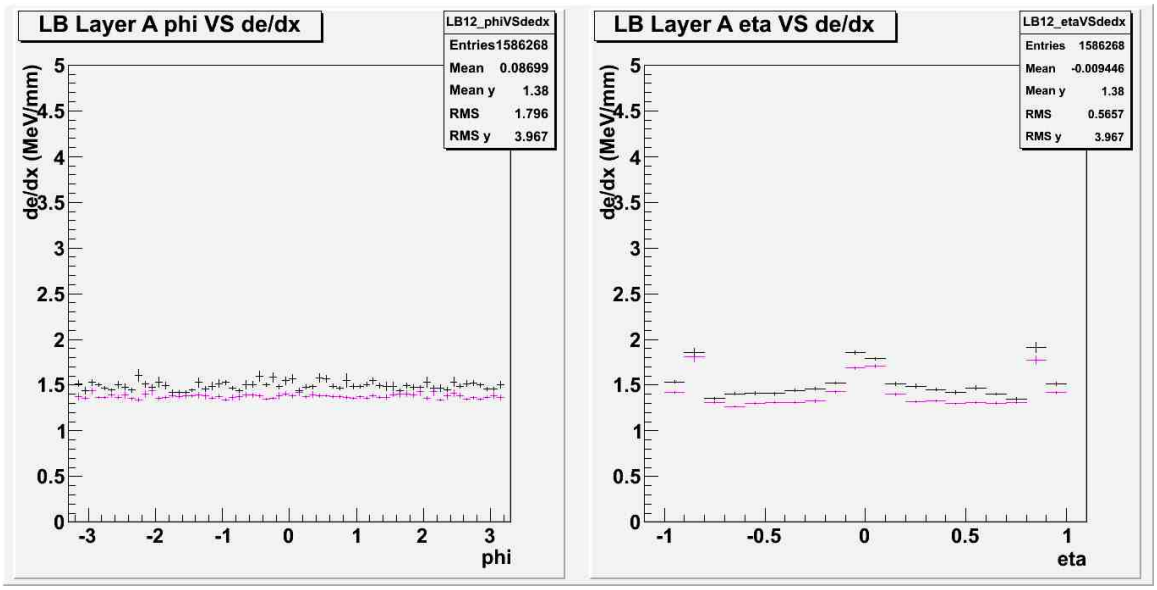

Figure 5.2. Response for LB Layer A in ϕ (left) and η (right).

As can be seen in Fig. 5.2, LB Layer A has a uniform response in ϕ (left), and the response is uniform in η, with the exception of η near zero. The difference between the response of the MC and collision data is due to the processes that produce the

muons. Since a large portion of the collision muons are from K/π decays (see Fig. 4.2), the average energy deposition of those muons is somewhat larger since they are not truly MIP's. The muons in the MC data are MIP's, so the energy deposition is lower for this reason. The average response of each layer is given in Table 5.1.

Table 5.1. Average Response (MeV/mm) in ϕ and η for each Sample Layer

Layer	ϕ	η
LB A	1.380	1.380
LB BC	1.283	1.283
LB D	1.317	1.317
ITC C10	3.053	2.708
ITC D4	4.291	2.311
ITC E	27.85	27.85
EB A	2.119	2.119
EB B	1.966	1.966
EB D	1.323	1.323

The response of the other layers in ϕ, with the exception of ITC D4 and ITC E layers, is very uniform and the response in η is relatively uniform for the LB and EB. Exceptions exist for the η uniformity around $\eta = 0$ for the long barrel, and for towers bordering the gap region in both the long barrel and end-cap. The plots for the other layers are available in the appendices. The non-uniformity of the end-cap towers next to the gap region is due to edge effects in the calculation of the path, an issue which is in the process of being corrected. The ITC has a very high response, specifically in the E layer due in large part to the fact that the material is much thicker (2.5x) scintillating tile with no steel absorber. However, as evidenced by the slight non-linearity of the path length vs. energy plots for the ITC layers (specifically D4 and E layers), the path length calculation is not completely accurate, an issue that needs to be corrected. Although there are much fewer statistics in the ITC since

these layers are only one cell thick (with the exception of E), this fact should not significantly affect the linearity of the path length versus the energy deposited, just the uniformity.

5.2.1 Response of Special Modules in the End Barrel

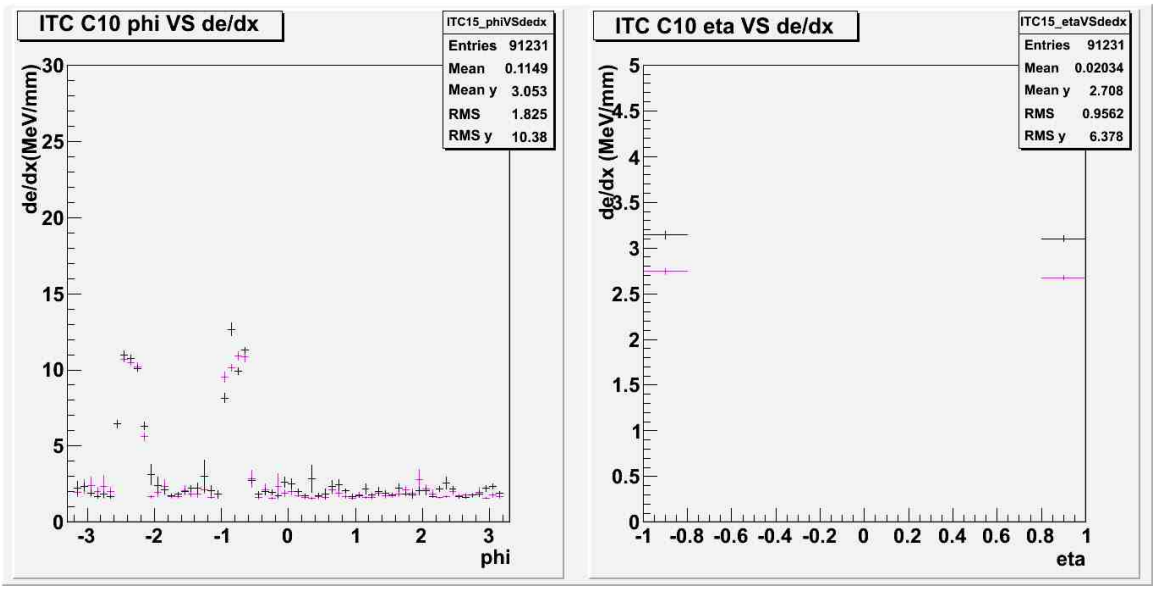

Figure 5.3. Response for ITC Layer C10 in ϕ (left) and η (right).

Figure 5.8, located at the end of this chapter, shows the response of each of the layers in the EB Layer A, with the special asymmetric cells outlined in red. All of the cells are close to the average uniform response for their tower, with a few exceptions. The A12 cells (top pair in the figure) is not nearly as good as the uniformity of the other towers in the layer, but the statistics for A12 are 60% or lower than the statistics for the other towers. The asymmetric cells have individual responses similar to those of the other cells in the layer, which indicates their asymmetric nature does not diminish the quality of the data derived from them. The few cells with low responses

(A-side: A16 module 6; C-side: A14 and A16 module 63, and A16 module 5) indicate that there are potential, outstanding issues with those cells, such as inefficiencies with the PMT's (possibly due to a low voltage).

5.2.2 Response of ITC Layer C10

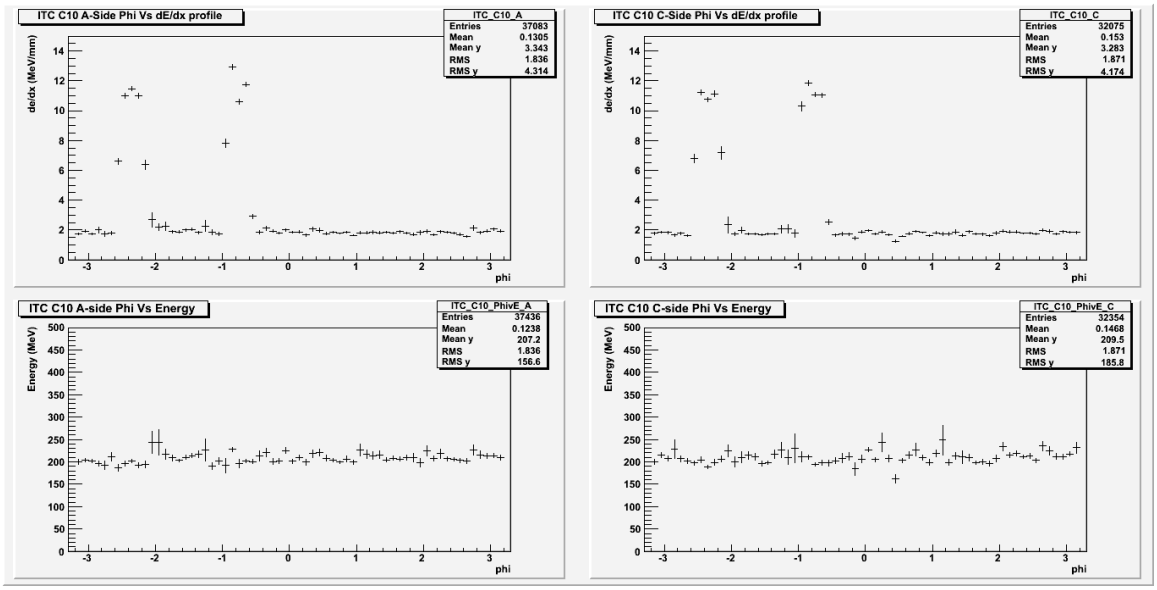

Figure 5.4. C10 cell response (top) and energy deposition (bottom) in ϕ.

As can be seen in Fig. 5.3 (left), the response of the C10 cells is generally uniform in ϕ, except in the regions of -2.6 $< \phi <$ -2.1 and -1.0 $< \phi <$ -0.6, for both the A-side and C-side. By comparing the dE/dx response of the cells with the actual energy deposited in them, see Fig. 5.4, we see that the non-uniformity does not exist in the cells' energy deposition. Since the energy deposition is uniform, the non-uniformity of the dE/dx response shows that there is an error in the path length calculation for these cells that must be fixed. The response in η is relatively uniform, although there are only two sets of cells, one set in each gap.

5.2.3 Response of ITC Layer D4

The D4 layer has the fewest statistics out of all the layers in TileCal. The response of the D4 layer in the ITC is much higher than, and not as uniform as, the barrel layers. The ϕ uniformity, as seen in Fig. 5.5 (left), is uniform within the range of the statistical errors, but the performance of the response can be tightened and possibly increased with better statistics.

The η response is closer to that of the barrel layers, but, as evidenced by Fig 5.5 (right), the edge effects cause deviations in the uniformity of the cells. However, these are singular cells, one set in each gap region, so the response should be uniform on each side.

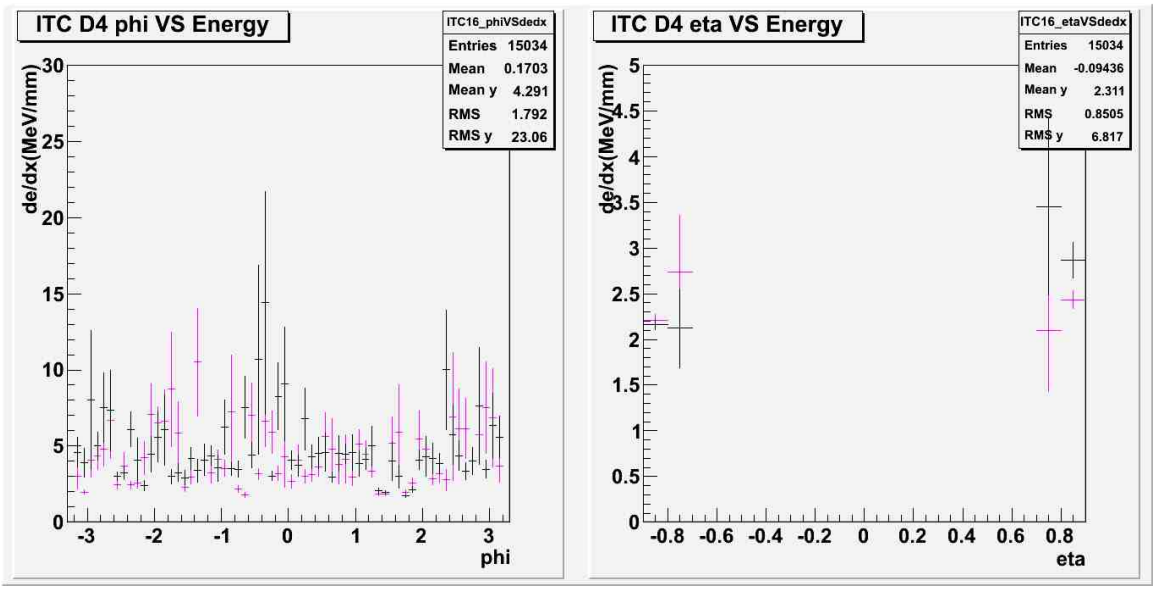

Figure 5.5. Response for ITC Layer D4 in ϕ (left) and η (right).

5.2.4 Response of ITC Layer E

The response of the E layer of the ITC is very high in ϕ, seen in Fig. 5.6 (left), higher by a factor of 9 with respect to the other EB layers, and by a factor 20 with respect to the barrel layers. The reason for this is the tile thickness, and also a different light collection geometry, as has been previously discussed, not the path length algorithm, as evidenced by the linearity of the path length vs. the energy deposition (Fig. B.16 in Appendix B). The uniformity of the layer in ϕ is good, but it is more constructive to look at the individual towers. The actual response (see Fig. 5.6 (right)) of the individual towers in E show that the E3 and E4 tiles are the source of the high average response for the layer. The individual towers are considered below.

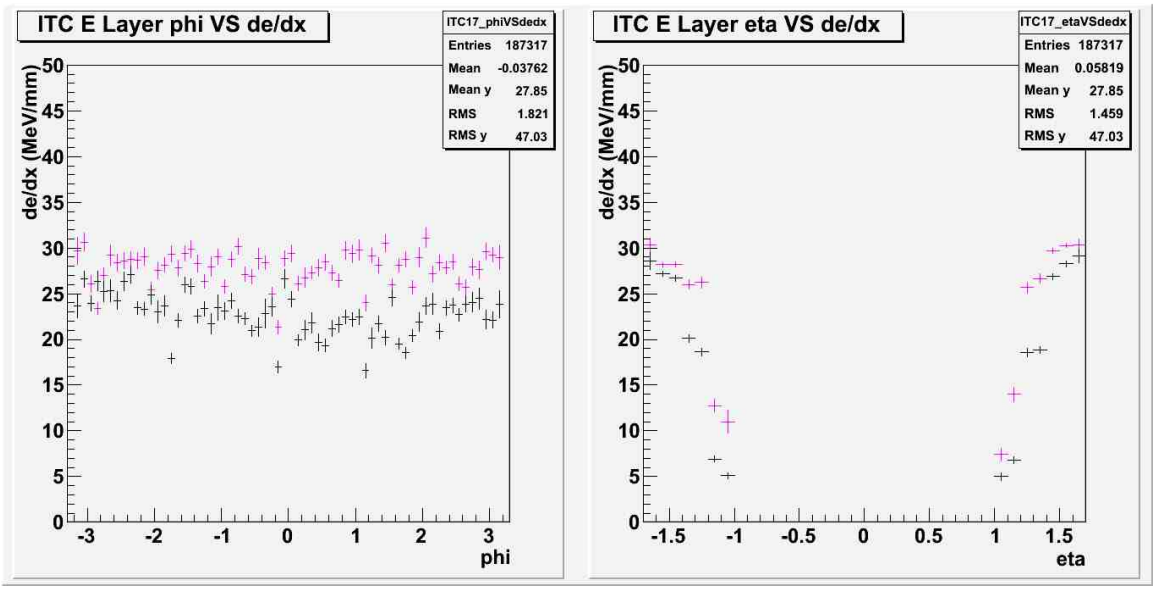

Figure 5.6. Response for ITC Layer E in ϕ (left) and η (right).

When looking at the individual towers, low statistics comes into play, and is consequently considered. Table 5.2 summarizes the average response for each tower in the ITC. See Appendix B for the corresponding graphs.

Table 5.2. Average ϕ Response (MeV/mm) for E Layer towers

Layer	A-Side	C-Side
C10	3.343	3.283
D4	3.078	2.190
E1	2.651	2.779
E2	3.153	3.281
E3	7.270	7.107
E4	10.93	10.94

The crack tiles (E3 and E4) have much higher responses compared to E1 and E2, which may indicate the calibration of these cells is not yet adequate. The response of the C10 cells is actually closer to 2.9 MeV/mm; the irregular responses for the stated regions greatly increases the average.

5.3 Photoelectron Production in C10 Cells

With the yield values obtained via fitting the muon energy distributions in C10 cells to a normalized Landau curve, many cells are seen to have a good yield, with a few exceptions. Only three cells in the C-side (module numbers 2, 21, and 22) were found to have a bad yield as compared to the other cells, while the A-side only had two bad cells (module numbers 13 and 21). These cells with too few statistics to apply an accurate fit, four cells on A-side (module numbers 7, 17, 20, and 29) and three on C-side (module numbers 12, 13, and 37), are set to yield = 0 for further analysis. Figure 5.7 shows the module number vs. the yield for each side, and the actual yield values are given in Tables D.1 and D.2 in Appendix D.

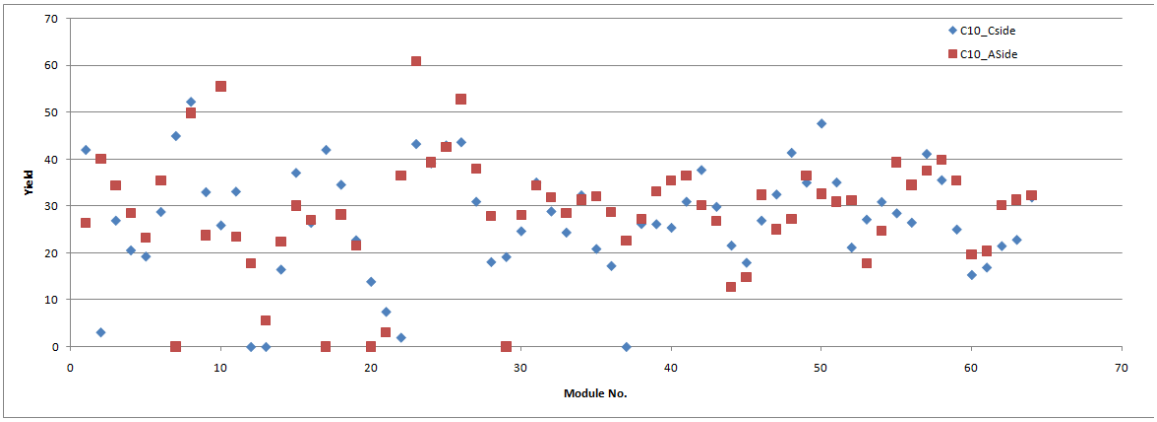

Figure 5.7. Photoelectron yield for C10 cells.

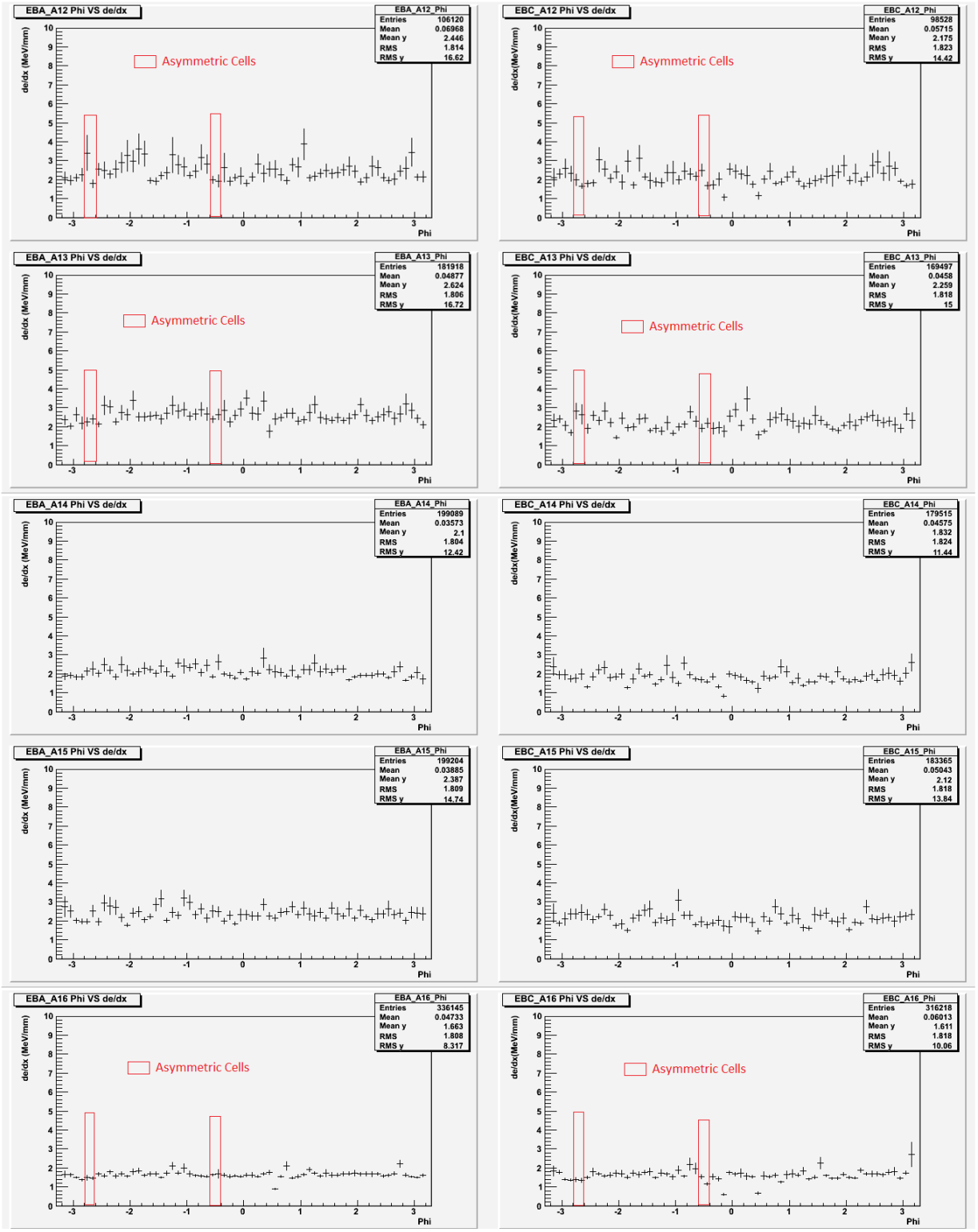

Figure 5.8. Response in ϕ for End Barrel Layer A Cells and Towers.

CHAPTER 6

CONCLUSIONS

This study has verified the average uniform response of approximately 1.575 MeV/mm of the cells within the layers of the Long Barrel and End Barrel sections of the Tile Calorimeter of the ATLAS detector in η and ϕ using muons produced from $\sqrt{s} = 7$ TeV pp collisions at the LHC. The special asymmetric cells within the End Barrel A Layer of the Tile Calorimeter have been verified to have a response similar to other cells within the layer and within other layers. The Intermediate Tile Calorimeter layers have a much higher response than the end-cap and barrel layers, and it has been found that cells in the C10 layer have a non-uniform response that must be investigated further.

Errors in the path length algorithm have been identified for the end-cap and long barrel cells bordering the gap-region of the detector, as well as the D4 cells of the ITC. The track match criteria used in this analysis can be improved to reduce the pedestal further so that pedestal cuts would not be as necessary. Several cells in the C10 layer of the ITC have very low yield for photoelectron production, which also warrants further investigation.

APPENDIX A

ADDITIONAL PLOTS: LONG BARREL

In this appendix, all necessary plots and figures are provided for the Long Barrel (LB) section of the ATLAS Tile Calorimeter. In the response plots for the various layers, the collision results are in black, and the Monte Carlo results are in magenta. The plots are arragned in groups according to each layer.

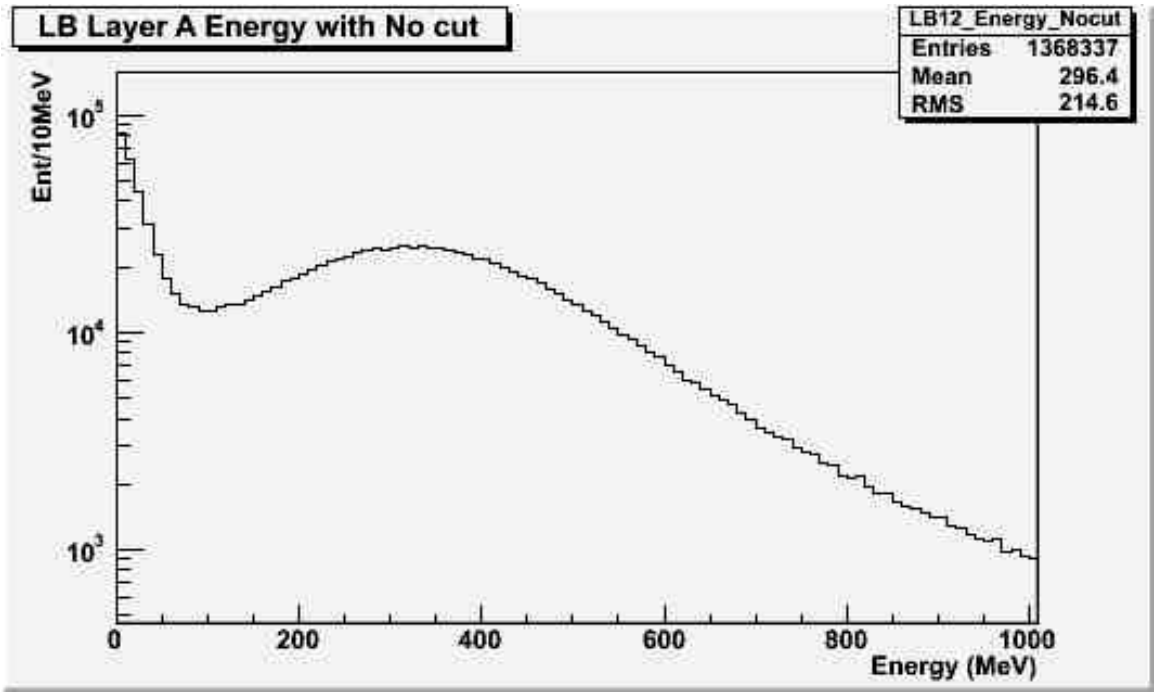

Figure A.1. Uncut Energy Distribution in LB A.

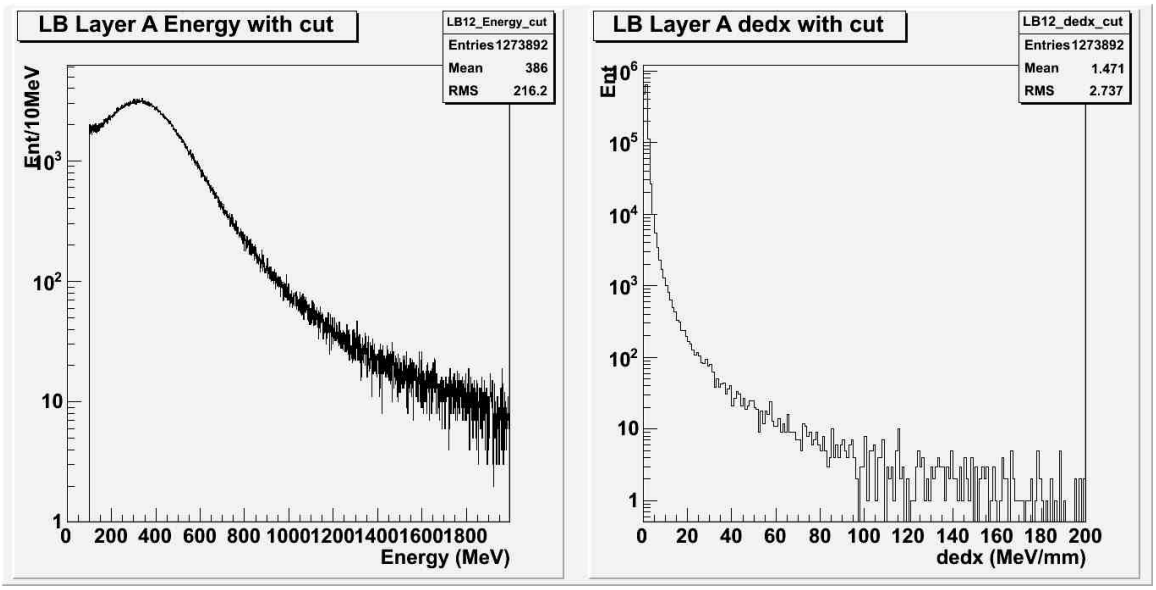

Figure A.2. Energy (left) and dE/dx (right) Distributions after Selection for LB A.

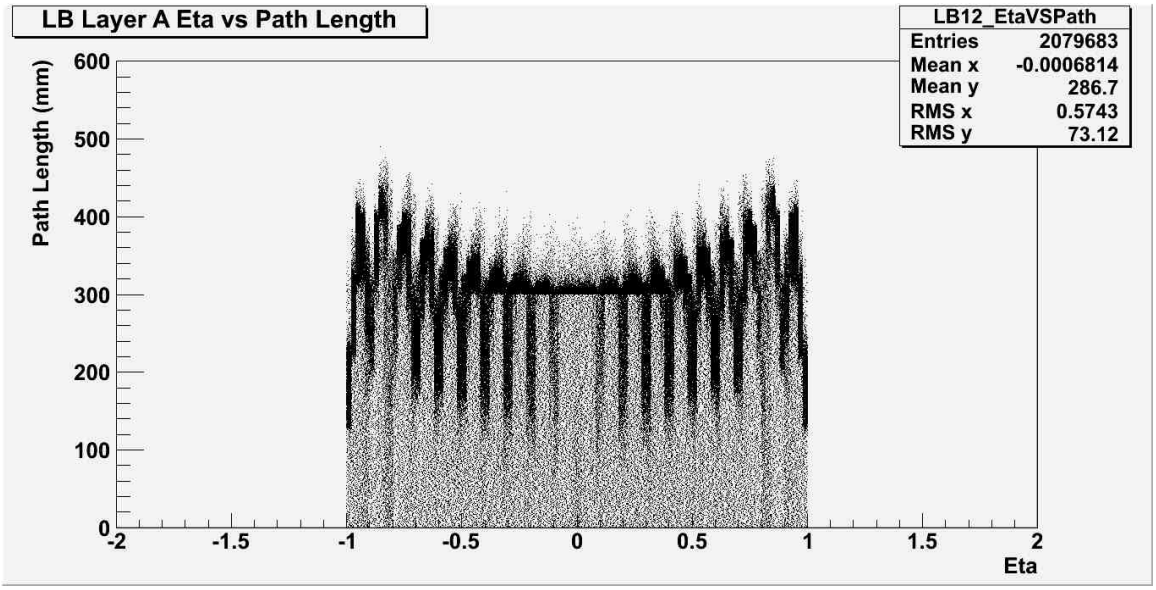

Figure A.3. η vs. Path Length in LB A.

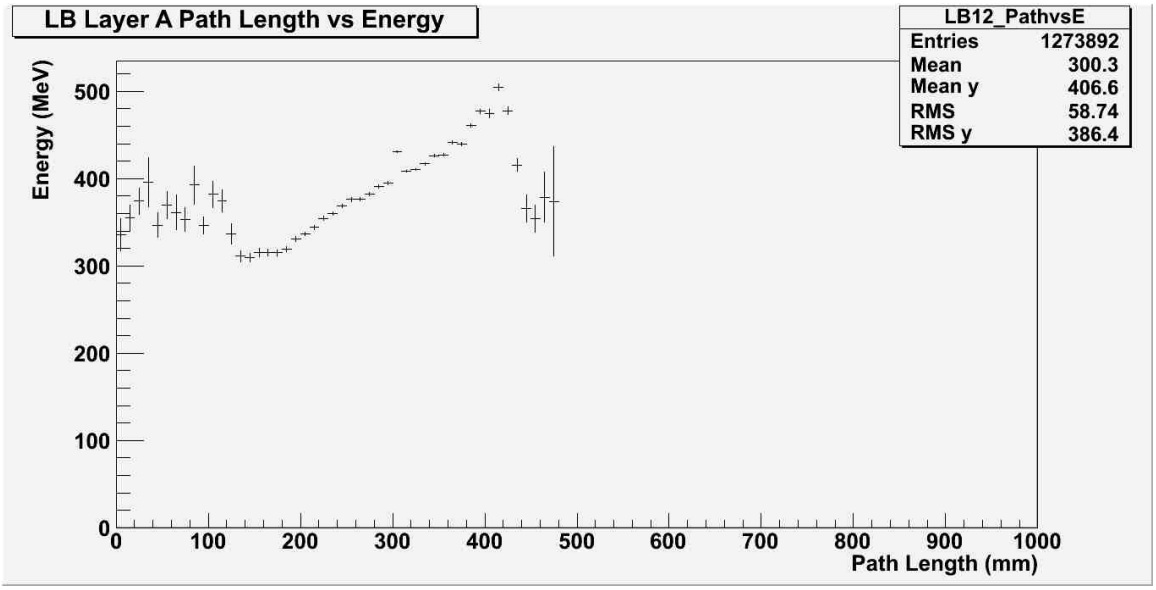

Figure A.4. Path Length vs. Energy in LB A.

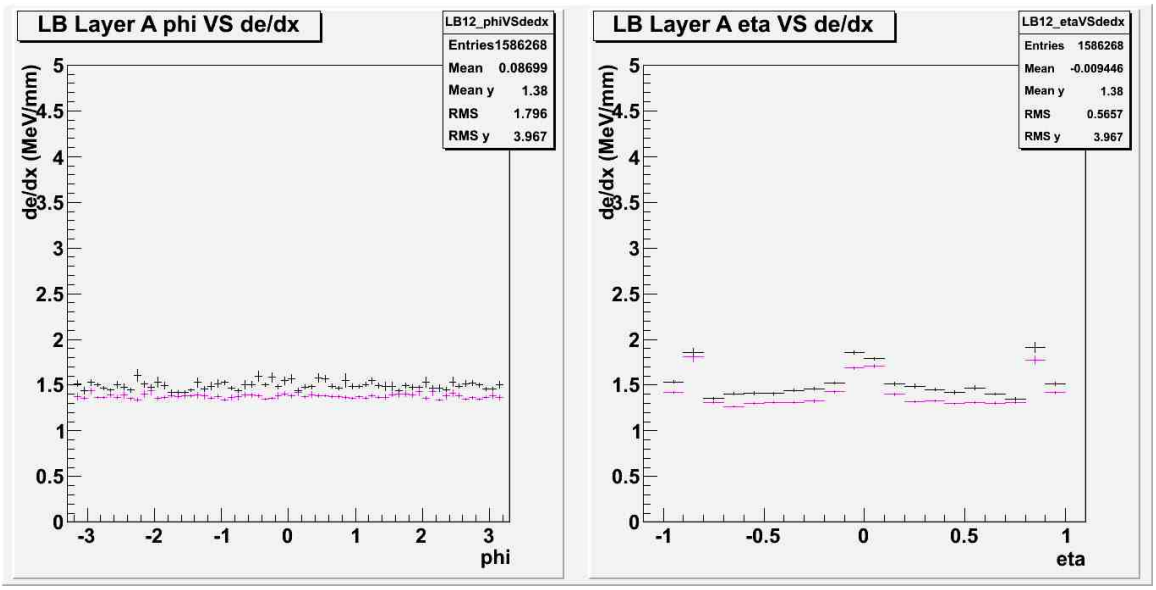

Figure A.5. Response for LB Layer A in ϕ (left) and η (right).

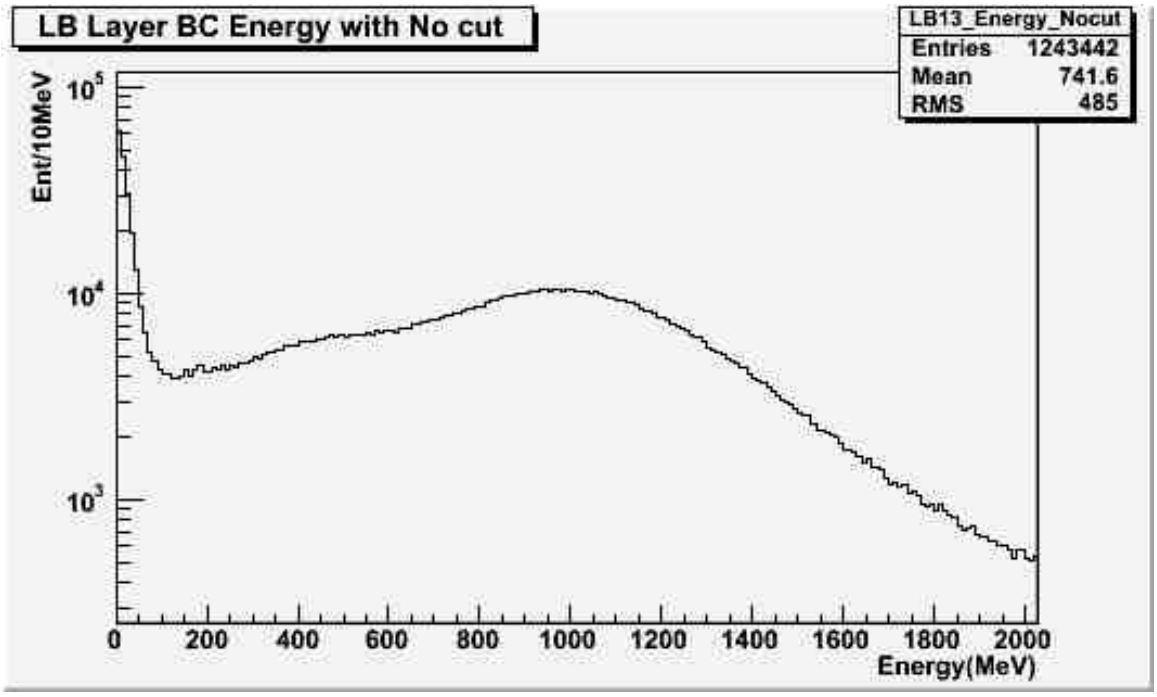

Figure A.6. Uncut Energy Distribution in LB BC.

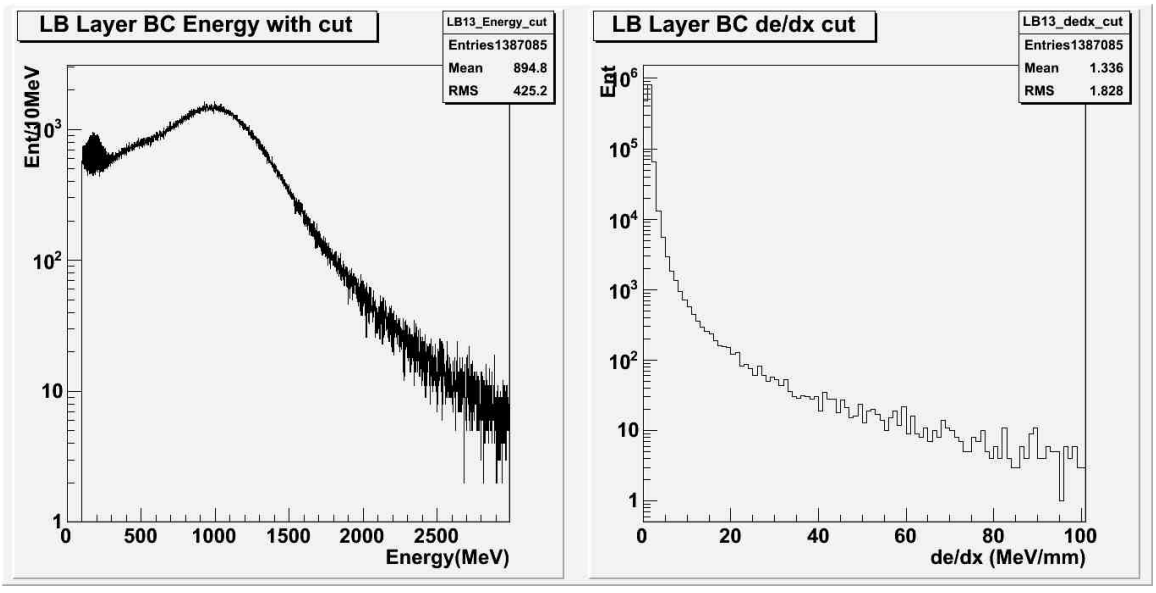

Figure A.7. Energy (left) and dE/dx (right) Distributions after Selection for LB BC.

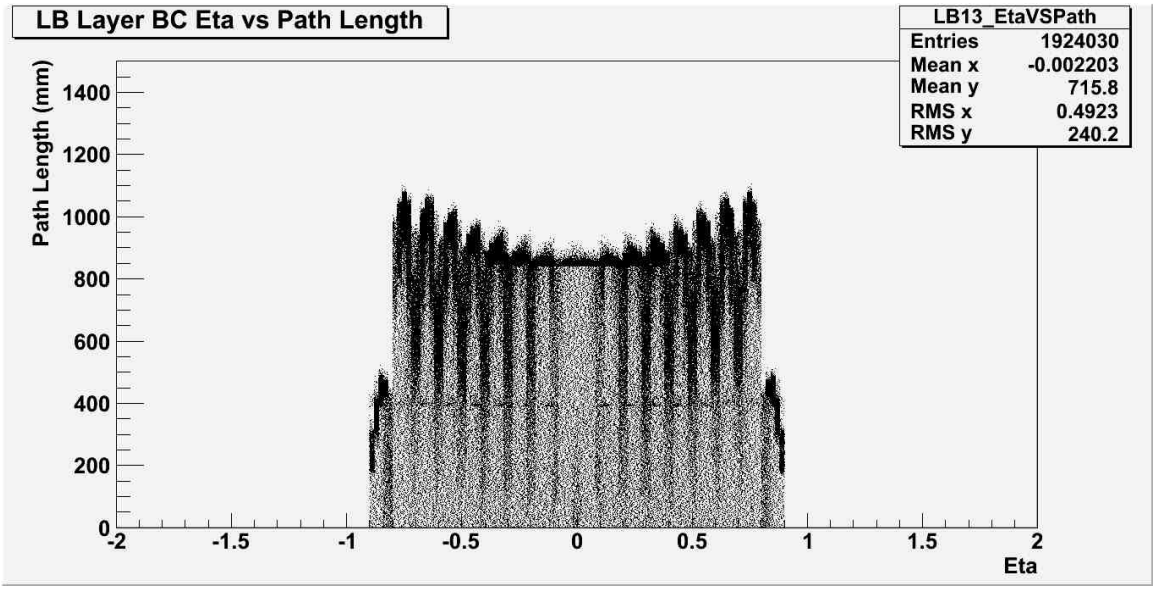

Figure A.8. η vs. Path Length in LB BC.

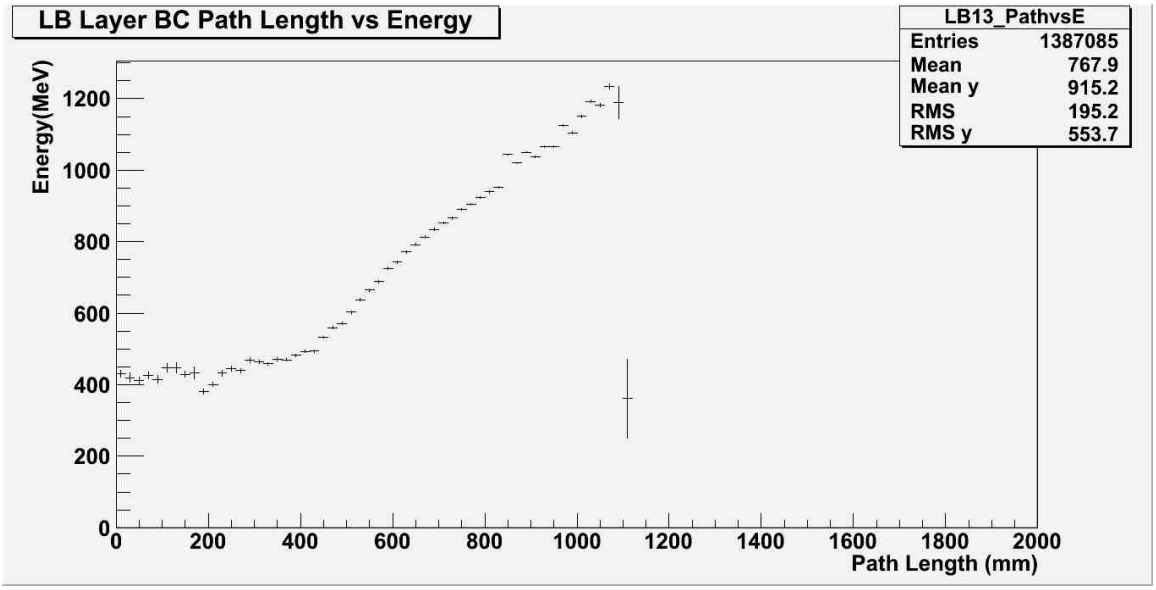

Figure A.9. Path Length vs. Energy in LB BC.

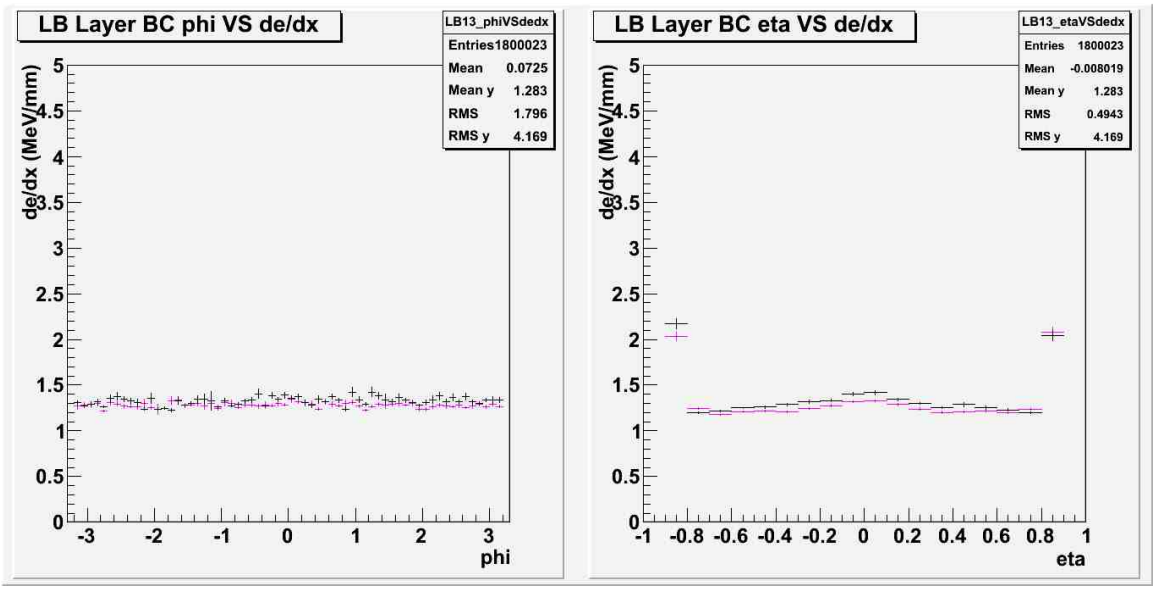

Figure A.10. Response for LB Layer BC in ϕ (left) and η (right).

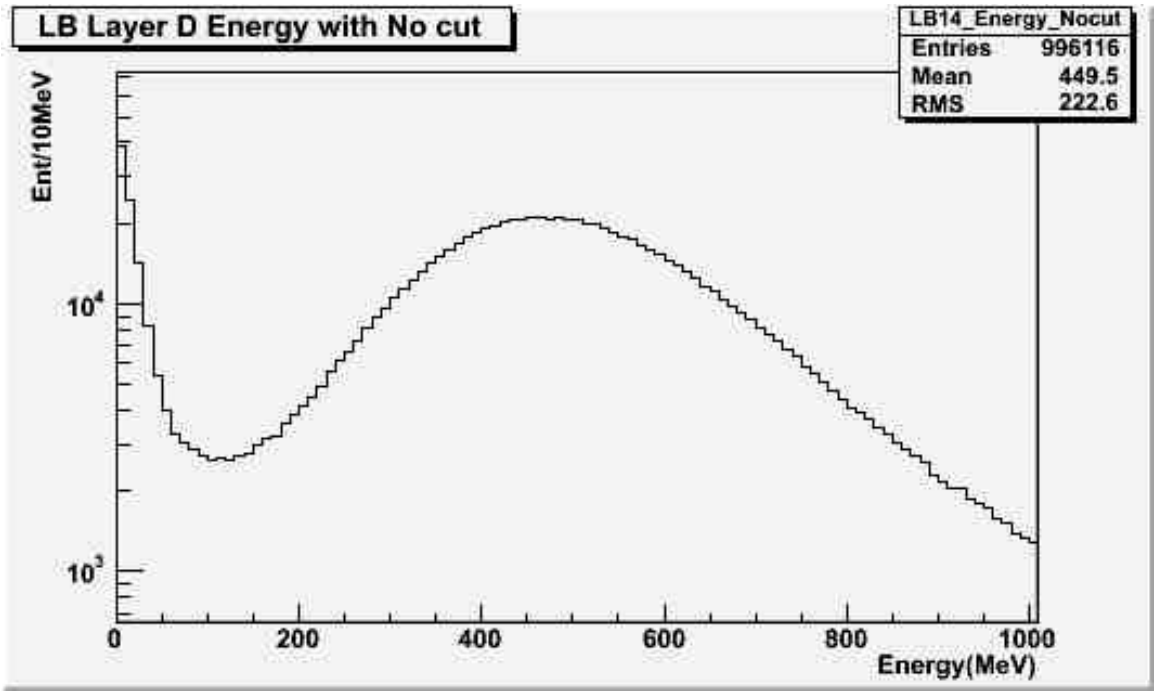

Figure A.11. Uncut Energy Distribution in LB D.

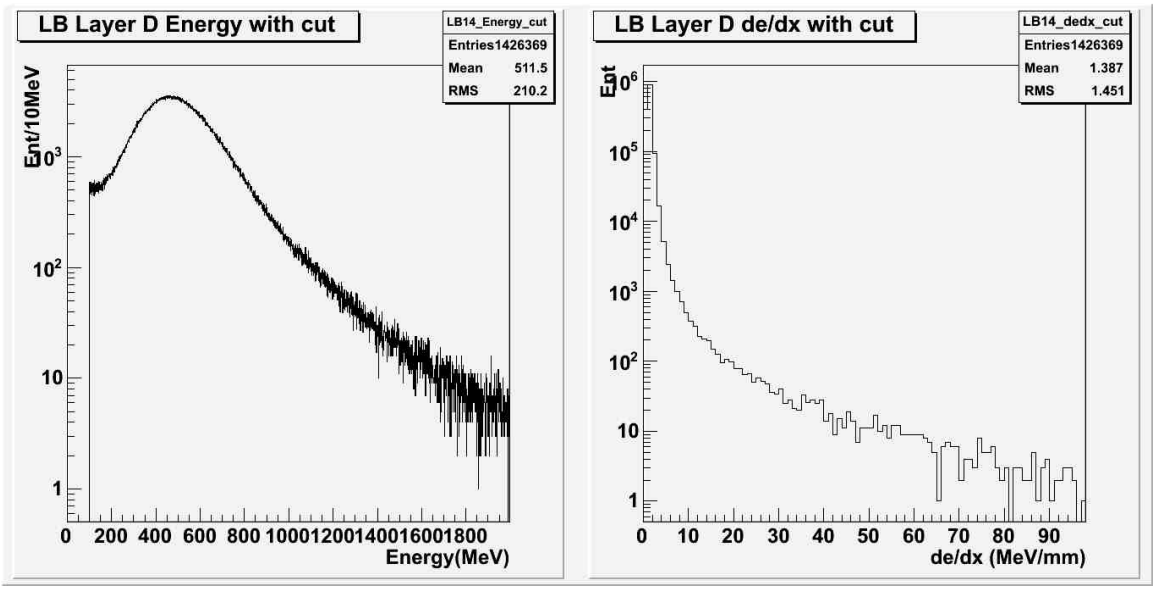

Figure A.12. Energy (left) and dE/dx (right) Distributions after Selection for LB D.

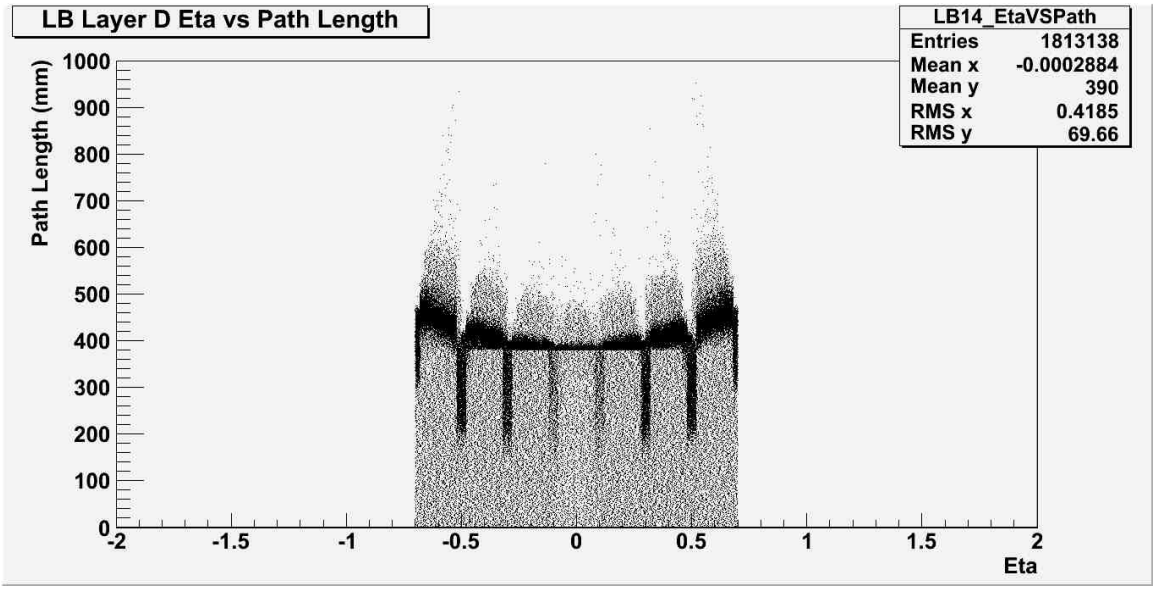

Figure A.13. η vs. Path Length in LB D.

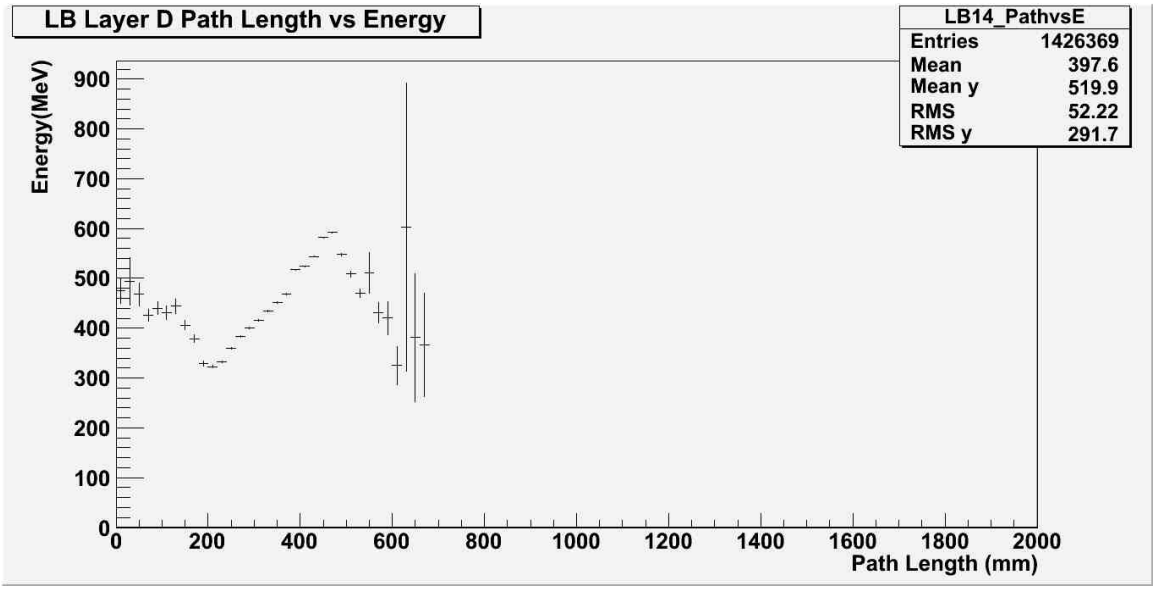

Figure A.14. Path Length vs. Energy in LB D.

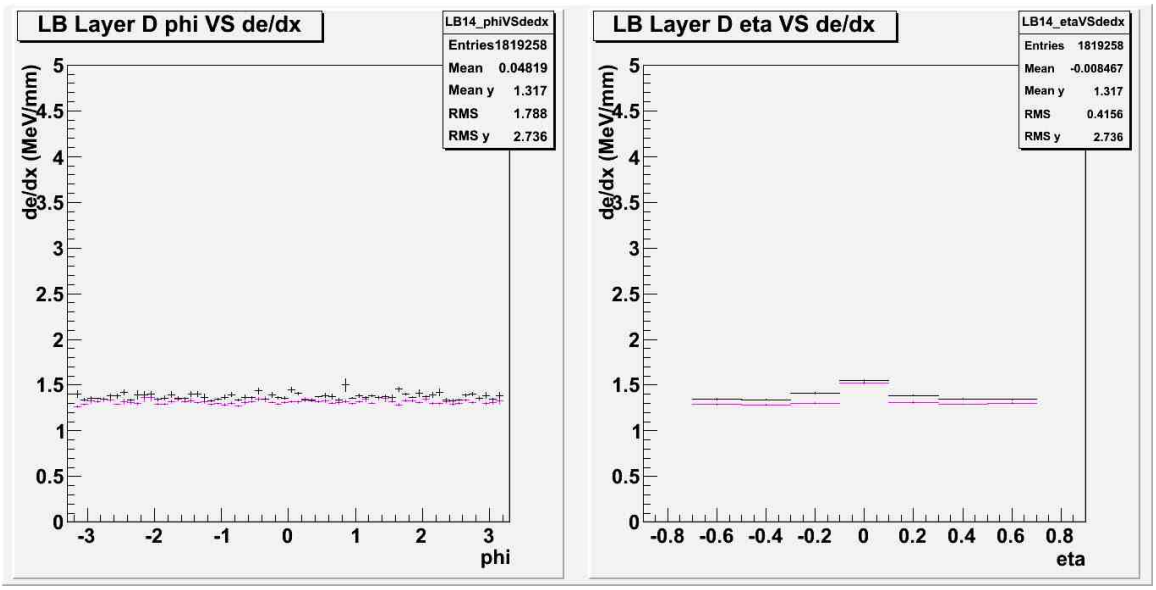

Figure A.15. Response for LB Layer D in ϕ (left) and η (right).

APPENDIX B

ADDITIONAL PLOTS: ITC

In this appendix, all necessary plots and figures are provided for the Intermediate Tile Calorimeter (ITC) section of the ATLAS Tile Calorimeter. In the response plots for the various layers, the collision results are in black, and the Monte Carlo results are in magenta. The plots are arragned in groups according to each layer.

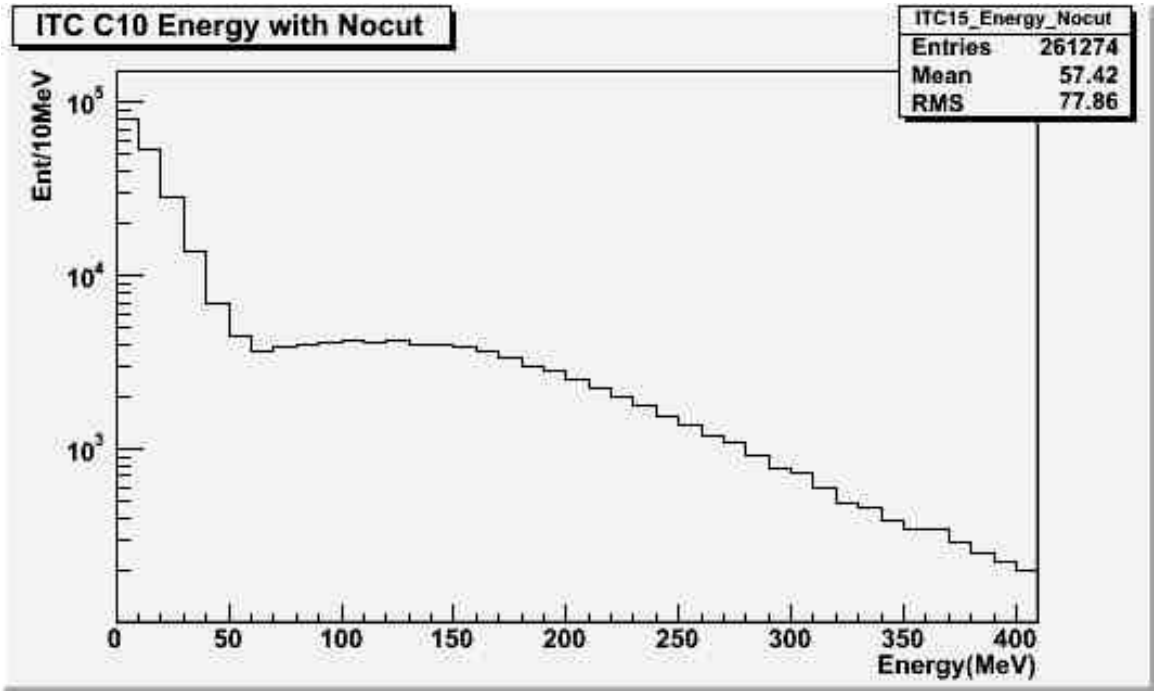

Figure B.1. Uncut Energy Distribution in ITC C10.

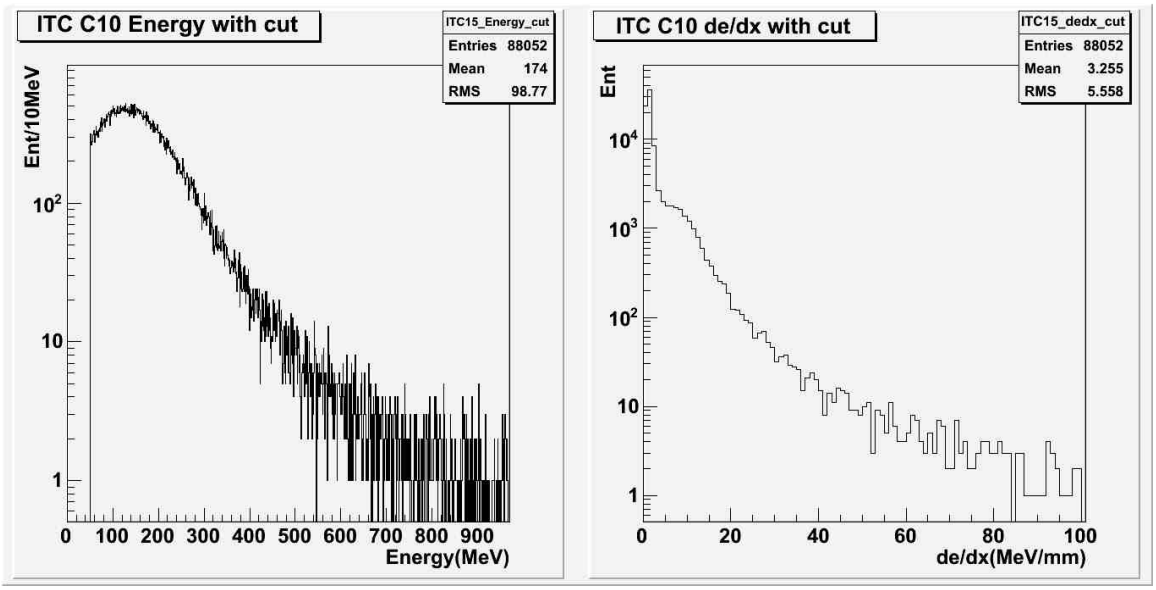

Figure B.2. Energy (left) and dE/dx (right) Distributions after Selection for ITC C10.

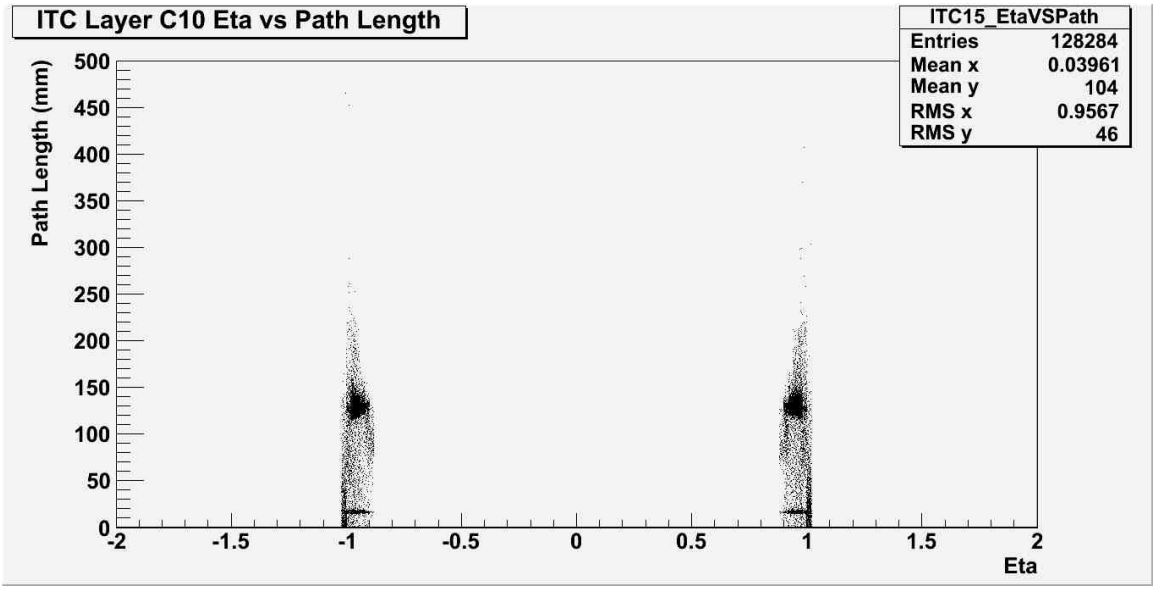

Figure B.3. η vs. Path Length in ITC C10.

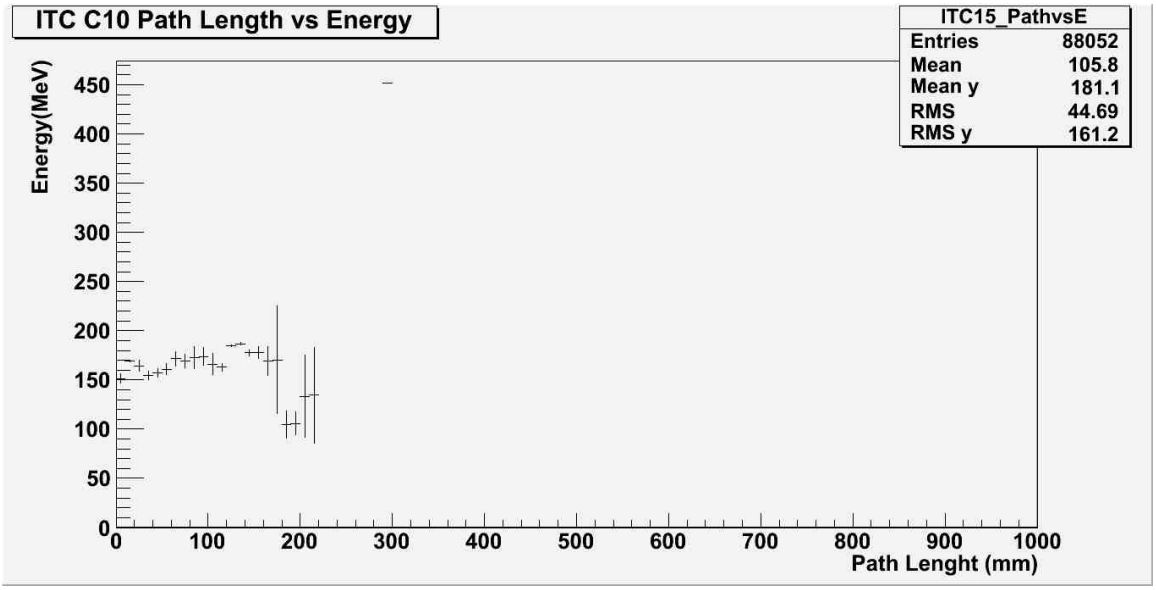

Figure B.4. Path Length vs. Energy in ITC C10.

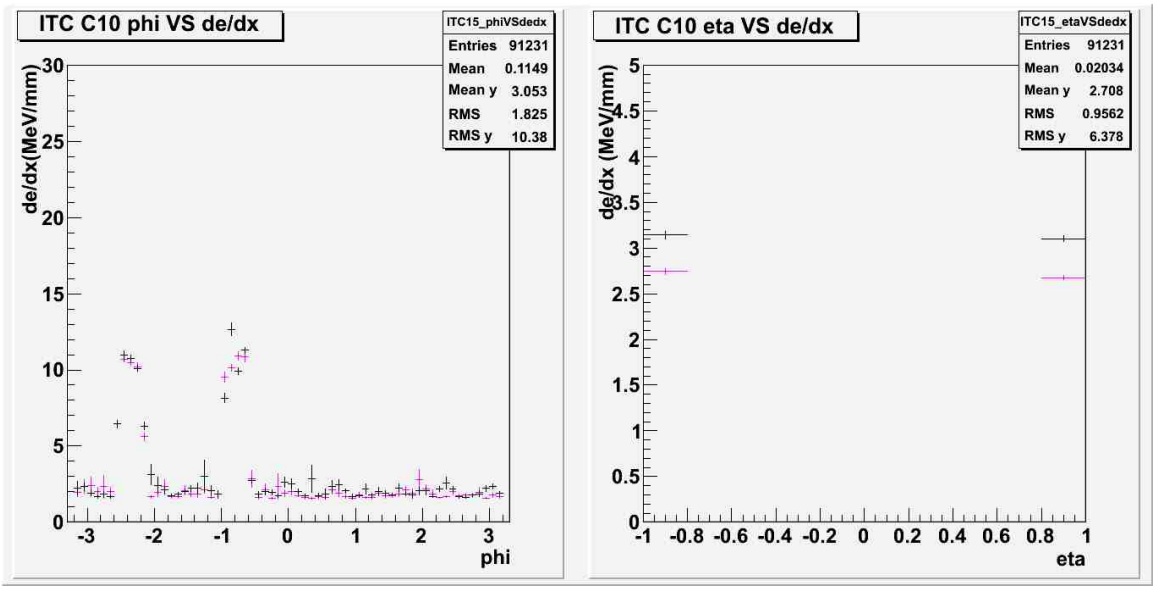

Figure B.5. Response for ITC Layer C10 in ϕ (left) and η (right).

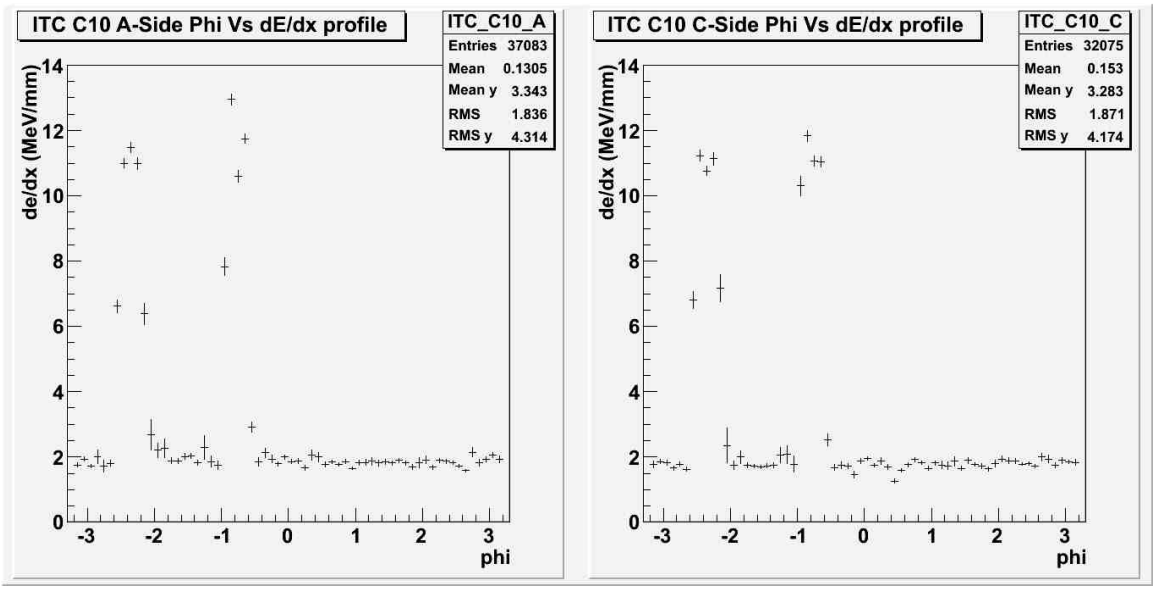

Figure B.6. Response in ϕ for ITC C10 A-Side (left) and C-Side (right).

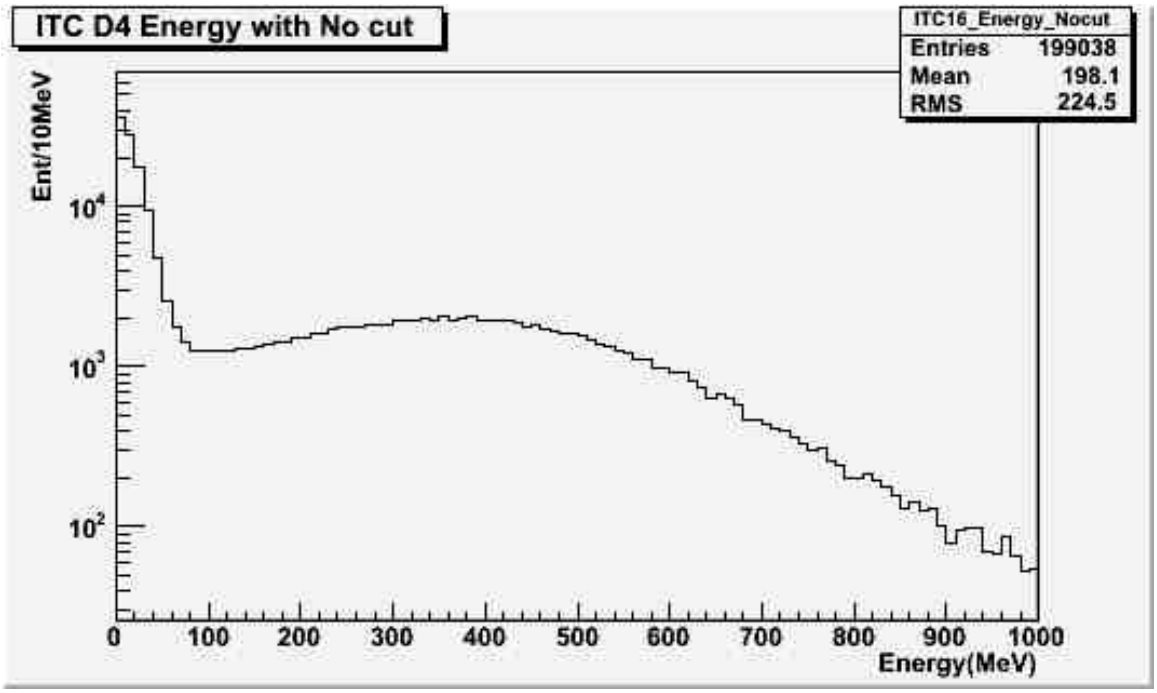

Figure B.7. Uncut Energy Distribution in ITC D4.

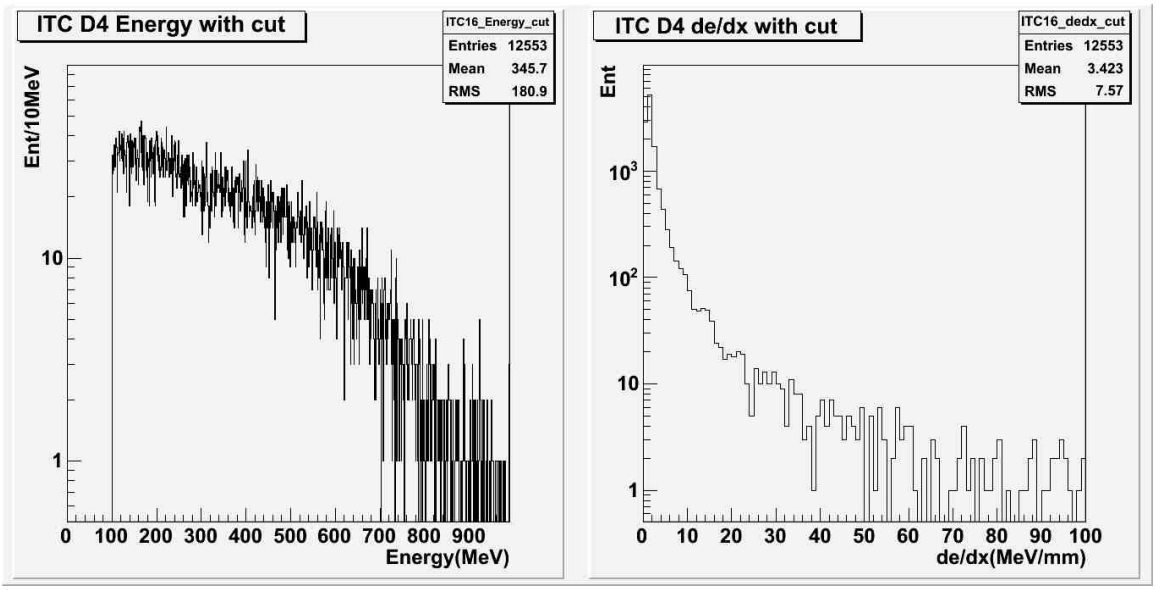

Figure B.8. Energy (left) and dE/dx (right) Distributions after Selection for ITC D4.

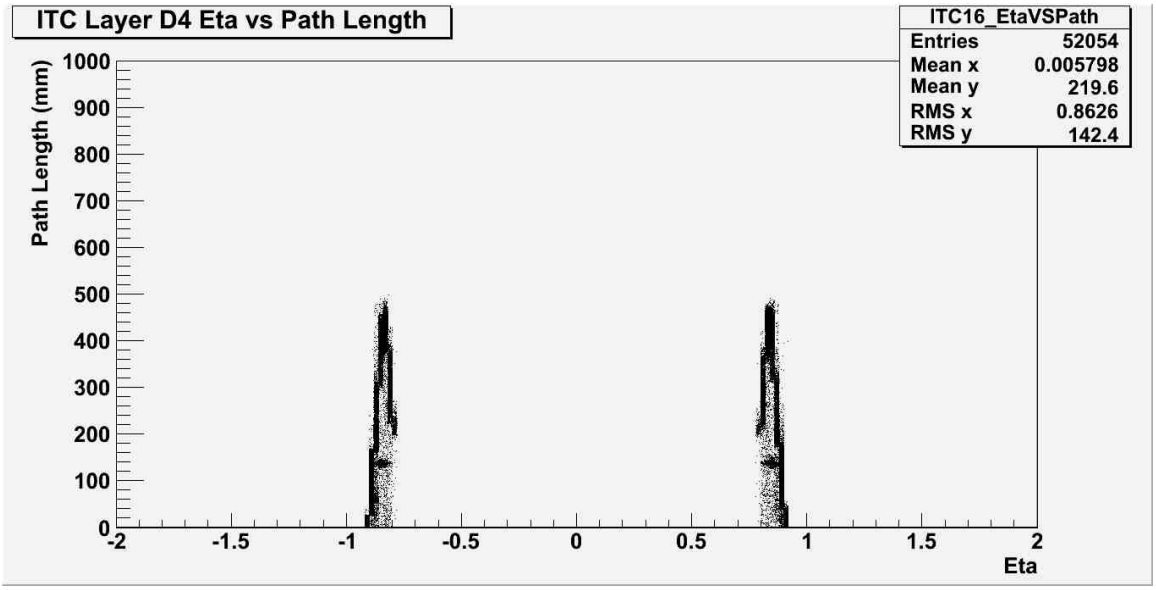

Figure B.9. η vs. Path Length in ITC D4.

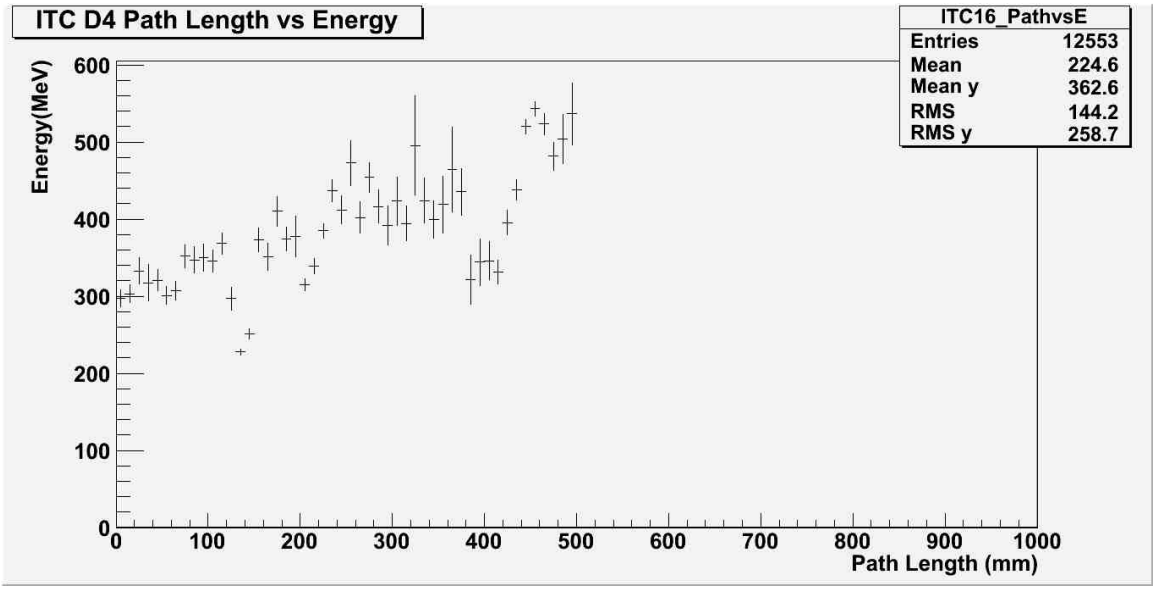

Figure B.10. Path Length vs. Energy in ITC D4.

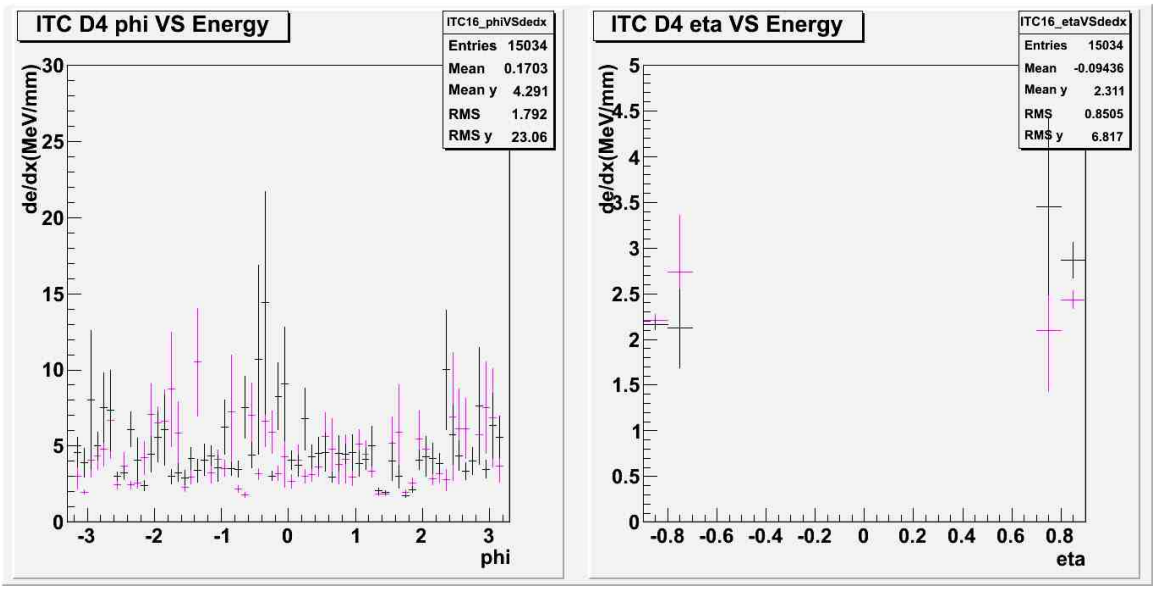

Figure B.11. Response for ITC Layer D4 in ϕ (left) and η (right).

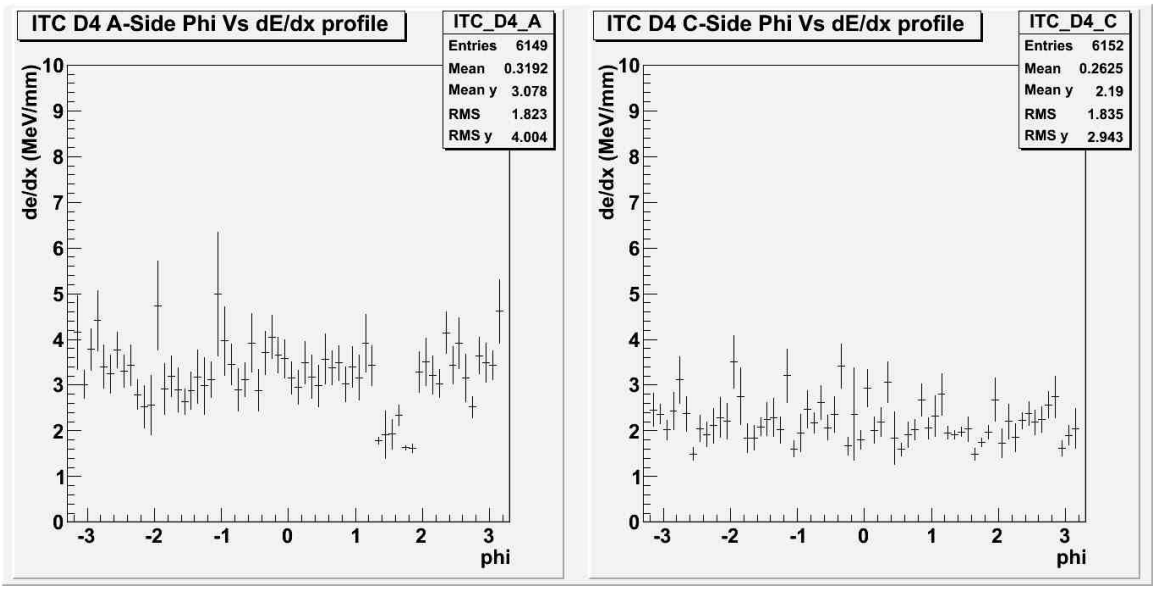

Figure B.12. Response in ϕ for ITC D4 A-Side (left) and C-Side (right).

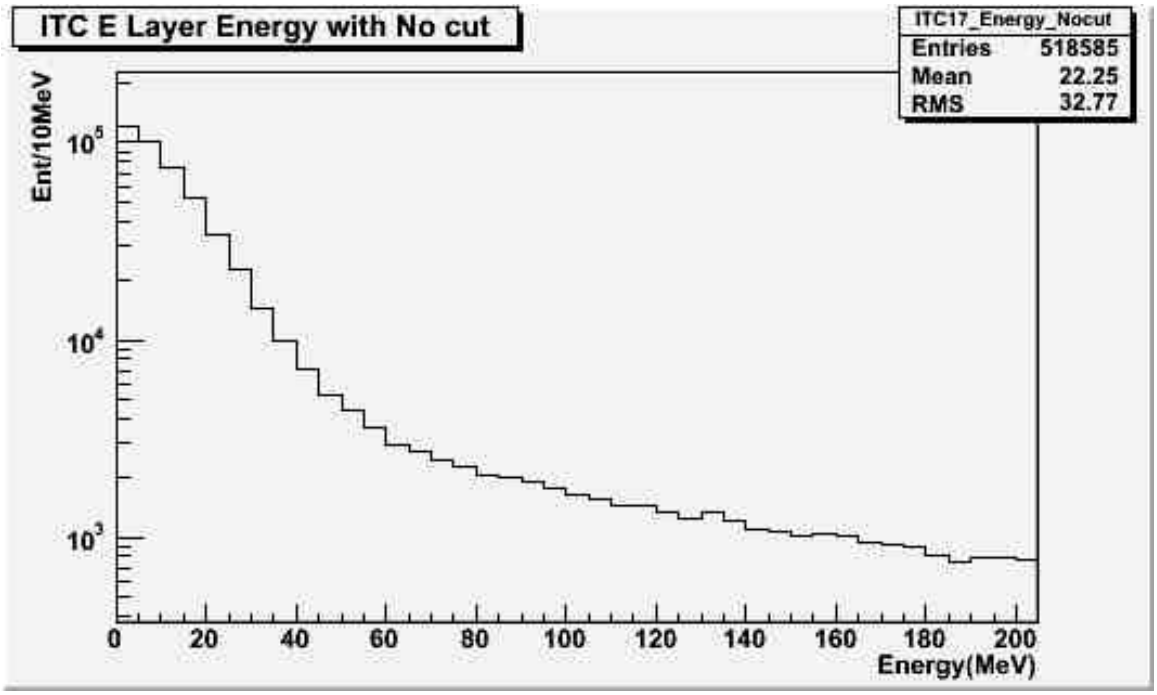

Figure B.13. Uncut Energy Distribution in ITC E.

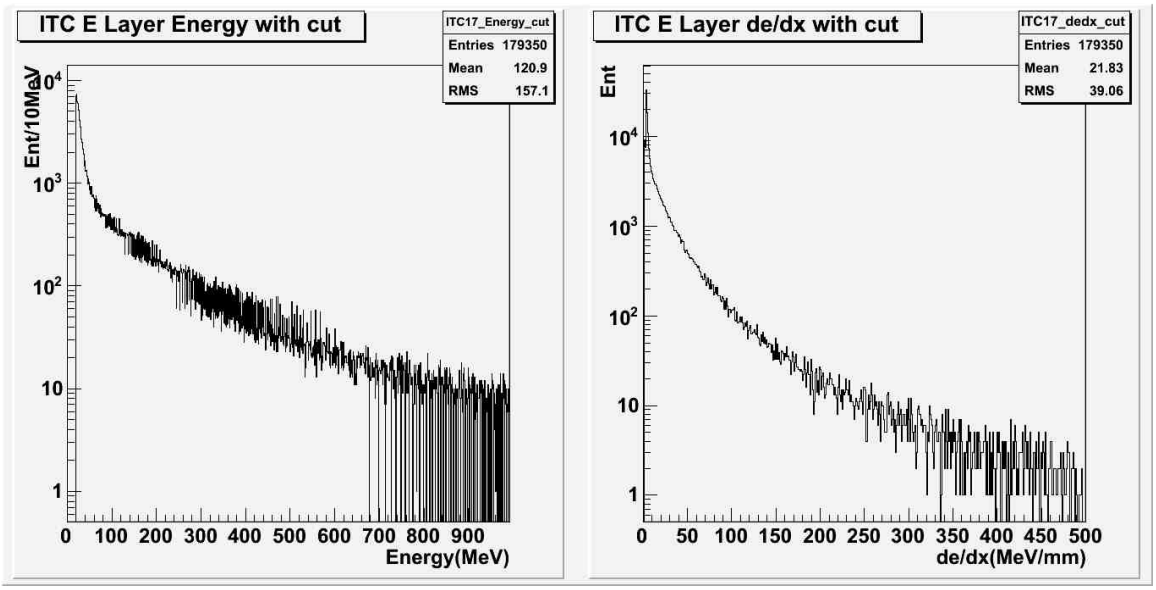

Figure B.14. Energy (left) and dE/dx (right) Distributions after Selection for ITC E.

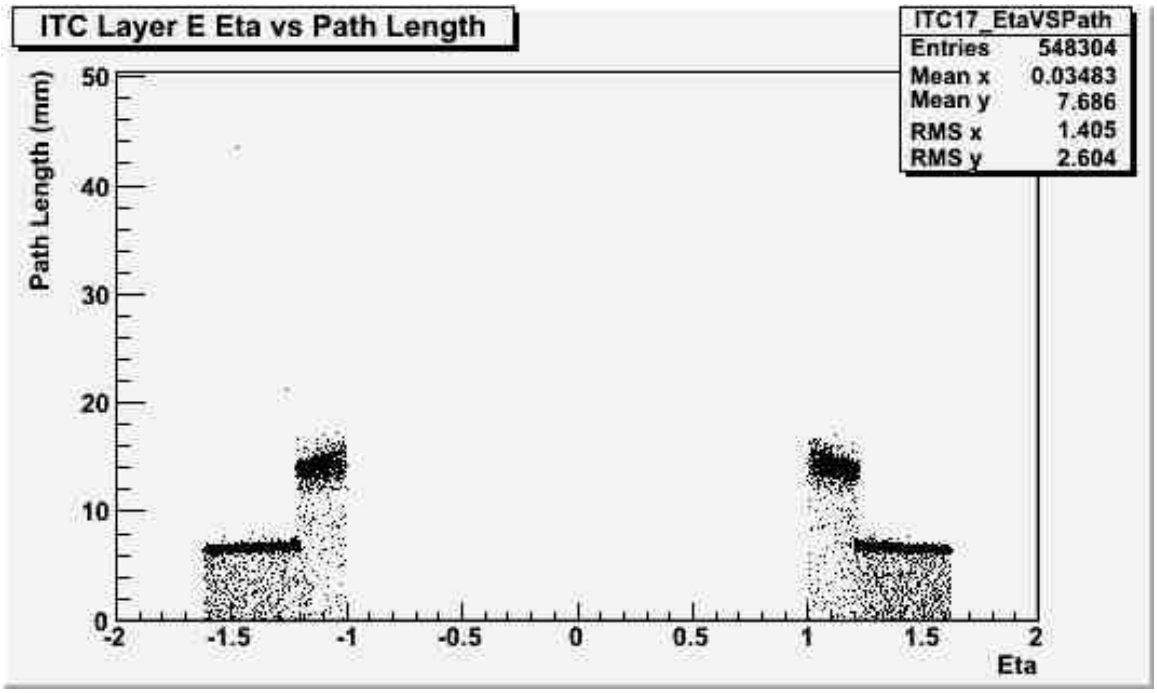

Figure B.15. η vs. Path Length in ITC E.

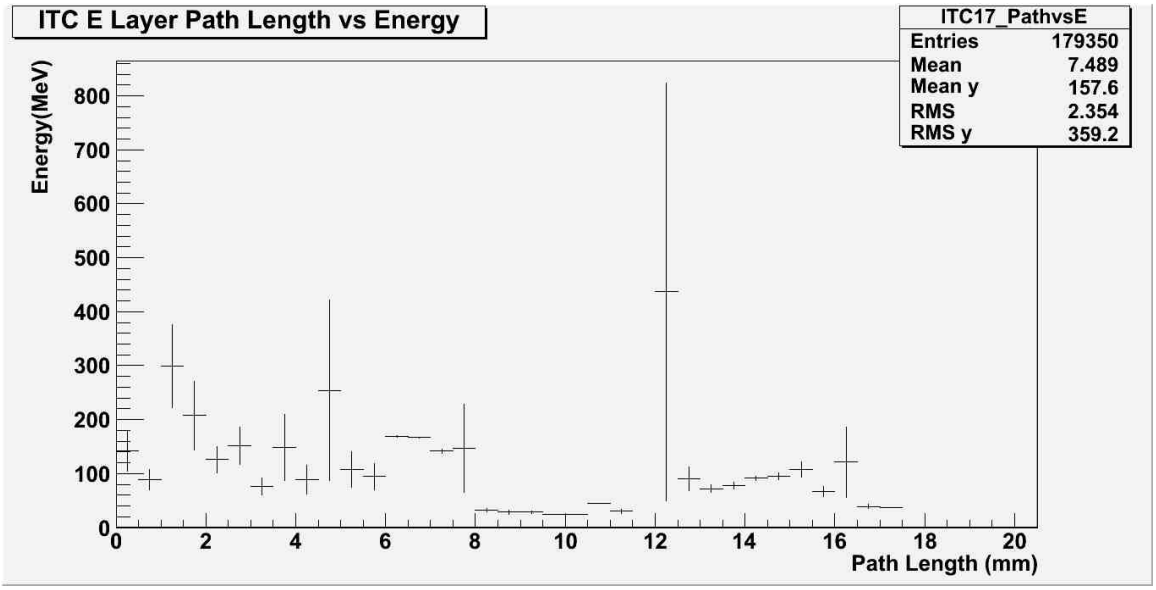

Figure B.16. Path Length vs. Energy in ITC E.

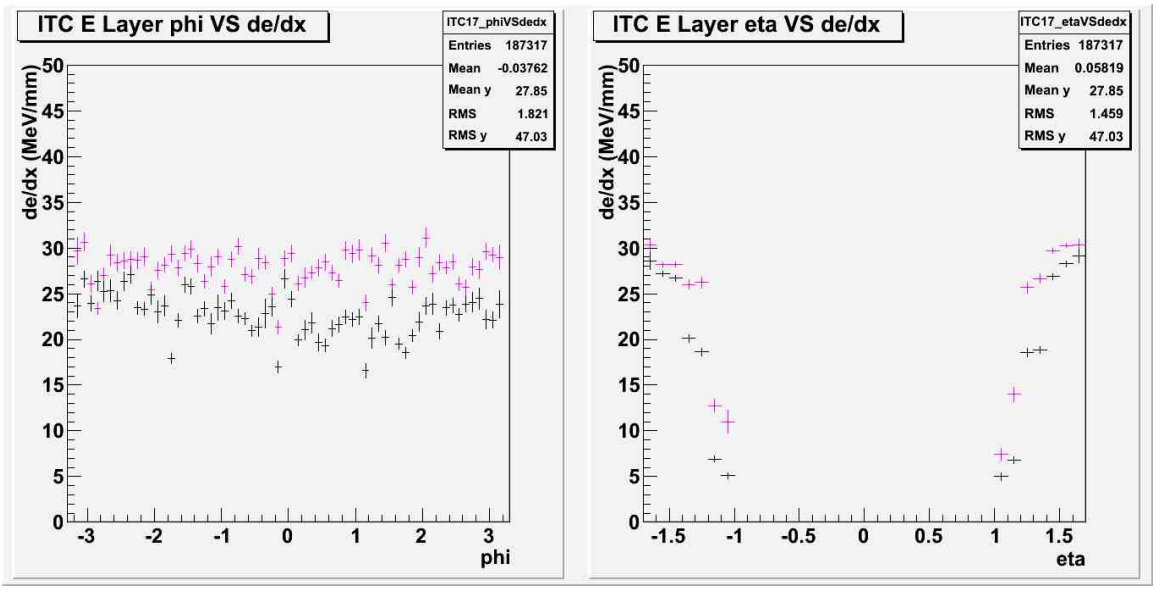

Figure B.17. Response for ITC Layer E in ϕ (left) and η (right).

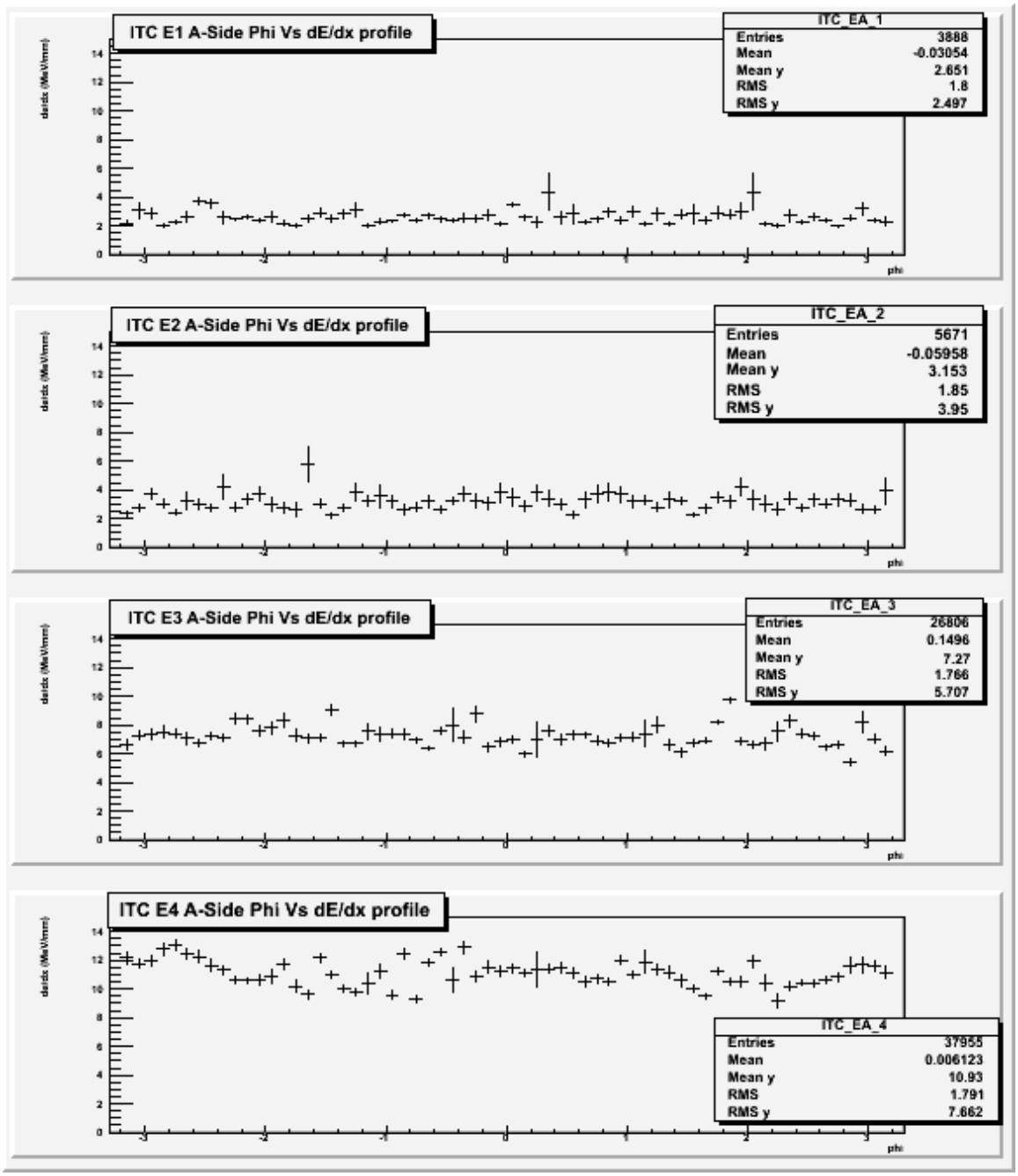

Figure B.18. Response in ϕ for ITC Cells for each A-Side Tower.

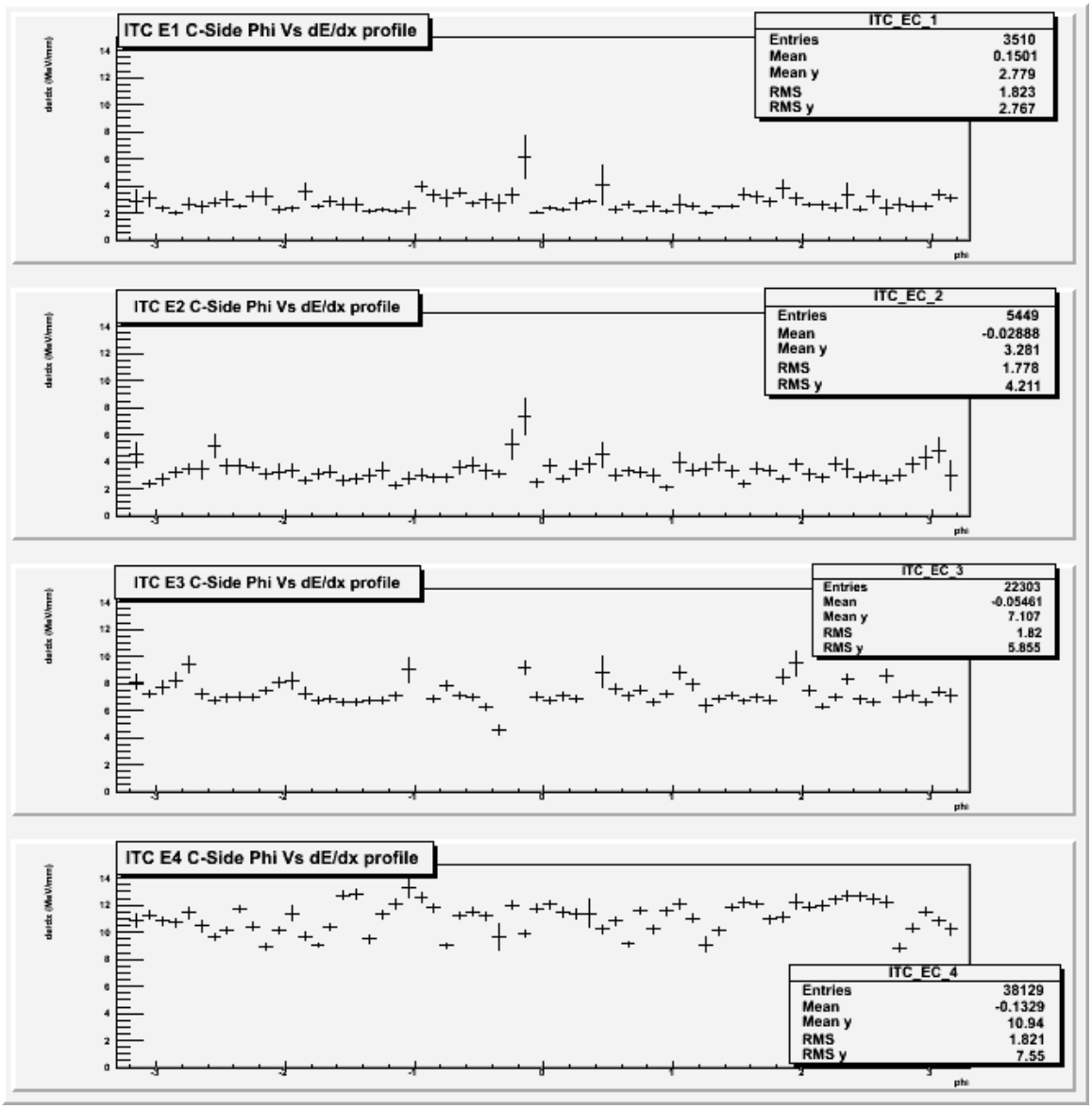

Figure B.19. Response in ϕ for ITC Cells for each C-Side Tower.

APPENDIX C

ADDITIONAL PLOTS: END BARRELS

In this appendix, all necessary plots and figures are provided for the End Barrel (EB) sections of the ATLAS Tile Calorimeter. In the response plots for the various layers, the collision results are in black, and the Monte Carlo results are in magenta. The plots are arragned in groups according to each layer.

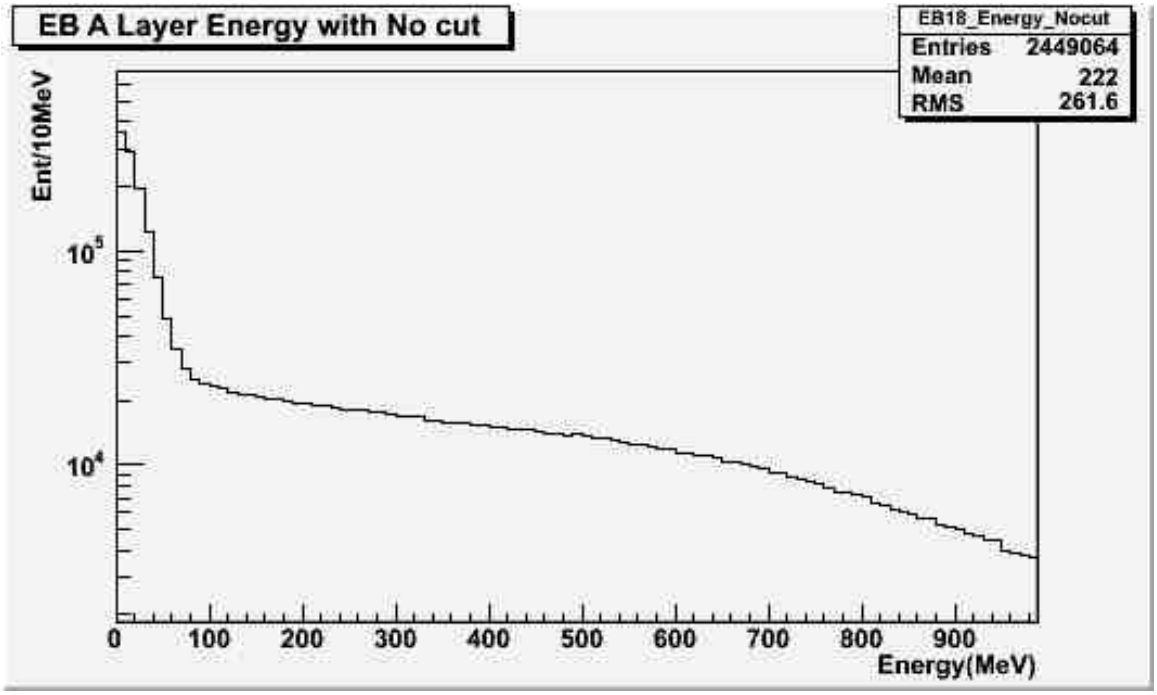

Figure C.1. Uncut Energy Distribution in EB A.

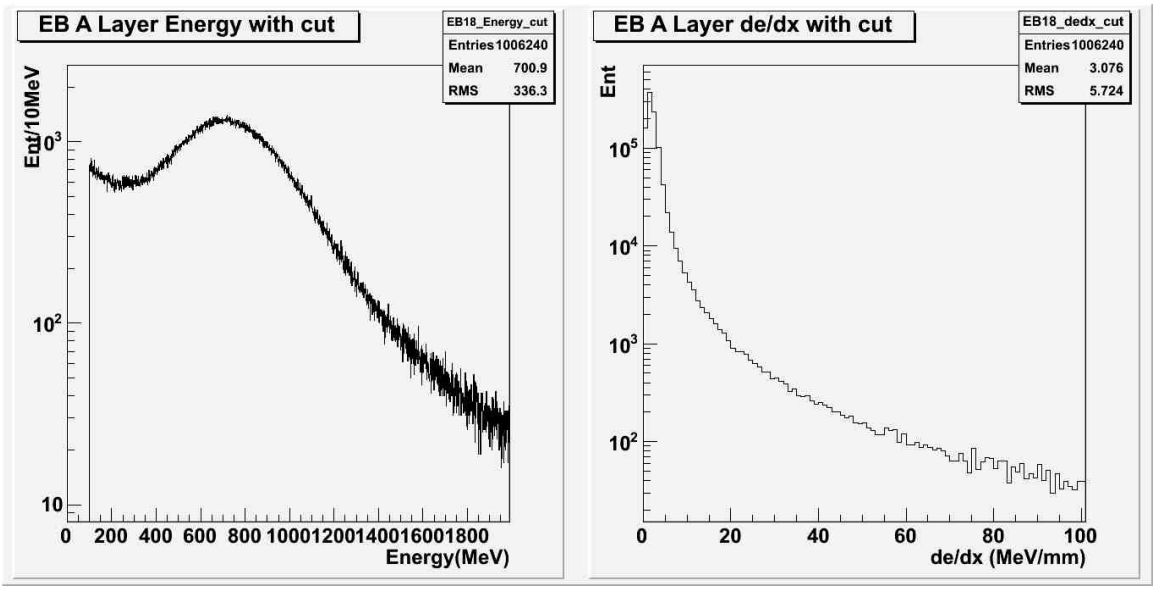

Figure C.2. Energy (left) and dE/dx (right) Distributions after Selection for EB A.

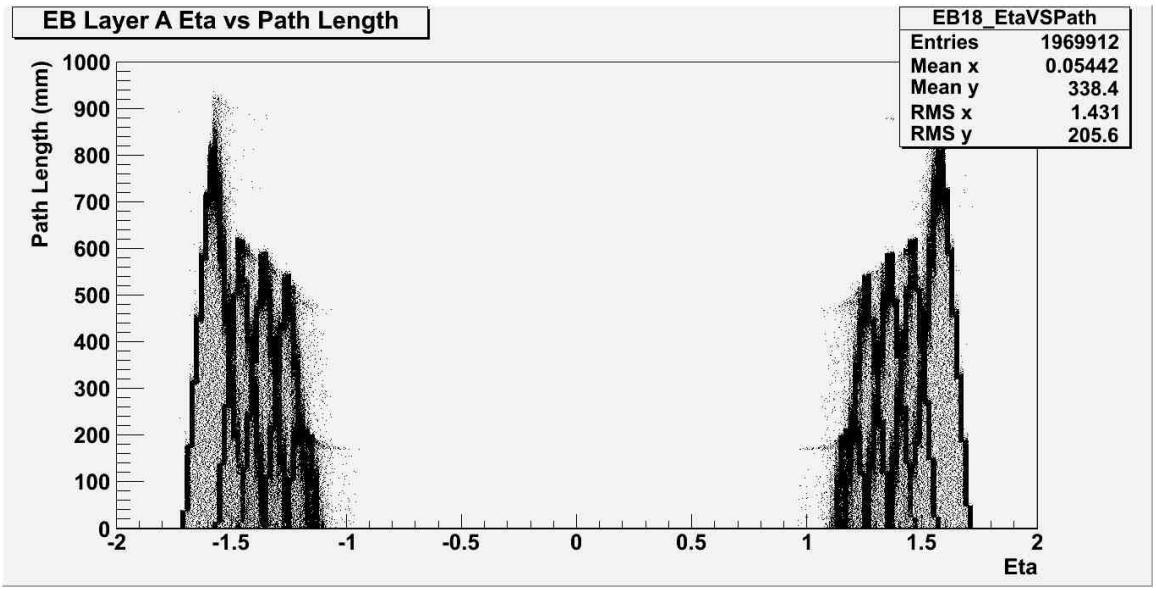

Figure C.3. η vs. Path Length in EB A.

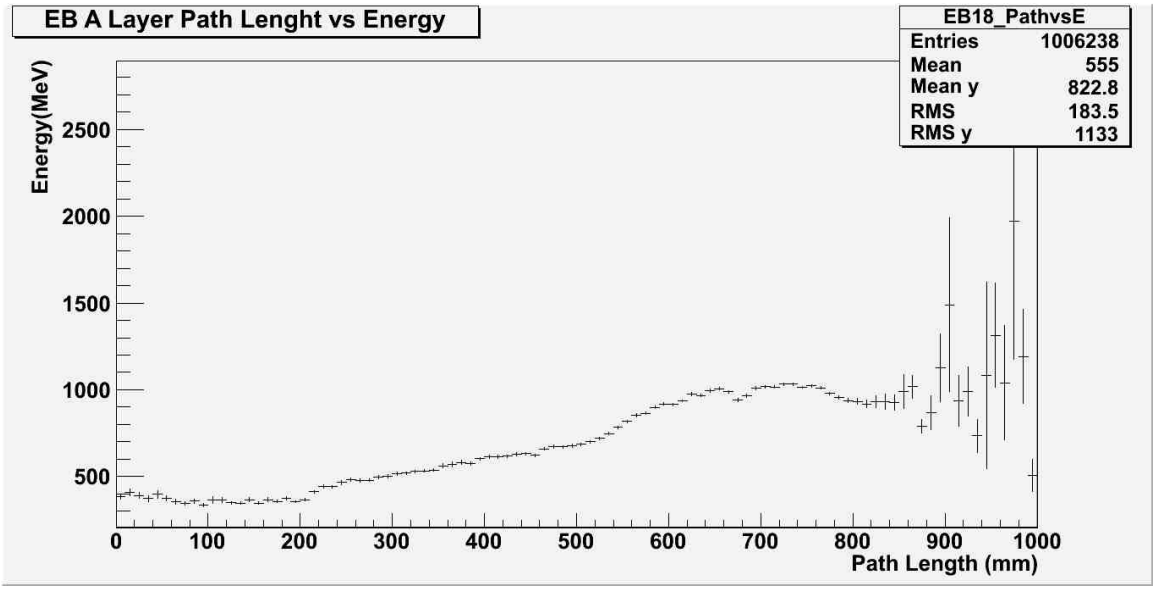

Figure C.4. Path Length vs. Energy in EB D.

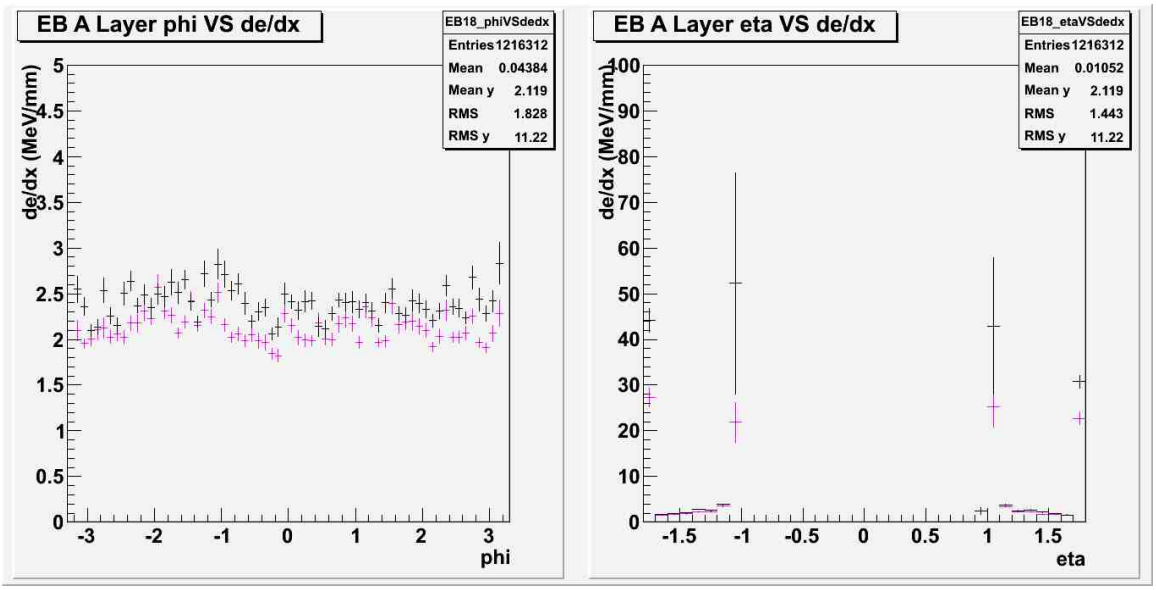

Figure C.5. Response for EB Layer D in ϕ (left) and η (right).

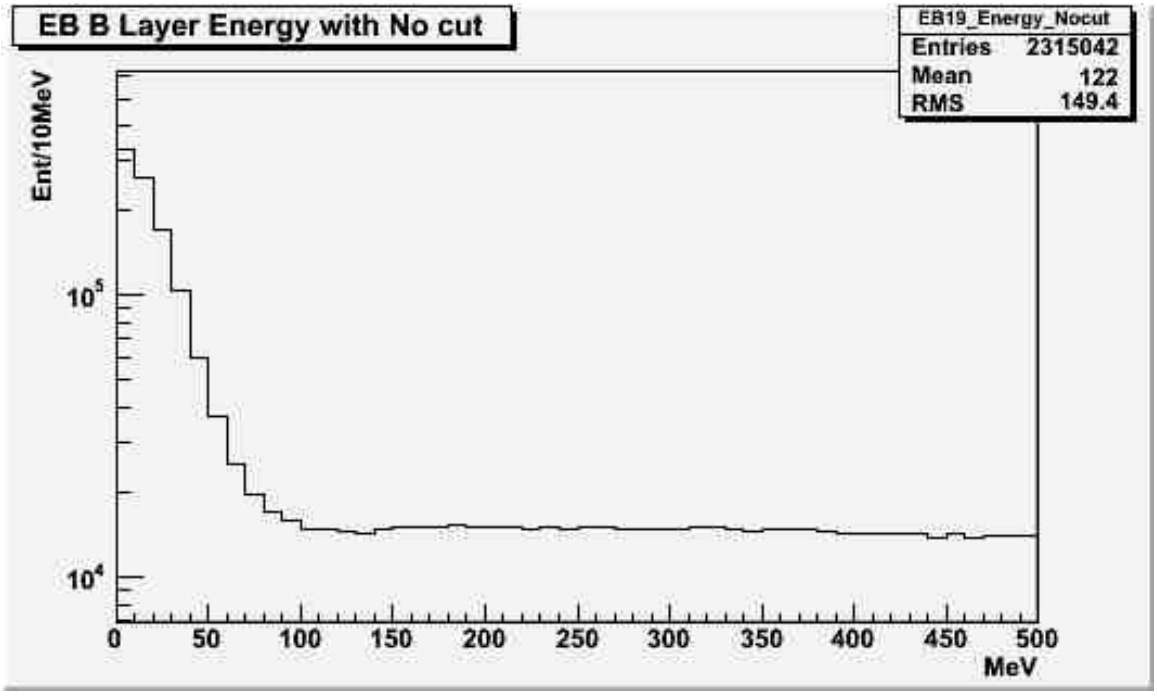

Figure C.6. Uncut Energy Distribution in EB B.

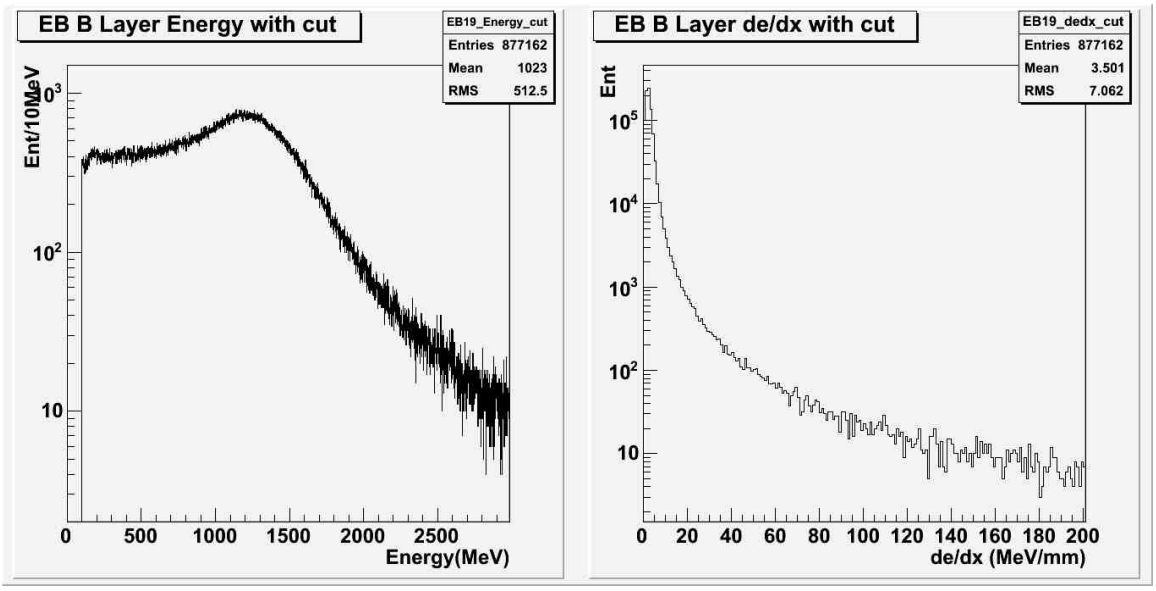

Figure C.7. Energy (left) and dE/dx (right) Distributions after Selection for EB B.

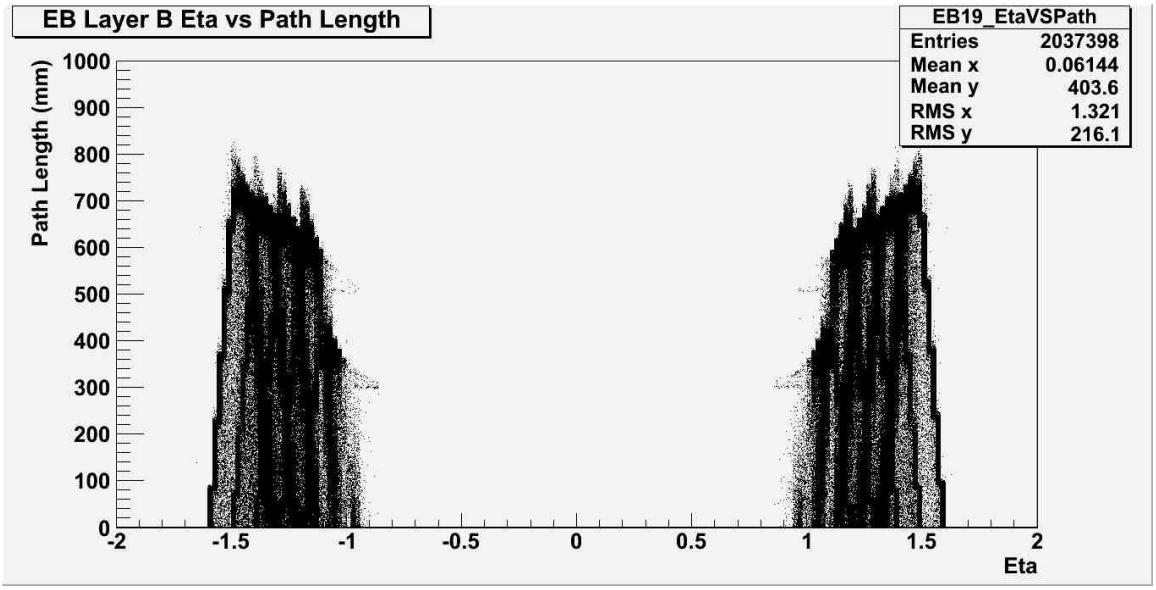

Figure C.8. η vs. Path Length in EB B.

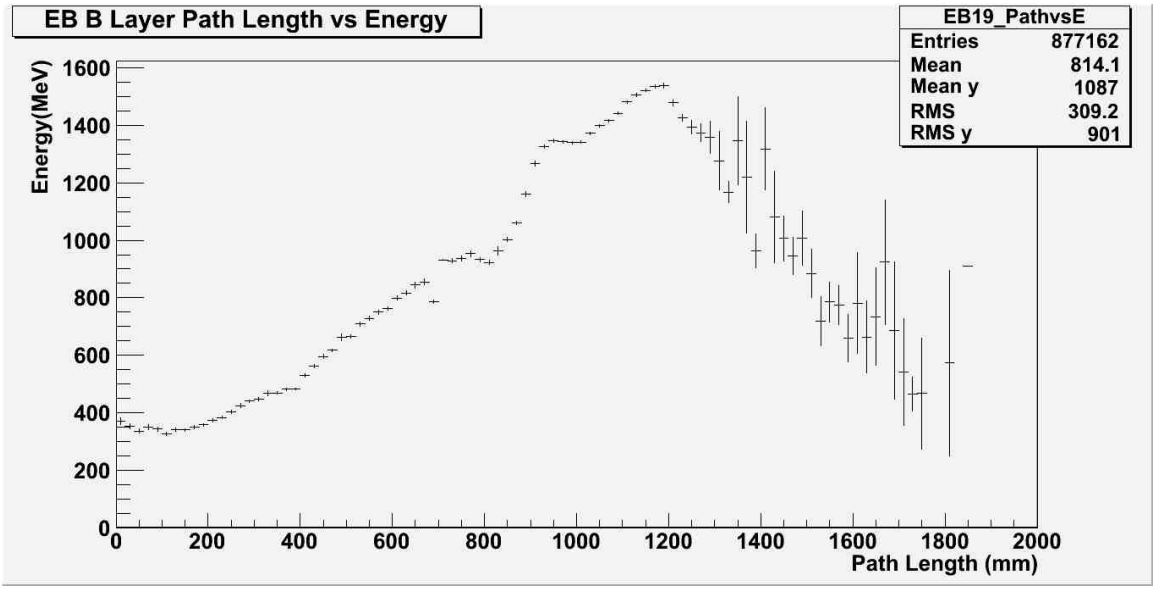

Figure C.9. Path Length vs. Energy in EB B.

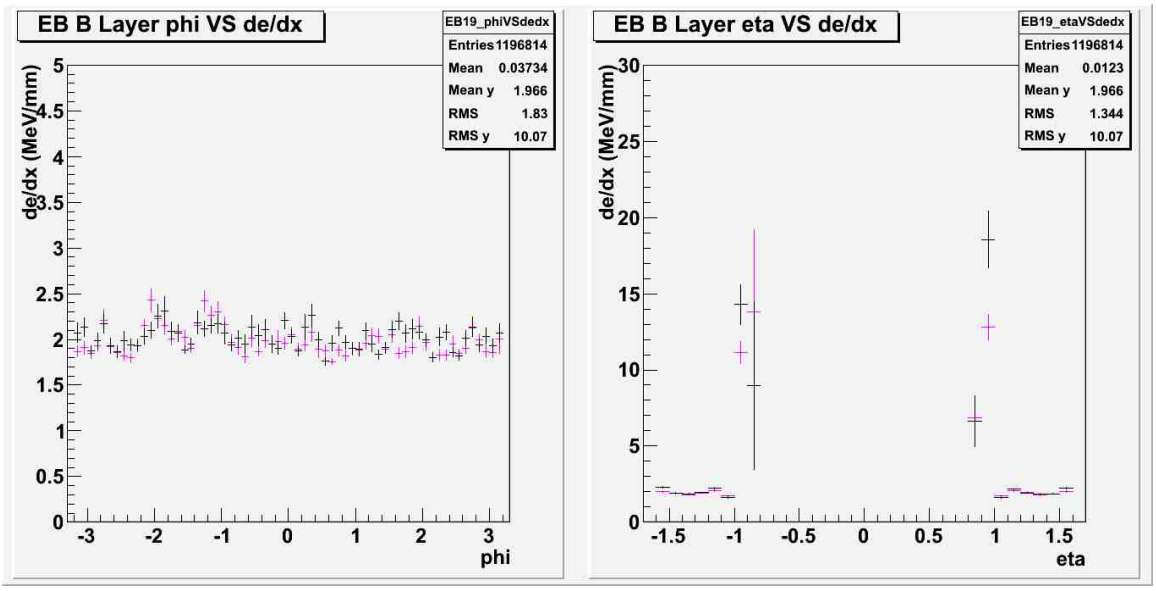

Figure C.10. Response for EB Layer B in ϕ (left) and η (right).

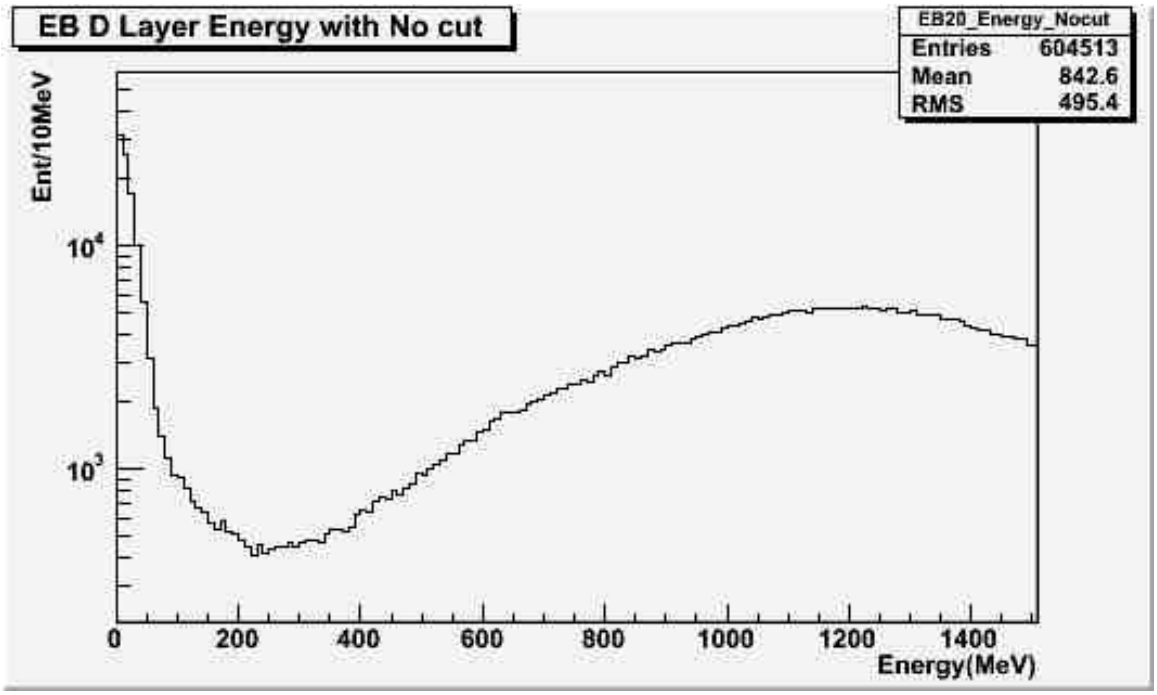

Figure C.11. Uncut Energy Distribution in EB D.

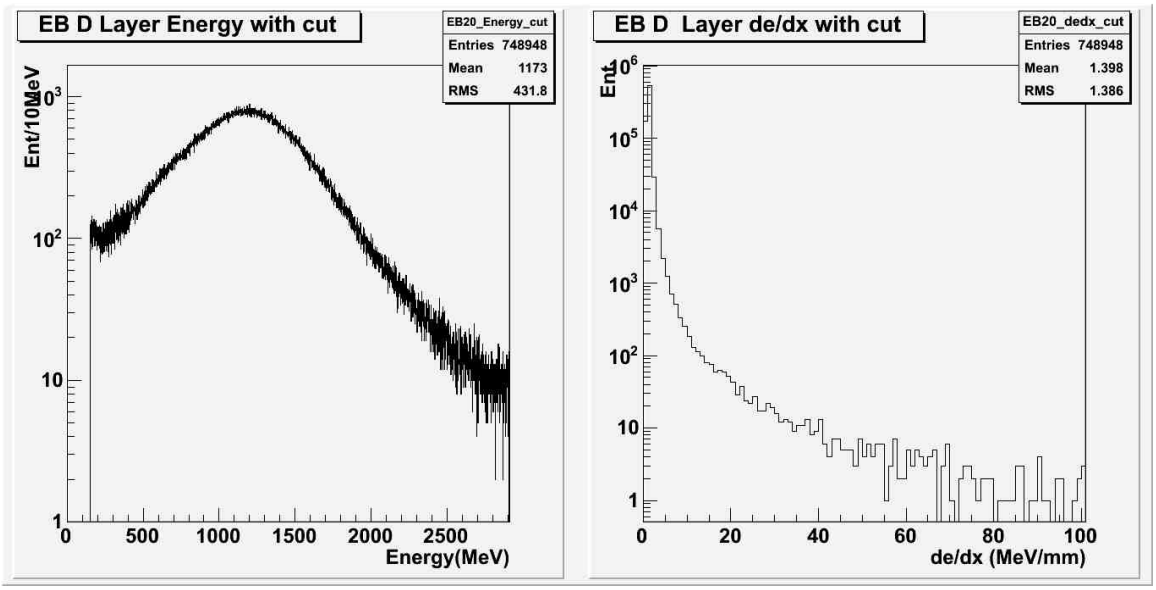

Figure C.12. Energy (left) and dE/dx (right) Distributions after Selection for EB D.

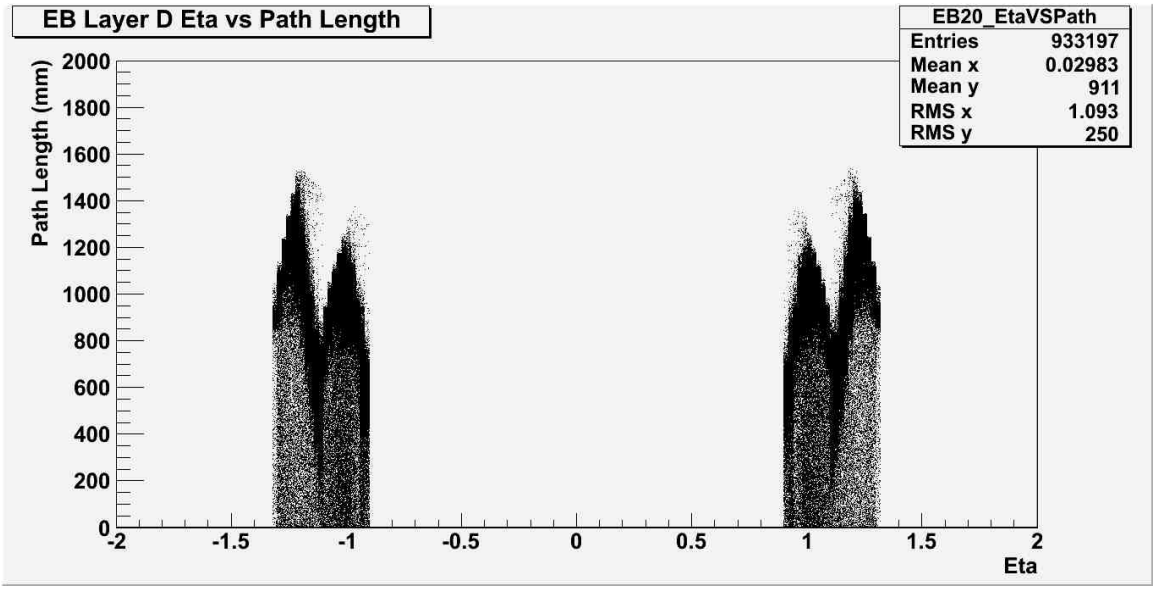

Figure C.13. η vs. Path Length in EB D.

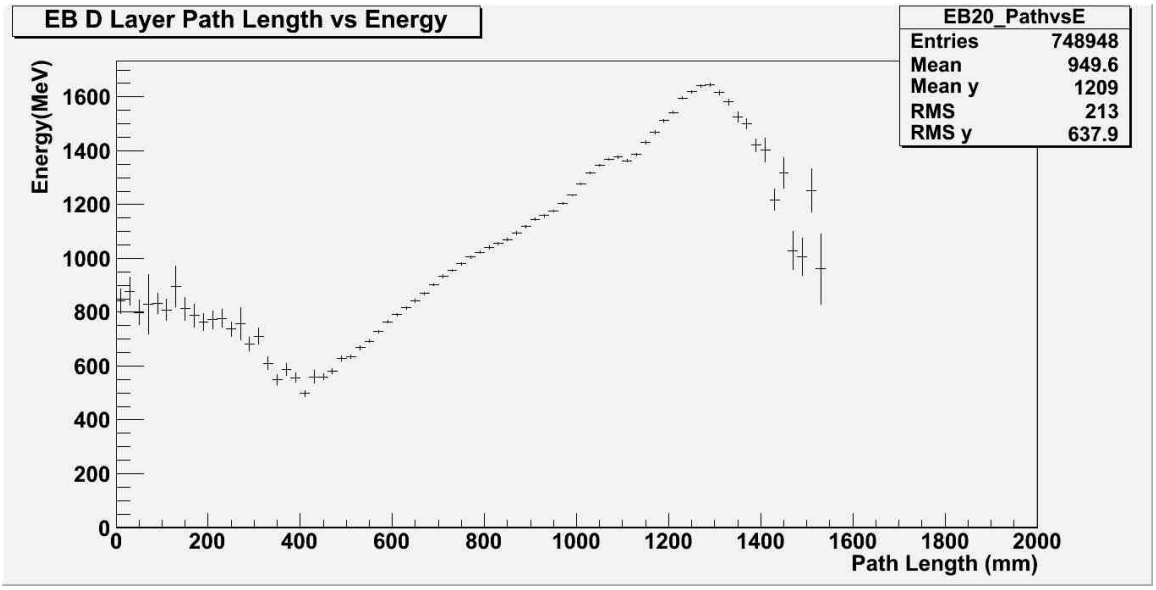

Figure C.14. Path Length vs. Energy in EB D.

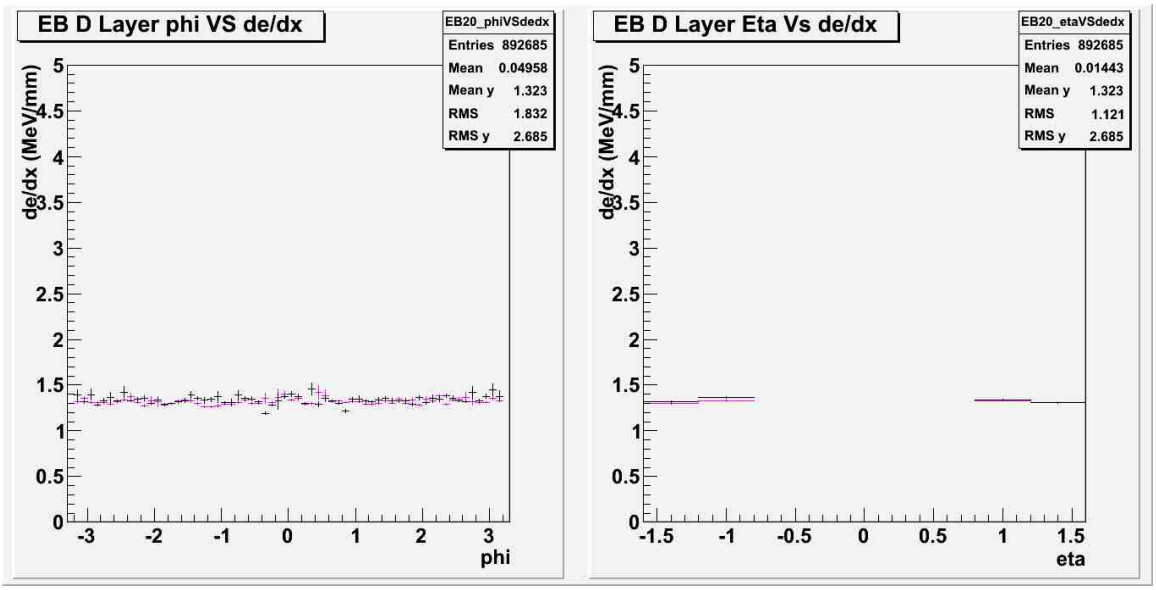

Figure C.15. Response for EB Layer D in ϕ (left) and η (right).

APPENDIX D

C10 YIELD VALUE TABLES

Photoelectron yield value for the C10 cells, both A and C side.

Table D.1. Photoelectron yield values for the C10 cells, modules 1 through 31

Module No.	A-side (1-32)	C-side (1-32)
1	26	42
2	40	3
3	34	27
4	28	21
5	23	19
6	36	29
7	0	45
8	50	52
9	24	33
10	56	26
11	24	33
12	18	0
13	6	0
14	22	16
15	30	37
16	27	26
17	0	42
18	28	35
19	22	23
20	0	14
21	3	7
22	37	2
23	61	43
24	39	39
25	43	43
26	53	44
27	38	31
28	28	18
29	0	19
30	28	25
31	34	35
32	32	29

Table D.2. Photoelectron yield values for the C10 cells, modules 32 through 64

Module No.	A-side (33-64)	C-side (33-64)
33	28	24
34	31	32
35	32	21
36	29	17
37	23	0
38	27	26
39	33	26
40	36	25
41	37	31
42	30	38
43	27	30
44	13	22
45	15	18
46	32	27
47	25	32
48	27	41
49	37	35
50	33	48
51	31	35
52	31	21
53	18	27
54	25	31
55	39	28
56	35	26
57	38	41
58	40	36
59	35	25
60	20	15
61	20	17
62	30	21
63	31	23
64	32	32

REFERENCES

[1] ATLAS fact sheet. The ATLAS Colaboration. Geneva, Switzerland. [Online]. Available: http://www.atlas.ch/fact-sheets-view.html

[2] CERN Press Office. (2011, January) CERN announces LHC to run in 2012. CERN. Geneva, Switzerland. [Online]. Available: http://press.web.cern.ch/press/PressReleases/Releases2011/PR01.11E.html

[3] C. Lefevre. (2008) LHC: the guide. CERN. Geneva, Switzerland. [Online]. Available: http://cdsweb.cern.ch/record/1092437/files/CERN-Brochure-2008-001-Eng.pdf?version=1

[4] I. Aracena. (2009, December) Operational experience of the atlas high level trigger with single-beam and cosmic rays. SLAC-NAL on behalf of the ATLAS Collaboration. Menlo Park, CA. [Online]. Available: http://cdsweb.cern.ch/record/1228285/files/ATL-DAQ-PROC-2009-044.pdf

[5] R. Fernow, *Introduction to Experimental Particle Physics*. New York, NY: Cambridge University Press, 1986.

[6] "ATLAS detector and physics performance technical design report," The ATLAS Colaboration, Geneva, Switzerland, CERN/LHCC 99-14, May 1999.

[7] U. Egede, "The search for a standard model Higgs at the LHC and electron identification using transition radiation in the ATLAS tracker," Ph.D. dissertation, Lund University, Lund, Sweden, January 1998. [Online]. Available: http://www.hep.lu.se/atlas//thesis/egede/thesis-node39.html

[8] G. Usai, "Muon production from K/π decays in flight. an estimation using fully simulated minimum bias events DC1," E. Fermi Institue, Univ.

of Chicago, Chicago, MA, Internal Note, April 2004. [Online]. Available: http://cdsweb.cern.ch/record/990877/files/ATL-COM-PHYS-2006-075.pdf

[9] (2011) ATLAS photos. The ATLAS Experiment. Geneva, Switzerland. [Online]. Available: http://www.atlas.ch/photos/index.html

[10] "ATLAS muon spectrometer technical design report," ATLAS Muon Colaboration, Geneva, Switzerland, CERN/LHCC 97-22, June 1997.

[11] "ATLAS tile calorimeter technical design report," ATLAS/Tile Calorimeter Colaboration, Geneva, Switzerland, CERN/LHCC 96-42, December 2000.

[12] A. Das and T. Ferbel, *Introduction to Nuclear and Particle Physics*. Toh Tuck Link, Singapore: World Scientific Publishing Co. Pte. Ltd., 2003.

[13] (2011, April) Muon reconstruction efficiency in reprocessed 2010 LHC proton-proton collision data recorded with the ATLAS detector. The ATLAS Experiment. Geneva, Switzerland. [Online]. Available: https://atlas.web.cern.ch/Atlas/GROUPS/PHYSICS/CONFNOTES/ATLAS-CONF-2011-063/

BIOGRAPHICAL STATEMENT

Pierce B. Weatherly was born in Fort Worth, Texas, in 1986. He grew up on a farm outside the small town of Itasca, Texas, where he attended the local high school and graduated as Salutatorian in 2004. He graduated Summa Cum Laude from The University of Texas at Arlington (UTA) in 2009 with a B.S. degree in Mathematics and a B.S. degree in Physics. He later earned his M.S. degree from UTA in 2011 in Physics with a graduate studies GPA of 4.0.

From 2006 to 2009, he was with UTA's department of Physics serving as a tutor, and from 2007 to 2009, he served as a tutor with UTA's department of Mathematics. As an undergraduate, he worked with the High Energy Physics (HEP) group at UTA's Physics department, putting together cells in the E layer of the ITC and testing their performance with cosmic rays, as well as working on a prototype Tier 3 computing and display system. He also traveled to the European Organization for Nuclear Research (CERN) and aided the ATLAS group with the commissioning of the ATLAS detector.

When he graduated with his B.S. degrees, Pierce continued on at UTA as a lab instructor and a research assistant with the HEP group, again traveling to CERN for the summer of 2010 to work on an analysis of special asymmetric cells with muons from cosmic rays in the end barrels of the ATLAS Tile Calorimeter (TileCal). Using this analysis, he continued on at UTA using that experience to conduct his study of the response of the TileCal to muons produced in proton-proton collisions provided by the Large Hadron Collider.